Parallel Nano-Manufacturing via Electro-Hydrodynamic Jetting from Externally-Fed Emitter Arrays

by

Philip Ponce de Leon

B.S., Physics, New York University (2011)
B.E., Mechanical Engineering, Stevens Institute of Technology (2011)

Submitted to the Department of Mechanical Engineering
in partial fulfillment of the requirements for the degree of

Master of Science in Mechanical Engineering

at the

MASSACHUSETTS INSTITUTE OF TECHNOLOGY

February 2015

Author .... Signature redacted ....
Department of Mechanical Engineering
September 8, 2014

Certified by Signature redacted
Luis Fernando Velásquez-García
Principal Research Scientist, Microsystems Technology Laboratories
Thesis Supervisor

Certified by.................... Signature redacted ....
Anastasios John Hart
Associate Professor, Department of Mechanical Engineering
Thesis Supervisor

Accepted by .... Signature redacted ......
David E. Hardt
Chairman, Department Committee on Graduate Students

Parallel Nano-Manufacturing via Electro-Hydrodynamic Jetting from Externally-Fed Emitter Arrays

by

Philip Ponce de Leon

Submitted to the Department of Mechanical Engineering
on September 8, 2014, in partial fulfillment of the
requirements for the degree of
Master of Science in Mechanical Engineering

Abstract

The accelerating growth of our ability to engineer at the nanoscale offers unprecedented opportunity to control the world around us in meaningful ways. One particularly exciting development is the production of nanofibers, whose unique morphological properties promise to improve the quality and efficiency of countless technologies. Unfortunately, their integration into almost all of these technologies is unfeasible due to the low throughput and high cost of current production methods. The most common production process, known as electrospinning, involves pumping a viscous, conducting liquid at very low flow rates through a syringe needle in a strong electric field. The emitted charged jet is stretched and whipped extensively creating fibers with diameters as small as tens of nanometers.

Existing approaches to increase throughput via multiplexing of jets are either too complex to scale up effectively, or they sacrifice precision and control. In this thesis research, we report the design, fabrication, and experimental characterization of externally-fed emitter arrays for electro-hydrodynamic jetting. We microfabricate monolithic, emitter blades that consist of pointed structures etched out of silicon using DRIE and assemble these into a slotted base to form two-dimensional arrays. By patterning the emitter surface with appropriately dimensioned microstructures, we enable and control the wicking of liquid toward the emission site via passive capillary action.

Our results confirm greater flow rate per unit area through wicking structures comprised of open microchannels as compared to those consisting of micropillars. We also demonstrate the existence and location of a flow maximum with respect to the width of the microchannels. We test arrays with as many as 225 emitters (25 emitters/cm^2) and with emitter densities as high as 100 emitters/cm^2. The densest arrays (1 mm emitter spacing) fail to electrospin fibers but demonstrate electrospray of droplets. Sparser arrays ($\geq$ 2 mm emitter spacing) are capable of both emission modes, sometimes simultaneously. This can degrade fibers via re-dissolution on the collector electrode and suggests the need for finer control over emission characteristics.

Arrays capable of electrospinning exhibit a mass flux as high as 400 $\left[\frac{g}{hr \cdot m^2}\right]$, which is 4 times the reported production rate of the leading free-surface electrospinning technology. Throughput is shown to increase with increasing array size at constant density suggesting the current design can be scaled up with no loss of productivity. For the arrays tested, increased emitter density led to decreased throughput. This is likely due to a large decrease in electric field enhancement at high emitter densities and may be alleviated with the incorporation of a proximal, individually-gated extractor electrode.

Thesis Supervisor: Luis Fernando Velásquez-García
Title: Principal Research Scientist, Microsystems Technology Laboratories

Thesis Supervisor: Anastasios John Hart
Title: Associate Professor, Department of Mechanical Engineering

Acknowledgments

Funding for this project was provided by the Defense Advanced Research Projects Agency Microsystems Technology Office (DARPA/MTO) under contract W31P4Q-11-1-0007. I thank Luis Fernando Velásquez-García, the project's principal investigator, for giving me the opportunity to work on this research and for serving as my thesis advisor.

There are several people to thank from the mechanical engineering department: Professor John Hart, for serving as co-supervisor of this thesis; Leslie Regan, for providing moral support in addition to unrivaled administrative guidance; and, especially, Professor David Hardt, for giving me the opportunity to work with him as a TA during a funding lapse. Professor Hardt offered kindness as well as perspective on the struggles of graduate thesis research at a time when I was in need of both.

I thank all of the lab staff at MTL for their tireless work. Dennis Ward, in particular, went out of his way to accommodate training requests and after-hours troubleshooting when I faced pressing deadlines. He could also always be counted on for smack-talking the New York Jets.

I thank all of my group mates for their willingness to share their opinions and feedback. Frances Hill provided crucial guidance during the early stages of my research. When I was having trouble getting started, she showed me how to "get my hands dirty" setting up and running simple experiments. I owe very special thanks to Eric Heubel. Countless times, he set aside his own work to help me push through a research obstacle. Collaborating with Eric taught me how difficult and time-consuming it can be to tackle unfamiliar challenges with honesty and humility, rather than look for a quick fix. It also revealed how worthwhile it can be and engendered in me the confidence to make this effort on my own.

I sincerely thank my friends and family for putting up with the madness, only some of which was attributable to MIT, and being there for me nonetheless. Amidst all of the noise, it is easy to lose perspective. I am lucky enough to have wonderful family and friends whose presence in my life serves as a daily reminder of what is truly important.

Contents

List of Figures

List of Tables

List of Symbols

α	Taylor cone half-angle
A	Cross-sectional area
b	External radius of idealized cylindrical emitter
β	Electric field enhancement factor
β_{Max}	Max electric field enhancement factor
Bo	Bond number
C_1, C_2, C_3	Undetermined constants
Ca	Capillary number
Ca_D	Darcy-equivalent capillary number
d	Microfeature size (pillar thickness or microchannel wall thickness)
Da	Darcy number
d_{plate}	Distance from ground plane to collector electrode
$E_{applied}$	Applied electric field (ideal parallel-plate)
E_{crest}	Critical electric field for electro-capillary waves
E_{crit}	Critical electric field for EHD jetting

E Electric field

E_{local} Local electric field strength

$\in$ Is an element of

ϵ_0 Permittivity of free space

ϵ Porosity

ϵ_r Relative electrical permittivity

η Flow consistency index

f_1 First function of geometrical ratios

f Force per unit length

f_2 Second function of geometrical ratios

F_A Meniscus area correction factor

f_b Body force per unit volume

F_{V2} Meniscus flow correction factor

F_V Meniscus volume correction factor

G Liquid spreading coefficient

g Gravitational acceleration

γ Surface tension

γ_{SL} Solid-liquid interfacial energy

γ_{SV} Solid-vapor interfacial energy

h Surface microfeature height

h_{climb}	Height of external meniscus around cylinder
I	Current
K	Electrical conductivity
k	Flow permeability
k_V	Current-voltage power fit, proportional constant
L	Fraction of max meniscus displacement
l	Meniscus displacement
λ	Capillary length
λ_{wave}	Wavelength for electro-capillary waves
$\dot{l}$	Velocity of moving meniscus
l_e	Emitter length
l_{max}	Maximum meniscus displacement in capillary rise
$\dot{m_{avg}}$	Average mass production rate
μ	Viscosity
$\hat{\mathbf{n}}$	Surface normal unit vector
n_p	Flow behavior index
P_ν	ν^{th}-degree Legendre polynomial
p_c	Capillary pressure
ϕ	Azimuthal angle in spherical coordinates
ϕ_s	Solid fraction of porous surface roughness

p_L Liquid pressure

p_M Microfeature pitch

p Pressure

p_V Current-voltage power fit, exponent

Q Flow rate

q Flow rate per unit width

q_{crit} Critical droplet charge (Rayleigh Limit)

q_{enc} Charge enclosed in Gaussian surface

R^2 Coefficient of determination (in curve fit)

r Surface roughness

R_{C1} First principal radius of curvature

R_{C2} Second principal radius of curvature

R_{char} Characteristic pore size

R_{cyl} Cylindrical capillary inner-radius

r_{cyl} Radial distance in cylindrical coordinates

R_{drop} Droplet radius

Re Reynolds number

ρ Mass density

R_s Static-equivalent radius

r_{sph} Radial distance in spherical coordinates

R_{Tip} Emitter tip radius

s Emitter spacing (pitch)

$\bar{\bar{\sigma}}$ Stress tensor

S Surface element

$\bar{\bar{\tau}}$ Deviatoric stress tensor

τ_2 Time constant for visco-gravitational capillary rise

τ_1 Time constant for visco-inertial capillary rise

τ_e Electrical relaxation time

θ Polar angle in spherical coordinates

θ_{CA} Contact angle

θ_{CB} Cassie-Baxter contact angle

$\theta_{CB,crit}$ Critical angle for Cassie-Baxter state

$\theta_{HW,crit}$ Critical angle for hemi-wicking

θ_W Wenzel contact angle

θ_Y Young's contact angle

t Time

U Energy

v Velocity scalar

$\mathbf{v}$ Velocity vector

v_{avg} Average velocity

v_D Darcy velocity

$V_{applied}$ Applied voltage

V Electric potential

$W()$ Lambert W-function

w Microfeature gap

WD Working distance between emitter tips and collector

x Displacement of contact line

z Axial distance along cylindrical capillary

$\zeta()$ Riemann zeta function

$[\ ]^*$ Denotes dimensionless variable

$[\ ]_{chan}$ Denotes microchannel variable

$[\ ]_{pill}$ Denotes micropillar forest variable

Chapter 1

Introduction

1.1 The Untapped Potential of Nanotechnology

Ever since Richard Feynman's renowned 1959 lecture "There's Plenty of Room at the Bottom," the study and development of nanotechnology has been growing at an accelerating pace. Scientists now have the ability to manipulate matter directly at the molecular and atomic scale, perhaps beyond what Feynman imagined, and there is plenty of room to go deeper still [1]. The challenge encountered today in many areas of research, however, is that there is too much room at the top. The tools of the nanotechnology revolution are capable of remarkable precision, but many of them are too slow and expensive to realize the advantages of nano-manipulation for engineering challenges at the human level [2]. If we hope to reap the benefits of modern scientific discovery, an overwhelming fraction of which now occurs in the areas of micro and nanotechnology, we must develop techniques to faithfully control the miniscule over vast scales via the implementation of parallel nano-manufacturing.

Nanofabrication via electro-hydrodynamic jetting, in particular electrospinning, has received much attention recently and is a promising candidate for scaled up production of nanostructures via multiplexing. Electro-hydrodynamic jetting occurs when a strong electric field is applied to the surface of a conductive liquid [3]. The process is capable of producing ion plumes, fine aerosol droplets, or continuous fibers with sub-micron diameters depending on the properties of the liquid used and the ionization conditions [4, 5, 6]. Electrospinning has traditionally been performed from the tip of a syringe needle through which the liquid of interest is pumped at very low flow rates on the order of microliters per minute. For most common polymer solutions, this translates to a mass production rate as low as 0.01 grams per hour compared to a mass production rate on the order of hundreds of grams per hour per fiber jet for mechanically drawn fibers [7, 8]. This low-throughput makes the incorporation of nanofibers into commercial scale technologies impractical and expensive.

Many areas of research would benefit enormously from cheap, high-throughput production of nanofibers [6]. The advantage of electrospinning is its versatility in producing fibers of arbitrary length from a wide range of possible materials including polymers, metals, ceramics, and semiconductors. The applications of the nanofibers themselves are numerous and arise from their unique morphological properties. Dye-sensitized solar cells benefit from the reduction of grain boundaries associated with the one-dimensional structure of nanofibers, which improve charge conduction while allowing better infiltration of the viscous dye-sensitized gel due to their high porosity [9]. The high surface-to-volume ratio of nanofiber mats make them ideal scaffolds for catalyst dispersion in fuel cells or cell growth in tissue engineering [10]. They are great for enhancing any phenomenon which requires large surface area and their high porosity enables the integration of fluid flow. Some examples of such phenomena are charge storage in ultra-capacitors, sensitivity in functionalized bio-sensors, or filtration efficiency in filters and separation membranes [6]. They can even be integrated with other fabrics and layers to create high-performance, multi-functional clothing. The challenge that remains is producing nanofibers in a controlled fashion and in sufficient quantity to realize their enormous potential, in these and many other applications, at the commercial scale.

1.2 Higher Throughput via Multiplexing

The mass throughput of a fiber spinning operation scales linearly with the draw rate and with the square of the fiber diameter. Electrospun nanofibers have diameters $100 - 1000\times$ smaller than those of conventional, mechanically-drawn fibers and, therefore, exhibit a throughput that is $10^4 - 10^6\times$ smaller at equivalent draw rates. Increasing the draw rate is not an effective way to overcome low throughput, since the process is sensitive to flow rate, the productivity gains are linear, and the draw rate is ultimately limited by the speed of sound, above which shock waves occur. A more promising alternative is to spin from many different sources in parallel.

Several different approaches have been adopted in attempts to increase the throughput of electrospinning this way. The most obvious, perhaps, is the use of multiple syringe needles in parallel. This has been done [11] and, although it does increase throughput, it does not scale up well. A complex hydraulic network is required to feed all of the syringes and this, combined with the size of the syringes themselves, limits the possible density of such an array. Increasing the density is crucial, since throughput scales as the square of the array density if draw rate remains unchanged. Other work has used a ferro-fluid covered in polymer solution [12]. A large enough magnetic field triggers an instability in the ferro-fluid forming sharp spikes, which act as emission sites for fiber spinning. This method is simple but suffers from non-uniformity and offers minimal control over the positioning of the spikes. Some research has focused on spinning from a one-dimensional emission site (i.e., an edge) rather than a zero-dimensional emission site (i.e., a needle point). This has been demonstrated in a narrow, confined channel [13], from the edge of a bowl [14], and from a coil of wire [15]. The methods do work but lack control and do not offer an obvious path for scaling up and increasing emission density. They also lack the electric field enhancing properties of a sharp needle tip.

Another simple approach has been to electrospin fibers directly from the free-surface of a liquid [16]. This eliminates the need for pumps or channels of any kind but can require voltages on the order of 30-100 kV. This "brute force" process lacks precise repeatability and exhibits inferior fiber uniformity. It also offers no way to control the density of the jets aside from increasing the electric field. Yet another line of electrospinning research has explored using microscale equipment. PDMS microfluidics can simplify fabrication of a hydraulic network; however, this miniaturization of a closed channel architecture increases pump power requirements and the likelihood of clogging. Spinning directly from microfluidic orifices provides visibly less electric field enhancement and, therefore, requires higher voltage than a needle-like structure [17]. Near-field electrospinning is a technique that employs significantly lower voltages applied over much smaller working distances in order to spin fibers in a more stable fashion [18]. This introduces the possibility of precise fiber deposition and denser, low-powered arrays.

In this thesis, we explore electrospinning from two-dimensional arrays of emitters that are batch-microfabricated for high precision and externally-fed via passive liquid transport through integrated wicking structures on the emitters. The use of microfabrication allows for the combination of design features at hierarchical length scales. Micro-scale wicking structures are patterned on emitters with sub-millimeter, sharp tips for high electric field enhancement. The emitters, which are millimeters long, are arrayed along linear blades that are etched out of silicon wafers using standard microfabrication techniques. These linear blades are assembled out-of-plane into a slotted, microfabricated base to form two-dimensional arrays on the order of centimeters. These, in turn, can be tiled side by side to form arbitrarily large electrospinning sources. Along with the capability to scale up easily via multiplexing, this approach offers great potential to miniaturize. Emitters can be packed into arrays with sub-mm spacing with great accuracy and simplicity. Since the liquid is supplied passively via surface-tension, no pumping system is required.

The design, fabrication, and characterization of our emitter arrays, as well as relevant background theory, will be discussed in the following chapters. Chapter 2 explains the basic physics of electro-hydrodynamic jetting and describes different characteristic modes of operation. Chapter 3 discusses surface tension, wetting behavior at phase interfaces, and the resultant phenomenon of capillary action. Equations governing capillary flow through porous, microstructured surfaces are analyzed to suggest the existence of flow rate maxima for certain optimal geometrical parameters. In chapter 4, we explain the design and fabrication methods used to produce two distinct iterations of our devices. Chapter 5 recounts our experimental findings related to the behavior of liquid on microstructured surfaces. Wicking rates through designed microstructures are compared with those predicted by theoretical models. Chapter 6 details the characterization of electro-hydrodynamic jetting from our emitter arrays. Chapter 7 summarizes our results and describes future directions for research.

Chapter 2

Physics of Electro-Hydrodynamic Jetting

2.1 Traditional Needle Electro-Hydrodynamic Jetting

The term electro-hydrodynamics encompasses a vast and varied array of phenomena resulting from the forces present in electrically charged fluids. The discussion in this thesis is limited to flows in which the electrical forces interact with the free-surface of a conductive liquid in such a way as to disrupt its stability and initiate jetting; hence the specification of electro-hydrodynamic jetting.

The first major theoretical contribution to electro-hydrodynamics came in 1882 when Lord Rayleigh postulated an upper limit on the amount of charge a spherical droplet could carry before it would become unstable and, he hypothesized, emit jets of liquid [19]. He calculated that the onset of ellipsoidal instability associated with the second degree Legendre polynomial corresponds to a droplet charge of q_{crit}

$$q_{crit} = \sqrt{64\pi^2\epsilon_0\gamma R_{drop}^3} \tag{2.1}$$

where ϵ_0 is the permittivity of free space, γ is the liquid surface tension, and R_{drop} is the droplet radius. The same result can be derived more expediently by balancing the electric field energy density, or electrostatic pressure, just outside the droplet with the pull of surface tension:

$$\frac{1}{2}\epsilon_0 E^2 = \gamma(\frac{1}{R_{C1}} + \frac{1}{R_{C2}}) = \frac{2\gamma}{R_{drop}} \tag{2.2}$$

Here the capillary pressure is given in terms of the liquid surface's two principle radii of curvature R_{C1} and R_{C2}, which are the same everywhere on the surface of a spherical droplet and equal to R_{drop}. Therefore, the critical electric field strength above which electric pressure dominates surface tension can be written as

$$E_{crit} = 2\sqrt{\frac{\gamma}{\epsilon_0 R_{drop}}} \tag{2.3}$$

This expression is applicable to other surface shapes more general than a sphere if $\frac{2}{R_{drop}}$ is replaced with the mean curvature $(\frac{1}{R_{C1}} + \frac{1}{R_{C2}})$. In the specific instance of an isolated, charged spherical droplet, the electric field outside of the droplet behaves as though all of the charge is concentrated at the droplet's center, which is a result of symmetry and can be shown with Gauss's Law. Choosing a surface S just outside the droplet one can write

$$q_{enc} = \epsilon_0 \iint_S E \cdot \mathrm{d}S \tag{2.4}$$

$$q_{enc} = \epsilon_0 E_{crit} \iint_S \mathrm{d}S = 2\epsilon_0 \sqrt{\frac{\gamma}{\epsilon_0 R_{drop}}} R_{drop}^2 \iint_S \sin\theta \mathrm{d}\theta \mathrm{d}\phi \tag{2.5}$$

$$q_{enc} = \sqrt{64\pi^2 \epsilon_0 \gamma R_{drop}^3} = q_{crit} \tag{2.6}$$

This is the Rayleigh charge limit stated earlier.

In 1914, Zeleny examined liquid at the end of a capillary held at some potential difference relative to an opposing flat plate. He observed the liquid meniscus assume a number of unique configurations, and, at high enough voltages, witnessed jetting from the meniscus [20]. He attempted to describe the instabilities he observed by extending Rayleigh's harmonic analysis to prolate spheroidal droplets; however, he made several poor assumptions regarding the matching of the pressure distribution inside the droplet with the electric pressure distribution outside the droplet [3]. His approach remained accepted until the 1960s when G.I. Taylor revisited the issue of stable electro-hydrodynamic jetting.

2.1.1 The Taylor Cone

Taylor's theoretical description of the stable cone-shaped equilibrium interface that bears his name was inspired by a combination of mathematical reasoning and previous experimental results. Taylor reasoned that a stable meniscus equilibrium would require a local electric pressure that everywhere equaled the local Laplace pressure. For a spherical droplet in a spherically symmetric field, this is trivial; the mean curvature and the electric field strength are always constant over the entire liquid surface. In more general cases, this balance would require an electric field everywhere proportional to a varying mean curvature. Taylor knew that Zeleny and others had observed conical menisci during their experiments in addition to ellipsoidal perturbations. Compared to an ellipsoid, a conical meniscus has a much more simply varying mean curvature; $R_{C2} = \infty$ and $R_{C1} = \frac{r_{sph}}{cot(\alpha)}$, where α is the cone half-angle and r_{sph} is the radial spherical coordinate or distance of a surface element from the cone vertex (Figure 2-1).

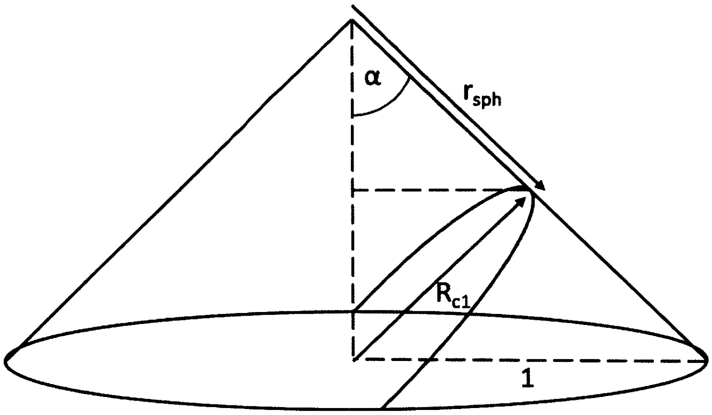

Figure 2-1: Taylor cone geometry: Curvature varies with distance r_{sph} from apex.

A stable cone-shaped interface would require a field $E \propto \frac{1}{\sqrt{r_{sph}}}$ or, equivalently, a potential $V \propto \sqrt{r_{sph}}$. An infinite conic geometry is easily described in spherical coordinates originating from the cone vertex as $\cos\theta = constant$, where θ is the polar angle coordinate. Axisymmetric solutions to Laplace's equation outside an infinite cone take the form

$$V = C_1 r_{sph}^{\nu} P_\nu(cos\theta) + C_2 \frac{1}{r_{sph}^{\nu+1}} P_\nu(cos\theta) + C_3 \tag{2.7}$$

where P_ν are ν^{th}-degree Legendre functions of the first kind. To satisfy the aforementioned conditions for equilibrium, $C_2 = 0$ and $\nu = \frac{1}{2}$ leaving

$$V = C_1 r_{sph}^{1/2} P_{1/2}(cos\theta) + C_3 \tag{2.8}$$

A cone at constant potential V_0 can only exist when $P_{1/2}(cos\theta) = 0$, which occurs when $\theta = \theta_0 = 130.71\,\text{deg}$. This corresponds to a cone half-angle $\pi - \theta_0 = \alpha = 49.29\,\text{deg}$ that is independent of surface tension. The constant C_1 can be determined by setting the normal electric field equal to the critical electric field:

$$E_\theta = \frac{-1}{r_{sph}} \frac{d}{d\theta} V = \frac{-C_1}{r_{sph}^{1/2}} \frac{d}{d\theta} [P_{1/2}(cos\theta)]_{\theta=\theta_0} = \sqrt{\frac{2\gamma \cot\alpha}{\epsilon_0 r_{sph}}} \tag{2.9}$$

Numerical evaluation gives $\frac{d}{d\theta}[P_{1/2}(cos\theta)]_{\theta=\theta_0} \approx -0.974$ and the Taylor cone potential is

$$V = V_0 + 0.952\sqrt{\frac{2\gamma}{\epsilon_0 r_{sph}}} P_{1/2}(cos\theta) \tag{2.10}$$

The predicted Taylor cone half-angle of $\alpha = 49.29\,\text{deg}$ agrees quite well with a wide range of experimental observations; however, more recent work has discovered significant deviation from the predicted half-angle under circumstances of low liquid conductivity, large viscoelastic forces, or non-negligible space charge effects [21].

2.1.2 Droplet Break-up in Electrospray

When low-viscosity, high-conductivity liquids in a capillary are acted upon by an electric field on the order of the critical magnitude mentioned earlier, it is common for liquid to be ejected from the tip of the Taylor cone in what is known as electrospray.

Depending on certain parameters, different modes of emission can be observed. For example, dripping will occur for lower applied electric fields and higher flow rates. Most electrospray of practical interest is some variation on the cone mode of operation, which can be further subdivided into cone-jet mode and cone-droplet mode.

In cone-jet mode, a straight jet will exit the cone tip and remain stable until a certain critical length, which generally increases with viscosity, resistivity, and flow rate. Beyond this critical length, perturbations to the jet surface will grow as a result of capillary forces which seek to minimize the surface energy of the jet by forcing its breakup into droplets. This is known as the Rayleigh-Plateau instability, or just the Rayleigh instability. In the limit of low viscosity, the droplets produced have a diameter roughly 1.9 times the jet diameter and do not depend strongly on the jet charge; increasing the viscosity of the liquid will increase the ratio of droplet diameter to jet diameter [5]. In many cases of cone-jet electrospray, it has been observed experimentally that the current and the droplet size are roughly independent of the applied voltage or the electrode geometry. As long as the voltage is sufficient to generate electrospray, the current and droplet size scale with the imposed flow rate [22, 23]. Others have measured some dependence of flow rate on voltage and emitter geometry [24].

Cone-droplet mode differs from cone-jet mode in that droplets are produced directly from the end of the Taylor cone rather than from the breakup of a jet associated with the Rayleigh instability. This mode, also referred to as microdripping, requires very low flow rates and is sensitive to details such as the shape and wettability of the capillary used [5]. In the limit of increasingly small droplets, it is possible to emit a plume consisting of individual ions. This can be achieved by sufficiently impeding the liquid using micro/nano-scale flow control structures. Electrospray in the ionic regime exhibits considerable dependence upon applied voltage [25].

2.1.3 Nanofiber Formation in Electrospinning

High-viscosity and viscoelastic liquids respond differently than low-viscosity liquids when exposed to large electric fields at the end of a capillary. In both cases, surface tension acts to destabilize the liquid jet via the Rayleigh instability; however, viscous liquids are able to resist breakup into droplets and, instead, are drawn out into thin fibers in what is known as electrospinning (Figure 2-2). However, it is not only viscosity that counteracts the Rayleigh instability. Wavelike perturbations on the jet surface bring surface charges closer together, which resist this change via mutual repulsion. Also, if the axis of the jet is parallel to the applied electric field, as it often will be in the region near the emitter, then this field will act on the surface charge creating a force tangential to the jet that counteracts the liquid's capillarity. Higher conductivity liquids increase free surface charge and, therefore, suppress the Rayleigh instability [26].

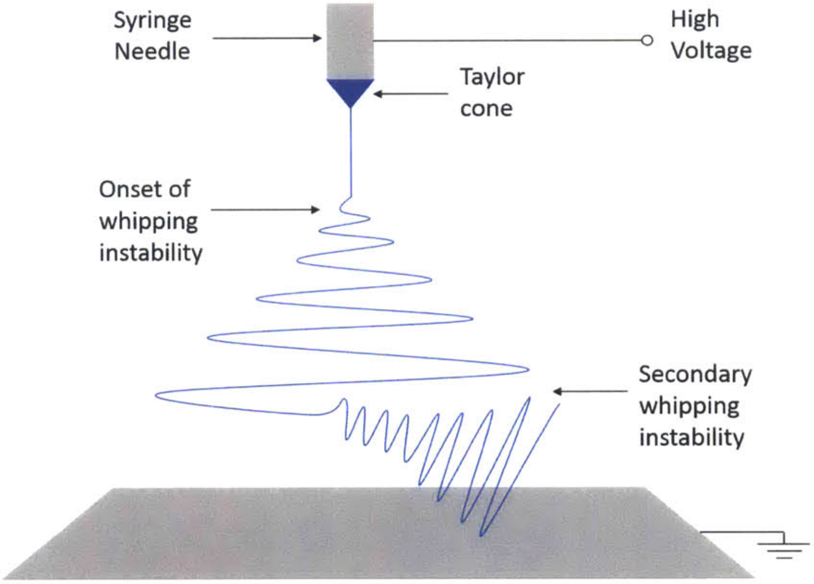

Figure 2-2: Schematic of traditional needle electrospinning: Electrospinning is characterized by a chaotic whipping instability that stretches fibers to ultrathin diameters as small as tens of nanometers.

There are two other instabilities that can affect a viscous, electrically conductive jet. The axisymmetric conducting mode arises from interactions between the applied field and the surface charge on the jet. Perturbation of the jet radius drives unequal redistribution of surface charge which is accelerated unequally by the applied electric field. The difference in the electrical relaxation time and the fluid relaxation time results in an oscillatory response. This axisymmetric instability is increasingly unstable at higher applied fields [26].

The final instability, the whipping conducting mode, is that which is most recognized in electrospinning and accounts for the tremendous fiber thinning ratios of which the process is capable. This mode results from repulsion among the like charges on the jet, and, unlike the other two modes, the whipping instability is not axisymmetric in nature. It is an example of Earnshaws's theorem, which states that a collection of charges cannot maintain a stable electrostatic equilibrium [27]. Since this is primarily a surface charge effect, it is most unstable for high conductivity liquids and large jet radii. It is the dominant instability when the normal electric field at the jet surface exceeds the tangential field, and, therefore, can be reduced by increasing the applied field strength. Capillary forces, which resist the creation of greater surface area, act as a stabilizing influence on the whipping mode.

2.2 Electric Field Enhancement of Emitter Geometries

A key aspect of traditional needle electro-hydrodynamic jetting is the syringe needle geometry from which the jetting occurs. The use of a high-aspect-ratio, conductive emitter with a sharp tip results in a large magnification of the electric field near the tip compared with an otherwise uniform field. This local "enhancement" of the field strength results from the dense buildup of surface charge required to cancel the interior electric field in regions of high curvature. The practical advantage of such field enhancing geometries is that the critical electric field for jetting can be achieved locally at lower bias voltages.

Various models have been proposed to predict the field enhancement factor β, which is dependent on the electrode geometry but independent of the applied voltage. It can be defined in a number of ways, but this work will use the most common convention for geometries comprised of some feature protruding from a grounded plane:

$$\beta = \frac{E_{local}}{E_{applied}} = \frac{E_{local} d_{plate}}{V_{applied}} \tag{2.11}$$

where d_{plate} is the distance between the grounded plane and an opposing, planar electrode and $V_{applied}$ is the potential bias between these two opposing electrodes.

The simplest models for predicting field enhancement factors treat the protruding feature as either a half-cylinder or half-sphere. These geometries produce electric fields that are equivalent to those produced, respectively, by an infinite, conducting cylinder or a conducting sphere placed in a uniform applied field. In both cases, an exact analytical solution can be derived for the field everywhere. For a cylinder, the electric field at the apex is twice the applied field; for a sphere, the field at the apex is enhanced by a factor of three. There are two points worth noting, here. The first is that a cylinder has a lower maximum field enhancement factor than a sphere. This result generalizes to other simple shapes: a two-dimensional version only has curvature in one-dimension and, therefore, has a lower max enhancement factor than a three-dimensional version of the same cross-section that has been revolved. The second curious detail is that the enhancement factors in either case are independent of feature radius and d_{plate}. This stems from the idealization of a perfectly uniform applied field. It does not hold true for more prolate features or when d_{plate} is on the order of the feature size [28].

In order to accurately model more pointed features, the previous models were generalized to the case where the feature cross-section is ellipsoidal rather than circular [29]. For the elliptical half-cylinder, the max enhancement factor can be given exactly as

$$\beta_{Max} = 1 + \sqrt{\frac{l_e}{R_{Tip}}} \tag{2.12}$$

where l_e is the emitter length and R_{Tip} is the tip radius. For a three-dimensional hemi-ellipsoid (Figure 2-3), a reasonable approximation of the max enhancement factor in the limit $\frac{R_{Tip}}{l_e} << 1$ is

$$\beta_{Max} = \frac{2\frac{l_e}{R_{Tip}}}{ln(4\frac{l_e}{R_{Tip}}) - 2} \tag{2.13}$$

These relationships better describe the dependence of field enhancement on emitter geometry. The trend of β_{Max} scaling roughly linearly with aspect ratio in 3D or as the square root of aspect ratio in 2D has been demonstrated for a number of prolate geometries [28]. However, the absence of d_{plate} in these formulas highlights the fact that they assume a uniform applied field - an assumption most accurate for working distances much larger than the emitter dimensions.

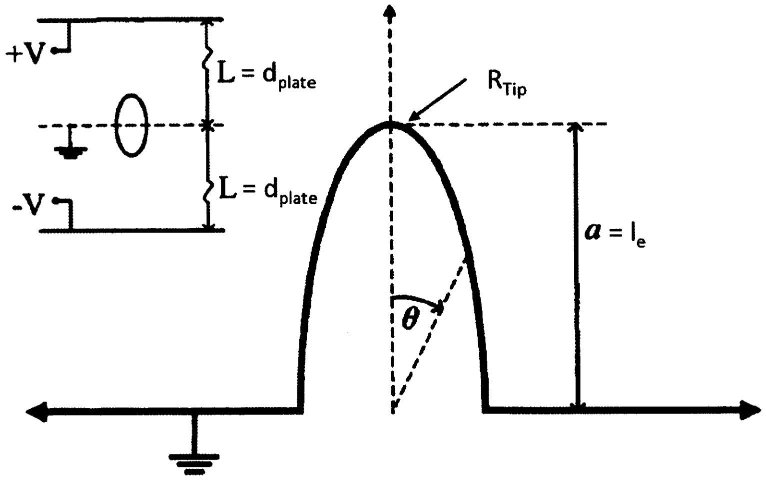

Figure 2-3: Schematic of hemi-ellipsoidal emitter: A prolate ellipsoid model better approximates the electric field around high aspect-ratio structures [30]. Please notice that using the convention we adopted in the text, $a = l_e$ and $L = d_{plate}$.

2.2.1 Free-surface Electrospinning

Free-surface electrospinning refers to the technique of applying strong electric fields to a viscous, conducting liquid to initiate jetting directly from the exposed liquid surface. This method requires no active pumping or complex hydraulic network; however, it suffers from a lack of field enhancement compared to approaches employing high-aspect-ratio emitters. Jet formation is instead catalyzed by the crests of surface waves, which become unstable above an electric field strength $E_{crest} = (\frac{4\gamma\rho g}{\epsilon_0^2})^{1/4}$ [13]. For distilled water, this critical value is $2.46 \times 10^6 \left[\frac{V}{m}\right]$ which is roughly 70% of the breakdown voltage of dry air at atmospheric pressure. Creating such large fields at working distances on the order of many centimeters requires very high voltage and leaves little room for error.

The characteristic wavelength of jet formation in free-surface electrospinning can be approximated by neglecting viscosity and deriving a dispersion relation from Euler's equation in an idealized one-dimensional geometry. The wavelength that determines jet spacing is given by $\lambda_{wave} = \frac{12\pi\gamma}{2\epsilon_0 E^2 \sqrt{(2\epsilon_0 E^2)^2 - 12\gamma\rho g}}$ [16]. This means for a given working liquid, the jet density can only be increased via an increase in the electric field. Although the scaling is favorable (doubling the field reduces the jet spacing by approximately a factor of four), the high threshold field limits the upside since breakdown occurs at less than twice the critical field.

Chapter 3

Physics of Surface-Tension Driven Flows

3.1 Surface Tension Forces

3.1.1 Young's Equation and Static Contact Angle

When two immiscible fluids come into contact with a perfectly smooth and rigid solid surface, they assume a configuration that is governed by the balance of forces per unit length of their mutual boundary line. These surface tensions arise from interactions at the molecular level and can be thought of more generally as the free energy per unit area of the interfaces. In the common case where an ambient fluid is in the vapor phase and a localized fluid is in the liquid phase, the force balance can be written as

$$\Sigma f = \gamma_{SV} - \gamma_{SL} - \gamma \cos \theta_{CA} \tag{3.1}$$

where γ_{ij} is an interfacial energy. The subscripts S, L, and V indicate the solid, liquid, and vapor phases, respectively (the absence of subscripts denotes the liquid-vapor surface tension), and θ_{CA} is the contact angle between the solid-liquid interface and the liquid-vapor interface. Solving for the static case $f = 0$ gives what is known as Young's Equation:

$$\gamma_{SV} = \gamma_{SL} + \gamma \cos\theta_{CA} \tag{3.2}$$

Rearranging the terms above yields an expression for the contact angle of a sessile droplet on an ideal solid surface, also known as Young's angle (Figure 3-1).

$$\cos\theta_Y = \frac{\gamma_{SV} - \gamma_{SL}}{\gamma} \tag{3.3}$$

In a physically possible situation, the contact angle θ_Y must fall within the range $0° - 180°$, which corresponds to a range of $[-1, 1]$ for the cos function. Outside of this range there is no equilibrium solution. Values greater than 1 indicate a condition of complete wetting, in which a liquid droplet will spontaneously spread on the solid surface forming a film of molecular thickness. Values less than -1 indicate a condition of complete dewetting, in which a liquid film will spontaneously separate into fully spherical droplets that will theoretically leave the solid surface in the absence of other forces (e.g., gravity). Complete wetting actually occurs in nature, but complete dewetting has never been observed experimentally. When the liquid in mention is water, low-contact angle interfaces (i.e., $\theta < 90°$), are called hydrophilic while high-contact angle interfaces (i.e., $\theta > 90°$) are called hydrophobic, although these terms are often extended to describe any wetting or non-wetting behavior irrespective of the liquid studied.

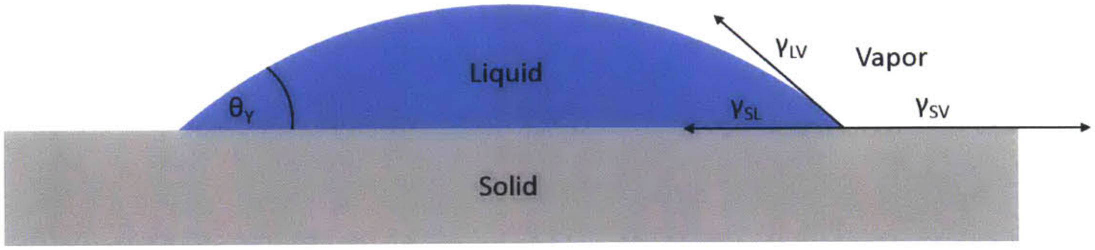

Figure 3-1: Young's Contact Angle: Young's angle is determined by the equilibrium of the three relevant surface tensions on a smooth surface.

3.1.2 Droplet States on a Rough Surface

The predictive power of Young's equation is severely limited by the non-ideality of most real solid surfaces. For one, it is difficult to accurately measure or calculate the interfacial energy of a solid. When reliable values are known, the presence of both chemical inhomogeneities (i.e., contaminants) and physical inhomogeneities (i.e., roughness) results in large discrepancies between measured contact angles and Young's angle. Even contact angle measurements on the same exact surface will vary depending on whether or not the droplet front is advancing or receding. This hysteresis is believed to be a consequence of how the contact line becomes pinned to microscopic defects on the surface [31]. Two major modifications of Young's model have been developed to describe the apparent contact angles that occur on real, inhomogeneous surfaces: the Wenzel model and the Cassie-Baxter model, both of which are described below.

Wenzel Model

The Wenzel model describes the apparent contact angle of a droplet on a roughened substrate when the liquid comes in contact with the entire solid surface (Figure 3-2) [32]. A simple way to derive the result is to minimize the surface energy of the system with respect to an infinitesimal displacement dx of the contact line. If one defines r as the ratio of total solid surface area to apparent area and θ_W as the apparent contact angle, then one can write the energy change per unit length of the contact line as

$$dU = r(\gamma_{SL} - \gamma_{SV})dx + \gamma dx \cos\theta_W. \tag{3.4}$$

The energy is minimized and the force is zero when $-\frac{dU}{dx} = 0$ yielding the condition

$$\cos\theta_W = r\cos\theta. \tag{3.5}$$

This relationship implies that roughness magnifies the expected wetting or non-wetting properties of an ideal surface as predicted by Young's equation. Wenzel's model only begins to describe the range of droplet behavior observed on inhomogeneous surfaces, and it often disagrees with experimental observations. It is most accurate in circumstances when the roughness is free of high curvature edges and has a characteristic size much smaller than the size of the droplet [31].

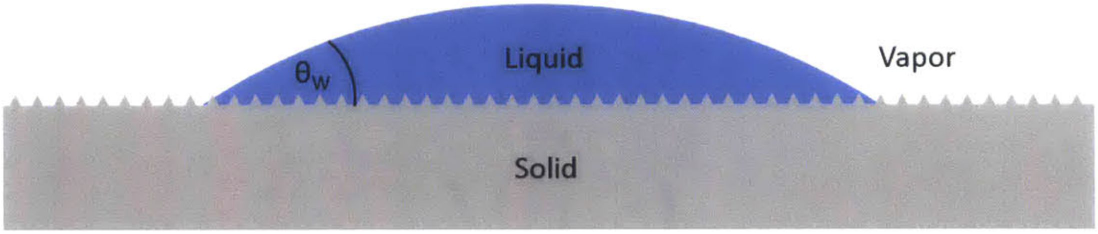

Figure 3-2: Wenzel Contact Angle: The Wenzel model predicts enhancement of the Young wetting state with increased surface roughness.

Cassie-Baxter Model

The assumptions of the Wenzel model often prove incorrect when dealing with intrinsically non-wetting interfaces that possess high roughness. In such cases, rather than displacing the entrenched vapor and assuming the Wenzel state, it can be energetically favorable for a droplet to sit atop a combination of solid and vapor in what is known as the Cassie-Baxter state (Figure 3-3) [33]. For uniformly patterned microfeatures (e.g., pillars, channels), we can write down the condition for an energetically favorable Cassie-Baxter state as

$$(r-\phi_s)(\gamma_{SL}-\gamma_{SV}) > (1-\phi_s)\gamma \tag{3.6}$$

where r is again the surface roughness and ϕ_s is the ratio of the features' top area to the total area. This relation neglects the meniscus curvature under the droplet which is a reasonable approximation for densely packed features much smaller than the droplet [31]. One can recast the above in terms of a critical contact angle $\cos\theta_{CB,crit}$ that depends only on the surface roughness geometry:

$$\cos\theta_{CB,crit} = -\frac{(1-\phi_s)}{(r-\phi_s)} \tag{3.7}$$

Any material interface whose chemically-defined Young's angle is greater than $\theta_{CB,crit}$ will favor the Cassie-Baxter state.

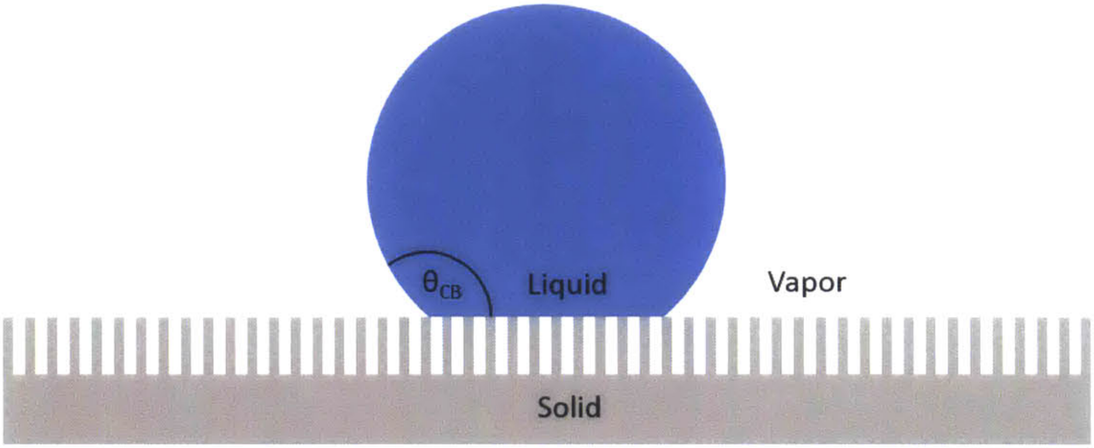

Figure 3-3: Cassie-Baxter Contact Angle: The Cassie-Baxter model describes the contact angle of droplets that rest upon multiple phases at scales smaller than the droplet.

As before, one can determine the macroscopically apparent contact angle in this state θ_{CB} by minimizing the system's surface energy with respect to a displacement of the contact line. Since the droplet now sits on both solid and vapor, the energy balance is as follows:

$$dU = \phi_s(\gamma_{SL} - \gamma_{SV})dx + (1 - \phi_s)\gamma dx + \gamma dx \cos\theta_{CB} = 0 \tag{3.8}$$

$$\cos\theta_{CB} = \phi_s(1 + \cos\theta_Y) - 1 \tag{3.9}$$

The result is fascinating. Interfaces with a mildly hydrophobic Young's angle can be made superhydrophobic (i.e., θ_{CA} near 180°) with the introduction of suitable roughness. Even intrinsically hydrophilic interfaces can be coerced into superhydrophobicity via high-aspect-ratio microstructures with re-entrant profiles that provide a large energy barrier blocking the Wenzel transition [34]. The Cassie-Baxter state exhibits low contact angle hysteresis and high mobility droplets due to the small area where liquid actually contacts the solid. The easily shed droplets minimize contamination of the solid surface.

3.1.3 Young-Laplace Equation, Capillary Action, and Hemi-wicking

In surface tension-driven flows, contact angles merely serve as the boundary condition for determining the configuration of the remainder of the fluid surface. The local curvature of this surface, often called the meniscus, can be directly related to the pressure discontinuity, known as the capillary pressure Δp_c, that occurs across it via the Young-Laplace equation:

$$\Delta p_c = -\gamma \nabla \cdot \hat{\mathbf{n}} \tag{3.10}$$

which can be rewritten as

$$\Delta p_c = -\gamma(\frac{1}{R_{C1}} + \frac{1}{R_{C2}}) \tag{3.11}$$

where R_{C1} and R_{C2} are the principle radii of curvature of the liquid free-surface. The minus sign in the equation implies that pressure is higher on the concave side of an interface than it is on the convex side. This has important implications for humans and redwoods alike as it underlies the pressure differential behind all biological capillary action. Inside a narrow cylindrical capillary tube, where gravitational effects are negligible, a meniscus takes on the shape of a section of spherical surface maintaining a constant pressure differential of $\Delta p_c = \frac{2\gamma \cos \theta_{CA}}{R_{cyl}}$ where R_{cyl} is the cylinder radius. Only in the simplest flow geometries, such as a cylindrical capillary tube, can the free-surface shape and resulting pressure distribution be described with an exact analytical solution. Fortunately, some more complex problems are amenable to approximation with the kind of variational energy analysis that was applied to derive apparent contact angles on real surfaces.

The previous contact angle calculations examined static situations; that is, they described liquid configurations in a minimum energy state when the net force experienced by the contact line was equal to zero. However, given a non-equilibrium starting condition, there will be a net force on the contact line that will distort the liquid surface and create a driving capillary pressure. On most smooth, ideal surfaces, a deposited droplet quickly adjusts its shape to reach the equilibrium contact angle. The presence of persistent driving forces would only arise in the complete wetting scenario discussed earlier which requires the condition $\frac{(\gamma_{SV} - \gamma_{SL})}{\gamma} > 1$ be met. Adding roughness to the surface can ease this constraint for sustained flow and significantly increase the flow volume. It can be thought of as embedding many small capillary tubes within the solid surface. Such liquid propagation has been coined hemi-wicking and is analogous to wicking in closed tubular capillaries [31].

Consider again pillar-like surface roughness (Figure 3-4); the condition for hemi-wicking through the roughness is $f = -\frac{dU}{dx} > 0$. Accounting for the gained and lost interfaces associated with an advancing liquid front ignoring meniscus curvature, one can write the energy balance as

$$dU = (\gamma_{SL} - \gamma_{SV})(r - \phi_s)dx + \gamma(1 - \phi_s)dx \tag{3.12}$$

$$-\frac{dU}{dx} = f = \gamma(1 - \phi_s)(\cos\theta_{CA}\frac{(r - \phi_s)}{(1 - \phi_s)} - 1) \tag{3.13}$$

The average capillary pressure can be approximated as the average force per unit length of the contact line divided by the average flow cross-section per unit length of the contact line or

$$\Delta p_c = \frac{f}{h(1 - \phi_s)} = \frac{\gamma}{h}(\frac{\cos\theta_{CA}}{\cos\theta_{HW,crit}} - 1) \tag{3.14}$$

where h is the microfeature height and $\theta_{HW,crit} = \cos^{-1}[\frac{(1 - \phi_s)}{(r - \phi_s)}]$ is the critical contact angle below which the spreading force is positive and propagation through the roughness occurs. The cosine of this critical angle is the same magnitude as that of the Cassie-Baxter critical angle but negated. This reveals the important role of roughness in defining the regimes of liquid behavior on a solid surface. On smooth, ideal solids, virtually all droplets assume a static equilibrium fully in contact with the surface and adopt a contact angle somewhere between 0° and 120° (roughly the highest known Young's angle). As surface roughness increases, the most intrinsically hydrophilic and most intrinsically hydrophobic interfaces cross over into the regimes of hemi-wicking and superhydrophobicity, respectively, while intermediate interfaces adopt the Wenzel state. At very high surface roughness, static Wenzel-like droplets are almost non-existent as, theoretically, all interfaces with a Young's angle below 90° exhibit hemi-wicking while those with one above 90° become superhydrophobic.

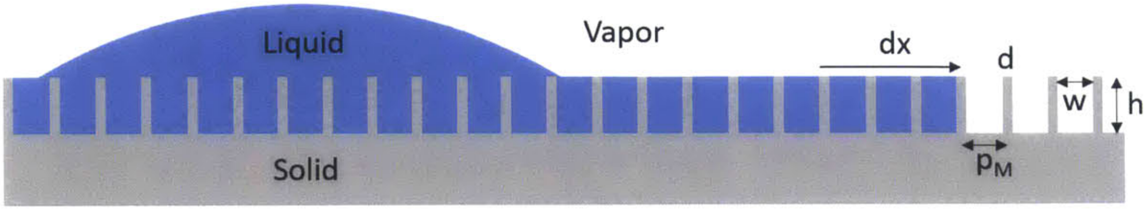

Figure 3-4: Schematic of hemi-wicking: Hemi-wicking refers to the propagation of liquid through porous surface roughness driven by surface energy gradients.

3.2 Dynamics of Surface-Tension Driven Flows

The previous sections introduced the surface-tension phenomena that arise from molecular interactions within a continuum and described the equilibrium position of a liquid droplet on a solid that results from the balance of surface-tension forces. The Young-Laplace equation was established as the means to translate surface-tension boundary conditions into menisci shapes and a corresponding pressure distribution within the bulk liquid. In order to predict the resulting liquid flow, one must relate its motion to these forces present within the liquid.

3.2.1 Cauchy Momentum Equation and Navier-Stokes

Conservation of momentum in a continuum can be formally expressed via the Cauchy momentum equation:

$$\rho \frac{D\mathbf{v}}{Dt} = \nabla \cdot \bar{\bar{\sigma}} + \mathbf{f_b} \tag{3.15}$$

For a fluid, the stress tensor can be broken apart into a pressure component ∇p_L and a deviatoric component $\nabla \cdot \bar{\bar{\tau}}$ that is responsible for deforming the fluid. If we also expand the material derivative term on the left-hand side, the result is the most general form of the Navier-Stokes equation:

$$\rho\left[\frac{\partial \mathbf{v}}{\partial t} + (\mathbf{v} \cdot \nabla)\mathbf{v}\right] = -\nabla p_L + \nabla \cdot \bar{\bar{\tau}} + \mathbf{f_b} \tag{3.16}$$

In addition to momentum, mass must be conserved locally which is enforced by the continuity equation:

$$\frac{\partial \rho}{\partial t} + \nabla \cdot (\rho \mathbf{v}) = 0 \tag{3.17}$$

At this point, a common set of assumptions can be adopted which will greatly simplify the initial analysis of the surface-driven flow problem. These include that the liquid is isotropic, incompressible, and exhibits viscous stresses that are proportional to the local strain rate (i.e., is Newtonian). The only body force under consideration is the gravitational force. Thermodynamical effects will be neglected and a constant temperature will be assumed. Under these conditions, the governing equations reduce to

$$\rho\left[\frac{\partial \mathbf{v}}{\partial t} + (\mathbf{v} \cdot \nabla)\mathbf{v}\right] = -\nabla p_L + \mu \nabla^2 \mathbf{v} + \rho \mathbf{g} \tag{3.18}$$

$$\nabla \cdot \mathbf{v} = 0 \tag{3.19}$$

where μ is the proportionality constant between the strain rate and the stress known as the viscosity and g is the gravitational acceleration. Even under these numerous constraints, the equation of motion remains unsolvable for all but the simplest, idealized geometries. However, it is instructive to analyze the example of a closed cylindrical capillary tube as a first approximation of more generalized surface-driven flows.

3.2.2 Flow in a Cylindrical Capillary and Generalization to Porous Media

Hagen-Poiseuille flow refers to fully-developed, axisymmetric flow of a viscous fluid along the axial direction of a cylindrical channel. If the flow is laminar and steady (or varying very slowly with time), then the flow rate through the pipe varies linearly with the pressure gradient. Assuming no slip boundary conditions at the interior channel walls, the velocity profile is parabolic and given by

$$v = \frac{-1}{4\mu}\frac{\partial p_L}{\partial z}(R_{cyl}^2 - r_{cyl}^2) \tag{3.20}$$

where r_{cyl} is radial coordinate, and R_{cyl} is the radius of the cylindrical tube. The minus sign indicates that flow is in the direction opposite the pressure gradient. Integrating over the entire tube cross-section and dividing by the cross-sectional area gives the average velocity

$$v_{avg} = \frac{R_{cyl}^2}{8\mu}\frac{\Delta p_L}{z} \tag{3.21}$$

where the spatially constant pressure gradient has been replaced by the pressure drop Δp_L divided by the distance z over which the drop occurs. This result neglects inertial forces assuming they are much smaller than viscous forces. The relative magnitude of these two forces is given by the dimensionless Reynolds number $Re = \frac{\rho v(2R_{cyl})}{\mu}$. In most cases, flows with $Re < 1$ or uni-directional flows with $Re < 2000$, it is fair to assume laminarity [35]. Gravitational body forces can be incorporated with other pressure sources into a single pressure drop term. Replacing the viscous term in the Navier-Stokes with the corresponding Hagen-Poiseuille relation averaged over the cross-section gives a more tractable equation that can be integrated over a control volume that evolves with the rising meniscus of a capillary flow. Doing so yields the following equation of motion:

$$\frac{-d(\rho l\dot{l})}{dt} = \frac{-2\gamma\cos\theta_{CA}}{R_{cyl}} + \frac{8\mu l\dot{l}}{R_{cyl}^2} + \rho g l \tag{3.22}$$

where l is the height of the meniscus and $\dot{l}$ is its average velocity in the z-direction. This momentum balance is limited in scope to the specific case of capillary rise in cylindrical channels; however, it can be modified to accommodate generalized porous media.

Darcy's Law

The phenomenon of flow that varies linearly with pressure gradient and inversely with viscosity is not limited to the Hagen-Poiseuille realm. In fact, such a relationship is the norm when it comes to low Reynolds number flow through porous media. This relationship is known as Darcy's law is written as

$$v_D = \frac{-k}{\mu} \nabla p_L \tag{3.23}$$

where k is a proportionality constant known as the permeability that depends only on the structure of the porous medium in question. The Darcy velocity v_D is an effective velocity equivalent to dividing the total flow rate by the cross-sectional area of the porous medium; it is related to the average rise velocity via $v_D = \epsilon \dot{l}$, where ϵ is the material's porosity or the ratio of flow volume to total volume. With this, the Hagen-Poiseuille result can now be re-written in the more generalized equations that describe porous flow.

$$\dot{l} = \frac{R_{cyl}^2}{8\mu} \frac{\Delta p_L}{l} = \frac{v_D}{\epsilon} \tag{3.24}$$

$$\dot{l} = \frac{-k}{\epsilon \mu} \frac{\Delta p_L}{l} \tag{3.25}$$

where $\epsilon = 1$ and $k = \frac{R^2}{8}$ for a cylindrical capillary. This more general viscous loss term can be substituted into the equation of motion for capillary rise as long as two criteria are met. First, the flow must have a low characteristic Reynolds number (i.e., $Re < 1$ for highly tortuous pores or $Re < 2000$ for straight pores). Second, the capillary pressure term must be modified, since the meniscus is not generally a spherical cap with constant radius of curvature. Fries et al. recommend using a static radius R_s defined to agree with experiment in the static regime $(\frac{-2\gamma \cos\theta}{R_s} = \rho g l)$ [36]. For geometrically regular porosity such as intentionally designed microchannel or micropillar arrays, the average capillary pressure Δp_c, and therefore R_s, can be calculated a priori using the method outlined in section 3.1.3. The equation of motion is rearranged to more intuitively convey the balance of forces; surface tension is pulling against the collective resistance of the liquid's inertia, viscous friction, and weight:

$$\Delta p_c = \frac{d(\rho l \dot{l})}{dt} + \frac{\epsilon \mu l \dot{l}}{k} + \rho g l \tag{3.26}$$

3.2.3 Analytical Solutions for Different Capillary Rise Regimes

There is no known analytical solution for the liquid rise in a porous medium when all four major forces are roughly the same order of magnitude. However, from the form of the equation of motion, it is clear that at different stages during the liquid rise, different forces will dominate the flow. At $t = 0$, the instant the medium is brought into contact with an infinite reservoir of liquid, both the height of the liquid l and the velocity of the front $\dot{l}$ are equal to zero. There is a rapid acceleration due to the pull of surface tension, and inertia is the primary force resisting it. As $\dot{l}$ grows larger in response to the upward acceleration, viscous forces increase thereby reducing the acceleration and overtaking inertia as the primary resistance to flow. As l increases due to the positive acceleration and velocity, gravitational forces increase thereby reducing the acceleration and velocity further. At some point, the liquid reaches an equilibrium height where surface tension balances the weight of the liquid column. By neglecting one or more of the less significant forces at different times during the liquid rise, it is possible to derive piecewise analytical descriptions of the motion.

Static Regime

The static regime is reached when the weight of the rising liquid becomes equal in magnitude to the driving capillary force.

$$\Delta p_c = \rho g l \tag{3.27}$$

$$l = \frac{\Delta p_c}{\rho g} \tag{3.28}$$

This describes the equilibrium liquid height for the case of a generalized porous medium. For a cylindrical capillary, this expression collapses to the well known Jurin's law first discovered in the 18th century:

$$l = \frac{2\gamma \cos \theta_{CA}}{\rho g R_{cyl}} \tag{3.29}$$

Viscous Regime

The first description of the dynamics of capillary rise was given by Washburn in 1921. Starting from the Hagen-Poiseuille model, he assumed a pressure gradient that varies as the inverse of the distance penetrated into the capillary, which is equivalent to assuming a constant pressure drop between the advancing liquid front and the entrance to the capillary [37]. This balance of capillary and viscous forces results in a first-order, nonlinear differential equation that is separable and can be solved by direct integration. For the case of a uniform porous medium,

$$\Delta p_c = \frac{\epsilon \mu l \dot{l}}{k} \tag{3.30}$$

$$\frac{dl}{dt} = \frac{k \Delta p_c}{\epsilon \mu l} \tag{3.31}$$

$$\int_0^l l \mathrm{d}l = \int_0^t \frac{k \Delta p_c}{\epsilon \mu} \mathrm{d}t \tag{3.32}$$

$$l = \sqrt{\frac{2k \Delta p_c t}{\epsilon \mu}} \tag{3.33}$$

This simple square root law, known as Washburn's equation, is tremendously accurate in describing many real-life capillary phenomena where the pores are very small, which keeps the inertial regime very short and the effects of gravity insignificant until long times.

Inertial Regime

Before viscous friction and gravity become significant, inertial forces are the main resistance to the pull of surface tension. The force balance is reduced to

$$\frac{\Delta p_c}{\rho} = \frac{d(l\dot{l})}{dt} = ll + \dot{l}^2 \tag{3.34}$$

which has the solution

$$l = t\sqrt{\frac{\Delta p_c}{\rho}} \tag{3.35}$$

In the early stages, liquid height increases linearly with time. This model described by Quéré resolves the problem of infinite velocity at $t = 0$ that was encountered by earlier models [38]; however, it still suffers from an infinite acceleration and, therefore, would not be accurate at extremely short time-scales.

Visco-inertial Regime

An extended model for short time scales that retains the viscous friction term was developed by Bosanquet [39]. The equation of motion is written as

$$\frac{\Delta p_c}{\rho} = \frac{d(l\dot{l})}{dt} + \frac{\epsilon\mu}{\rho k} l\dot{l} \tag{3.36}$$

which has the solution

$$l^2 = \frac{2k\Delta p_c}{\epsilon\mu}[t - \tau_1(1 - \mathrm{e}^{\frac{-t}{\tau_1}})] \tag{3.37}$$

with $\tau_1 = \dfrac{k\rho}{\epsilon\mu}$. At short enough times, this solution reduces to the Quéré solution predicting linear height increase with time. At time increases, the model describes a decreasing velocity in better agreement with the real behavior of viscous liquids as observed in experiments. At very long times, the Bosanquet solution converges to Washburn's equation, which describes the purely viscous regime.

Visco-gravitational Regime

In addition to describing purely viscous capillary rise, Washburn worked out an implicit solution for the case where gravitational effects are also significant [37]. The balance of forces is given as:

$$\Delta p_c = \frac{\epsilon\mu l\dot{l}}{k} + \rho g l \tag{3.38}$$

$$\frac{dl}{dt} = \frac{k}{\epsilon\mu l}(\Delta p_c - \rho g l) \tag{3.39}$$

which has the implicit solution

$$t = \frac{-\epsilon\mu}{\rho g k} l - \frac{\epsilon\mu\Delta p_c}{k(\rho g)^2} \ln{(1 - \frac{\rho g l}{\Delta p_c})} \tag{3.40}$$

Later, Fries et al. came up with an explicit solution using the Lambert W function [36].

$$l = \frac{\Delta p_c}{\rho g}[1 + W(-\mathrm{e}^{-1-\frac{t}{\tau_2}})] \tag{3.41}$$

where $\tau_2 = \dfrac{\epsilon\mu\Delta p_c}{k(\rho g)^2}$. Their solution converges to a constant height at long times in agreement with Jurin's law and experimental results.

3.3 Optimization of Surface-Tension Driven Flows

This chapter began by discussing the phenomenon of surface tension, how it governs interactions at phase interfaces, and how these interactions can drive flow. The equation of motion for liquid rise in a cylindrical capillary was derived as well as a natural extension in generalized porous media. The task that remains is to use this information to optimize the design of porous structures for the passive delivery of liquid. In the context of this research, optimization means precisely controlling the flow rate of liquid to an emitter tip. However, due to the viscosity of the liquids studied, achieving a sufficient flow rate via capillary action can prove extremely difficult. For this reason, we have focused on describing the conditions for maximizing flow through various wicking geometries. Operating at a local flow rate maximum also has the advantage of lower sensitivity to dimensional variation, and the magnitude of the maximum can be adjusted by altering other parameters of the design (e.g., the length of the emitter tip).

Before delving into thorough analysis, it is immediately obvious that such a flow maximum should exist with respect to varying porosity. A medium with zero porosity will not wick any liquid so the flow rate is zero. As pore size increases, surface-tension driven flow can occur. In the limit that pores become much larger than the capillary length, $\lambda = \sqrt{\frac{\gamma}{\rho g}}$, gravity dominates surface tension and the flow rate returns to zero. According to the mean-value theorem, there must be a characteristic pore size between zero and many times the capillary length at which the derivative of flow rate with respect to pore size is zero. The trivial case is a substance that does not wick at all, perhaps because it is hydrophobic. If any wicking can occur, then a maximum of flow rate with respect to pore size will exist. Multiple local maximums may exist that depend on the effects of the meniscus, pore packing density, and viscosity in addition to those of gravity.

It is important to stress that the maximum flow rate of interest is with respect to pore size at constant meniscus height l. A maximum flow rate with respect to time at constant pore size also exists. It occurs between the inertial and viscous regimes, typically at very short times and, therefore, very short heights. Beyond this point, flow rate is always decreasing for increasing t and l. Analysis will be limited to this post-inertial regime, thus the equation of motion simplifies to

$$\Delta p_c = \frac{\epsilon \mu l \dot{l}}{k} + \rho g l \tag{3.42}$$

and we have

$$Q = \epsilon \dot{l} A = \frac{kA}{\mu l}[\Delta p_c - \rho g l] \tag{3.43}$$

where Q is the flow rate and A is the cross-sectional area of the porous medium. For certain regular, well-defined geometries, k and Δp_c can be explicitly written in terms of a characteristic pore size and an analytical optimum can be found.

3.3.1 Cylindrical Tube

For a cylindrical capillary of radius R_{cyl}, $\Delta p_c = \frac{2\gamma \cos\theta_{CA}}{R_{cyl}}$ and $k = \frac{R_{cyl}^2}{8}$. Therefore, the flow rate Q is given by

$$Q = \epsilon \dot{l} \pi R_{cyl}^2 = \frac{\pi R_{cyl}^4}{8\mu l}[\frac{2\gamma \cos\theta_{CA}}{R_{cyl}} - \rho g l] \tag{3.44}$$

Taking the derivative of Q with respect to R_{cyl} and setting it equal to zero yields

$$\frac{dQ}{dR_{cyl}} = \frac{\pi}{8\mu l}[6\gamma\cos\theta_{CA}R_{cyl}^2 - 4\rho g l R_{cyl}^3] = 0 \tag{3.45}$$

$$R_{cyl} = \frac{3}{2}\frac{\gamma\cos\theta_{CA}}{\rho g l} \tag{3.46}$$

This expression gives the optimal cylinder radius for maximizing flow rate at meniscus height l in terms of l and physical parameters. Perhaps it is more instructive to rearrange terms as follows:

$$l = \frac{3}{2}\frac{\lambda^2\cos\theta_{CA}}{R_{cyl}} = \frac{3}{4}l_{max} \tag{3.47}$$

where l_{max} is the meniscus equilibrium height for a cylinder of radius R_{cyl}. In other words, if one seeks to maximize flow rate at a height l, choose R_{cyl} such that $l_{max} = \frac{4}{3}l$.

If, instead, the goal is to maximize flow rate per unit area (i.e., Darcy velocity), we divide the previous equation by the cross-sectional area which gives

$$v_D = \epsilon\dot{l} = \frac{R_{cyl}^2}{8\mu l}[\frac{2\gamma\cos\theta_{CA}}{R_{cyl}} - \rho g l] \tag{3.48}$$

whose derivative is

$$\frac{dv_D}{dR_{cyl}} = \frac{1}{8\mu l}[4\gamma\cos\theta_{CA} - 2\rho g l R_{cyl}] \tag{3.49}$$

Setting this expression equal to zero gives the optimum radius

$$R_{cyl} = \frac{\lambda^2\cos\theta_{CA}}{l} \tag{3.50}$$

or the alternate expression

$$l = \frac{1}{2}\frac{\lambda^2\cos\theta_{CA}}{R_{cyl}} = \frac{1}{2}l_{max} \tag{3.51}$$

For maximizing v_D at a height l, R_{cyl} should be chosen such that $l_{max} = 2l$. For a typical electrospinning solution in this research ($\lambda = 2.11$ mm and $\cos\theta_{CA} = \frac{\sqrt{3}}{2}$), the optimum cylinder radius that maximizes v_D at a meniscus height of 5 mm is $R_{cyl} = 772\ \mu m$. The radius that optimizes v_D is smaller than that which optimizes overall flow rate by a factor of $\frac{2}{3}$. This means that increasing the cylinder radius beyond the v_D optimum will increase flow rate but not as quickly as it increases cross-sectional area. If the goal is the maximize flow within a constrained area, as it is in this research, then the v_D optimum is the more relevant criterion.

Before extending these arguments to other geometries, it is instructive to non-dimensionalize the problem. The average velocity in a cylindrical capillary $\dot{l}$ can be non-dimensionalized by the quantity $\frac{\gamma}{\mu}$ to yield the capillary number Ca, which is an indication of the ratio of viscous to surface tension forces:

$$\frac{\mu\dot{l}}{\gamma} = Ca = \frac{k}{\epsilon l}[\frac{2\cos\theta_{CA}}{R_{cyl}} - \frac{\rho g l}{\gamma}] \tag{3.52}$$

This expression can be generalized by realizing that, in surface tension-driven, low Reynolds number flows through porous media, the permeability goes as the square of some characteristic length R_{char} times a function of geometrical ratios f_1. Capillary pressure goes as the inverse of R_{char} times a different function of geometrical ratios f_2. Since flow rate per unit area is the metric of interest, we should multiply the capillary number by ϵ to give a Darcy-equivalent capillary number Ca_D.

$$\epsilon Ca = Ca_D = \frac{f_1 R_{char}^2}{\lambda^2}[\frac{\lambda^2 f_2 \cos\theta_{CA}}{l R_{char}} - 1] = f_1 R_{char}^{*2}[\frac{f_2\cos\theta_{CA}}{l^* R_{char}^*} - 1] \tag{3.53}$$

Capillary number is a function a dimensionless characteristic length $R_{char}^* = \frac{R_{char}}{\lambda}$, a dimensionless meniscus height $l^* = \frac{l}{\lambda}$, contact angle, and other dimensionless ratios of geometrical parameters. The non-dimensional scaling can be extended to total flow rate using $Q^* = \frac{A}{\lambda^2}\mathrm{Ca}_D$. Figure 3-5 shows Ca_D and Q^* as a function of R_{char}^* at different l^* for the case of a perfectly wetting cylindrical capillary ($i.e., \cos\theta_{CA} = 1; f_1 = \frac{1}{8}; f_2 = 2$).

The non-dimensionalization given in terms of the characteristic pore size R_{char}^* is convenient to demonstrate the flow maximum with respect to this parameter. How-

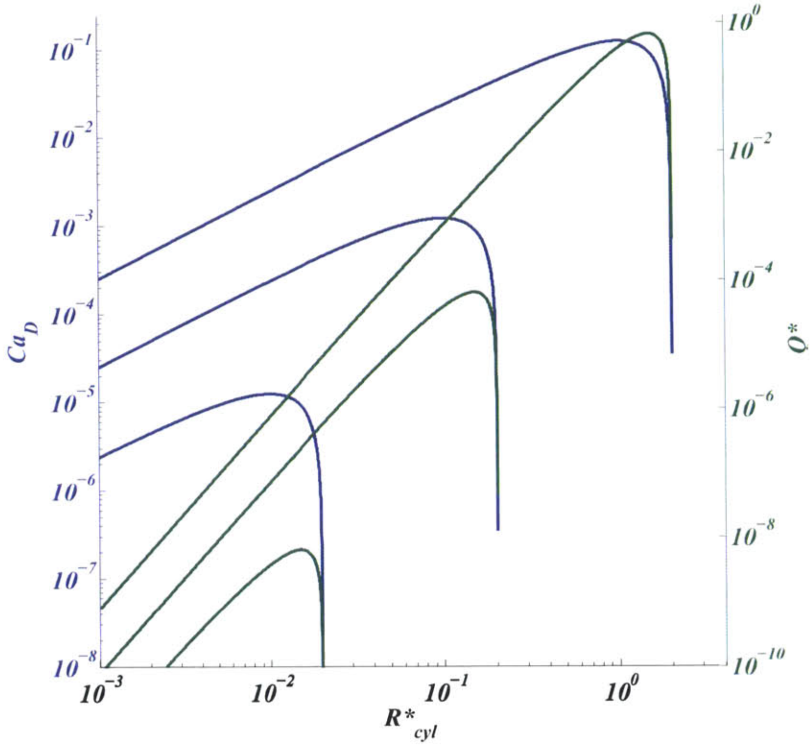

Figure 3-5: Flow rate Q^* and Darcy velocity Ca_D vs. cylinder radius (dimensionless variables) plotted for dimensionless meniscus height $l^* = 1, 10, 100$ (from top to bottom in plot): Ca_D is maximized at a smaller capillary radius than that which maximizes Q^*.

ever, another form can be written in terms of more conventional dimensionless numbers of fluid dynamics:

$$\epsilon Ca = Ca_D = DaBo[\frac{1}{L} - 1] \tag{3.54}$$

where the Darcy number $Da = \dfrac{k}{\epsilon A} = \dfrac{f_1 R_{char}^2}{\epsilon A}$ is the ratio of the permeability to the average pore cross-section, the Bond number $Bo = \dfrac{\epsilon A}{\lambda^2}$ is the ratio of gravitational forces to capillary forces, and $L = \dfrac{l^*}{l^*_{max}}$ is the ratio of the meniscus height to its final static height.

3.3.2 Microchannels and Micropillars

The challenge of extending the previous analysis to more complicated structures lies in accurately defining the capillary pressure Δp_c, the permeability k, and the porosity ϵ in terms of geometrical parameters. The method for calculating average capillary pressure outlined in section 3.1.3 works well when meniscus effects are negligible - for example, when the height of a wicking structure is much greater than its other dimensions. When this is not the case, the method must be adjusted to account for the greater liquid surface area and reduced liquid volume that result from a non-negligible meniscus. The approach we use is explained in Appendix A.

For a series of open, rectangular microchannels of height h, width w, sidewall thickness d, and pitch $p_M = w + d$ (See Figure 3-4), we have derived the following relationships:

$$\epsilon_{chan} = F_{V,chan}\left[1 - \frac{d}{p_M}\right] \tag{3.55}$$

$$k_{chan} = \frac{w^2}{12}F_{V2,chan}\left[1 - \frac{d}{p_M}\right]\left[1 - \frac{31\zeta(5)}{30\zeta(4)}\frac{w}{\pi h}\tanh\left(\frac{\pi h}{w}\right)\right] \tag{3.56}$$

$$\Delta p_{c,chan} = \frac{\rho g l}{F_{V,chan}}\left[\frac{\lambda^2}{hl}\left(\left[1 + 2\frac{h}{w}\right]\cos\theta_{CA} - F_{A,chan}\right) - F_{V,chan}\right] \tag{3.57}$$

$\zeta(n)$ represents the Riemann zeta function evaluated at the value n. $F_{A,chan}$ is a correction factor that multiplies the projection of open liquid surface to give the true meniscus surface area. $F_{V,chan}$ is a correction factor that multiplies the ideal, full-pore volume to give the actual pore volume. $F_{V2,chan}$ is a correction factor that accounts for the fact that the flow rate lost to the meniscus is not necessarily proportional to the flow volume lost. If the void of the meniscus is located at what would otherwise be the fastest part of the velocity profile, then the flow rate lost is actually greater than the average void cross-section times the average velocity. Plugging into Darcy's law and non-dimensionalizing yields model 1 (i.e., flow in open microchannels with meniscus and gravitational effects):

$$Ca_D = \epsilon_{chan}\frac{F_{V2,chan}}{F_{V,chan}}\left[\frac{w^{*2}}{12}\left(1 + \frac{d}{w}\right)^{-1}\right]\left[1 - \frac{31\zeta(5)}{30\zeta(4)}\frac{w}{\pi h}\tanh\left(\frac{\pi h}{w}\right)\right] \left[\frac{(1 + 2\frac{h}{w})\cos\theta_{CA} - F_{A,chan}}{l^*h^*} - F_{V,chan}\right] \tag{3.58}$$

Xiao et al. use a similar approach to describe the capillary pressure in micropillar forests; however, they neglect gravitational effects. They derive an expression for the permeability using Brinkman's equation and approximate the correction factors that we call F_A and F_V using meniscus profile simulations [40]. We add gravity and correction factor F_{V2} to their model and state the resulting relationships here:

$$\epsilon_{pill} = F_{V,pill}\Big[1 - (\frac{d}{p_M})^2\Big] \tag{3.59}$$

$$k_{pill} = p_M^2 k_{Num} F_{V2,pill}\Big[1 - (\frac{d}{p_M})^2\Big]\Big[1 - \frac{p_M}{h}\sqrt{\frac{k_{Num}}{\epsilon_{pill}}}\tanh\Big(\frac{h}{p_M}\sqrt{\frac{\epsilon_{pill}}{k_{Num}}}\Big)\Big] \tag{3.60}$$

$$k_{Num} = \Big(ln(\phi_s^{-1/2}) - 0.738 + \phi_s - 0.887\phi_s^2 + 2.038\phi_s^3 + o(\phi_s^4)\Big)\ [41] \tag{3.61}$$

$$\Delta p_{c,pill} = \frac{\rho g l}{F_{V,pill}}\Big[\frac{\lambda^2}{lh}\Big(\frac{1 + 2\frac{d}{w}(1 + 2\frac{h}{w})}{1 + 2\frac{d}{w}}\cos\theta_{CA} - F_{A,pill}\Big) - F_{V,pill}\Big] \tag{3.62}$$

Plugging into Darcy's law and non-dimensionalizing yields model 2 (i.e., flow in open micropillar forests with meniscus and gravitational effects):

$$Ca_D = \epsilon_{pill}\frac{F_{V2,pill}}{F_{V,pill}}\Big[w^{*2}\Big(1+\frac{d}{w}\Big)^2 k_{Num}\Big]\Big[1-\frac{w}{h}\Big(1+\frac{d}{w}\Big)\sqrt{\frac{k_{Num}}{\epsilon}}\tanh(\frac{h}{w}\Big(1+\frac{d}{w}\Big)^{-1}\sqrt{\frac{\epsilon}{k_{Num}}})\Big] \\ \Big[\frac{1}{l^*h^*}\Big(\frac{1 + 2\frac{d}{w}(1 + 2\frac{h}{w})}{1 + 2\frac{d}{w}}\cos\theta_{CA} - F_{A,pill}\Big) - F_{V,pill}\Big] \tag{3.63}$$

Both models describe the flow rate per unit area in terms of the characteristic flow width w, the flow region's aspect ratio $\frac{h}{w}$, the packing density of the microfeatures $\frac{d}{p_M}$, and the meniscus height l. However, there is a key difference between the two models with regards to their dependence on the packing density. In model 1, the flow within an individual microchannel of height h and width w does not depend on the packing density. Since each microchannel is entirely closed off from its neighbors, the flow through its cross-section can not depend on how near or far the next neighbor lies. Packing density only enters the calculation when considering the flow from a series of channels averaged over their spatial extent (i.e., the Darcy velocity). In model 2, packing density is far more significant. The capillary pressure and permeability depend strongly on packing density, and the flow between two rows of pillars is coupled to the flow through the neighboring rows. An important conclusion from this analysis is that the Darcy velocity can be maximized in arrays of microchannels by taking the sidewall thickness d as narrow as possible while w, h, and l are held constant. This is not true for micropillar forests since taking the pillar side-length d towards zero reduces the capillary pressure to zero.

In the contour plots that follow, dimensionless Darcy velocity is plotted against dimensionless microfeature pitch $p_M^* = \frac{p_M}{\lambda}$ and $\frac{d}{p_M}$ for various values of l^* and h^*. When $h^* \times l^* \ll 1$, meniscus effects dominate and maximum flow occurs when w^* is on the order of h^*. For larger widths, the decreasing aspect ratio means the meniscus void becomes a growing portion of the flow cross-section until it eventually intersects the bottom surface. When $h^* \times l^* \gg 1$, gravitational effects dominate and maximum flow occurs when w^* is on the order of $\frac{1}{l^*}$. When $h^* \times l^* \approx 1$, both gravitational and meniscus effects are significant (Figure 3-6, Figure 3-7, Figure 3-8). For micropillar forests, contours are plotted for values of $\frac{d}{p_M} < 0.5$ (i.e., the region in which the numerical permeability model is valid).

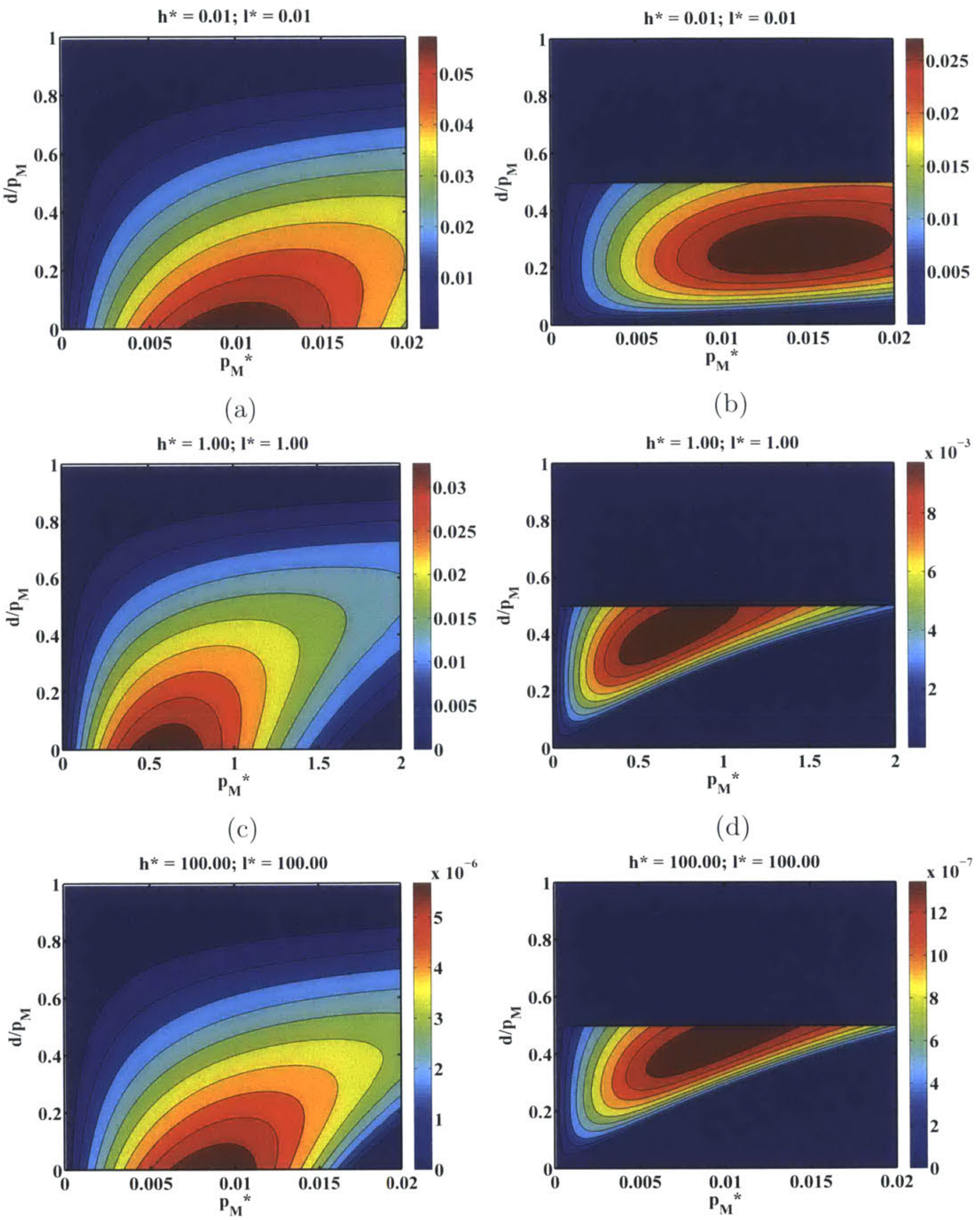

(a) (b) (c) (d) (e) (f)

Figure 3-6: Contour plots of dimensionless Darcy-effective capillary number Ca_D vs. dimensionless pitch p_M vs. packing ratio $\frac{d}{p_M}$ for various combinations of dimensionless microfeature height h^* and meniscus height l^* (Highlight different regimes):(a) Model 1, meniscus regime (b) Model 2, meniscus regime (c) Model 1, mixed regime (d) Model 2, mixed regime (e) Model 1, gravitational regime (f) Model 2, gravitational regime.

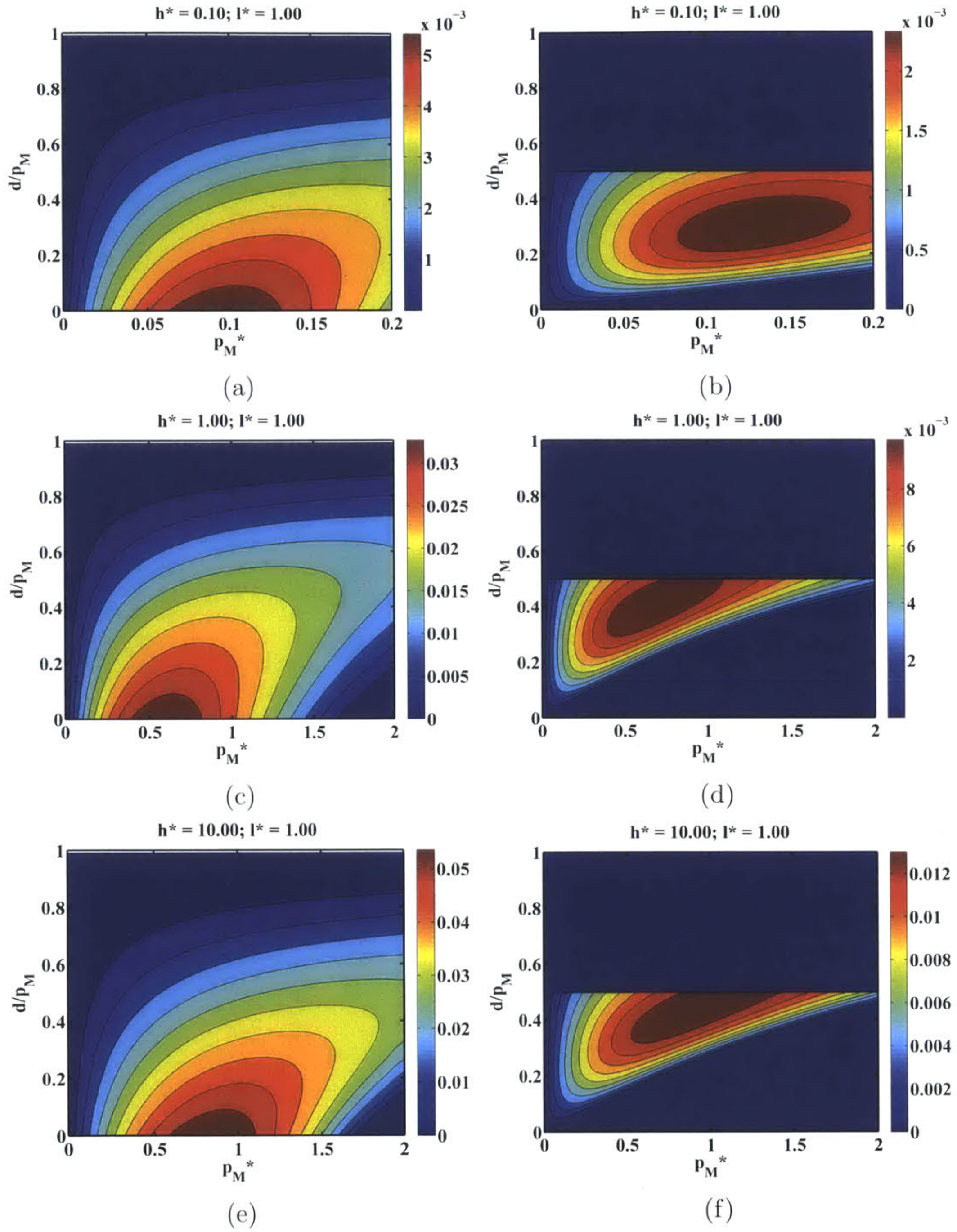

Figure 3-7: Contour plots of dimensionless Darcy-effective capillary number Ca_D vs. dimensionless pitch p_M vs. packing ratio $\frac{d}{p_M}$ for various combinations of dimensionless microfeature height h^* and meniscus height l^* (Highlight effect of h^*): (a) Model 1, meniscus regime (b) Model 2, meniscus regime (c) Model 1, mixed regime (d) Model 2, mixed regime (e) Model 1, gravitational regime (f) Model 2, gravitational regime.

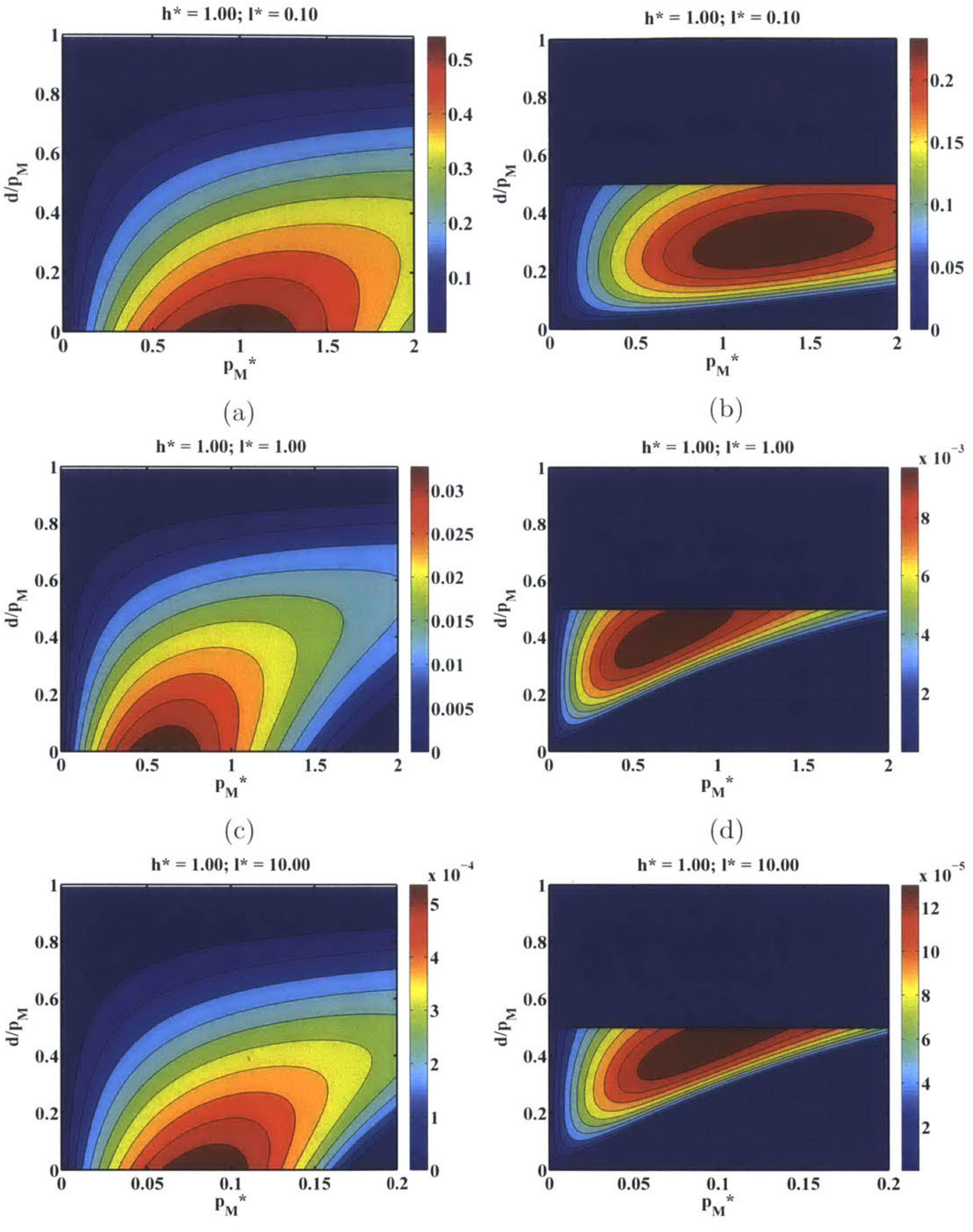

(a) (b)

(c) (d)

(e) (f)

Figure 3-8: Contour plots of dimensionless Darcy-effective capillary number Ca_D vs. dimensionless pitch p_M vs. packing ratio $\dfrac{d}{p_M}$ for various combinations of dimensionless microfeature height h^* and meniscus height l^* (Highlight effect of l^*): (a) Model 1, meniscus regime (b) Model 2, meniscus regime (c) Model 1, mixed regime (d) Model 2, mixed regime (e) Model 1, gravitational regime (f) Model 2, gravitational regime.

Chapter 4

Design and Fabrication of Externally-fed Emitter Arrays

4.1 Basic Design Concept

The previous two chapters have detailed some of the scientific background that describes electro-hydrodynamic jetting and surface tension-driven flow. This chapter will explain how that scientific knowledge informed the design of externally-fed emitter arrays. In this context, "emitter" simply means a structure that enables localized jetting. Traditionally, the emitter for internally-fed, actively-pumped electro-hydrodynamic jetting is a metal needle attached to a syringe pump. These syringe needles generally have high aspect-ratios and small tip radii, which generates a large electric field enhancement thereby lowering the critical applied voltage necessary to initiate jetting. Externally-fed emitters would benefit from the same type of geometry. In fact, increasing the aspect-ratio and decreasing the tip radius are the primary design knobs to counter the loss of field enhancement, which occurs when ordering elements in a 2D array, due to electrical shielding of centrally located emitters compared to those closer to the edge.

A second main design consideration is how to incorporate wicking structures onto the emitter surface to enable passive, surface tension-driven flow of liquid to the emission site at the tip. Regardless of the type of wicking structure or its fabrication method, two general principles emerge from the physics of wicking: first, a wider emitter will accommodate a greater flow rate and, second, a shorter emitter length will correspond to a higher flow rate at its tip. This presents a trade-off with the electrical design criteria, which called for narrower, longer emitters.

The admissible length scales of the design are related to the capillary length $\lambda = \sqrt{\frac{\gamma}{\rho g}}$ of the working liquid. In order to sufficiently localize emission, emitters that operate from a liquid reservoir must stick out above the surface of the bulk liquid. If the emitters are approximated as solid cylinders, then the height that the liquid meniscus will climb up their outside surface is given approximately by h_{climb}:

$$h_{climb} = b \ln(\frac{2\lambda}{b}) \tag{4.1}$$

where b is the cylinder radius [42]. This means the meniscus will climb a distance on the order of λ for b on the order of λ. For $b \ll \lambda$, the meniscus climbs a distance several times b. To be clear, h_{climb} is the height of the meniscus external to the emitter structure; liquid can rise higher than this by propagating through wicking structures on the emitter surface. In general, then, a safe design criterion is that the length of the emitter l_e be at least several times greater than the approximate radius of the emitter. In order for surface tension to sustain flow against gravity, the wicking structures on the emitters must have a characteristic length on the order of λ or less. Smaller structures can wick to a higher elevation but generally exhibit slower dynamics than structures on the order of λ. All of these criteria suggest a hierarchy of length scales: an emitter should be several times longer than it is wide, and the wicking structures should be no larger than this emitter width (so they fit on the emitter). We chose to explore designs with sub-millimeter wicking structures on millimeter-scale emitters.

A microfabrication approach was conceived that accommodates the hierarchical length scales inherent in such a design. Linear (one-dimensional) arrays of millimeter-scale tall emitters are monolithically patterned on a silicon wafer and micro-scale wicking features are patterned on its top and bottom surfaces. With a nested mask design, deep reactive ion etching (DRIE) is used to etch the wicking structures and through-etch the profile of the linear emitter arrays, effectively "cookie-cutting" them out of the silicon wafer. DRIE allows for very straight sidewalls and high precision of these parts. The emitter blade cut-outs are then precisely assembled into a microfabricated slotted base, by virtue of their high dimensional accuracy, to form the two-dimensional emitter arrays, which are on the order of centimeters in size (Figure 4-1). In addition to fine dimensional control, the use of traditional microfabrication gives the flexibility to incorporate well-controlled coatings (e.g., $SiO_2, SiN, CNTs, etc.$). The choice of DRIE as the etching method comes with some limitations in regards to possible geometries that can be fabricated; this will be discussed later in the text.

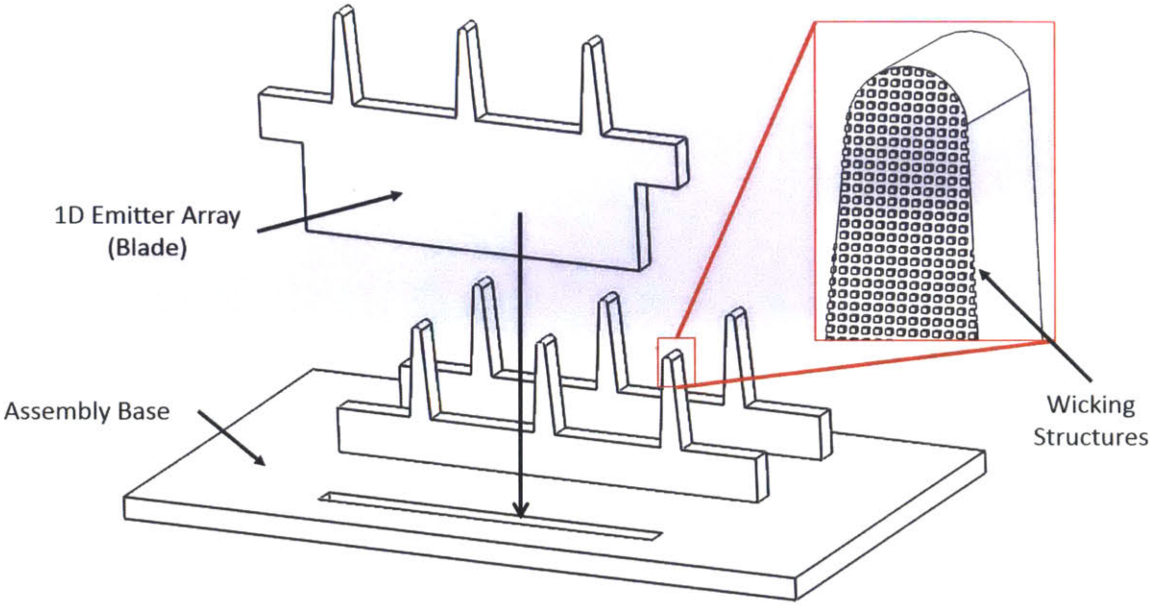

Figure 4-1: Schematic of emitter array design concept: Emitter blades with surface wicking structures are assembled into a slotted base to form a 2D array.

4.2 First-generation Devices

4.2.1 Surface Microstructures

Design Considerations

The first generation of wicking structures was limited to micropillar geometries. "Forests of micropillars" have been characterized for their wicking properties in past studies [43]. One paper in particular, by Xiao et. al. discusses a theoretical optimum liquid propagation rate that results from the scaling of viscous and surface tension forces with certain ratios of the pillar dimensions [40]. In Figure 4-2, h is the pillar height, d is the pillar diameter, p_M is the pillar pitch, and G is the spreading coefficient that describes the rate of liquid propagation ($l = G\sqrt{t}$).

It was decided to explore the design space around this optimum using hexagonally-packed micropillar forests, rather than the square-packed pillars used in the study of Xiao et al. (Figure 4-3). Hexagonally-packed pillars require a smaller "jump" of the liquid front as it progresses forward than square-packed pillars of comparable dimensions; however, they also present slightly greater viscous resistance [41]. Either way, in the hemi-wicking regime, increasing the height of the micropillars increases the thickness of the advancing film and, therefore, the flow rate per unit width of surface. Since this is the metric of interest, it was decided to maximize the height of the pillars within the limits of the fabrication approach.

The ultimate limit for the height of the micropillars is the thickness of the silicon

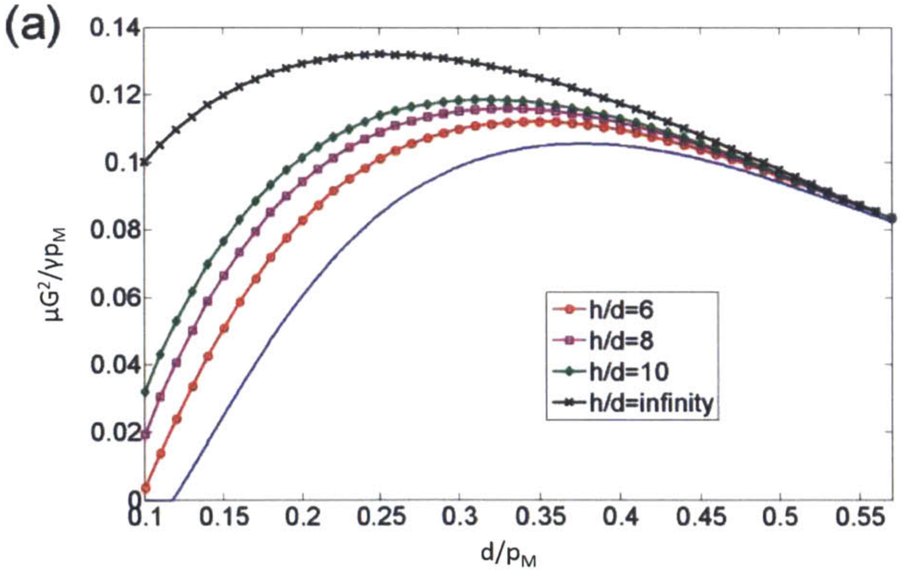

Figure 4-2: Dimensionless spreading coefficient vs. packing ratio ($\frac{d}{p_M}$) for different pillar aspect ratios ($\frac{h}{d}$): This plot, taken from reference [40], shows the flow maximum that arises from the scaling of viscous and capillary forces in square-packed arrays of pillars with circular cross-section.

wafer used as substrate, or slightly less than half of that thickness if pillars are to be etched on both sides. Fabrication was performed on 500 μm-thick silicon wafers, which put a practical upper limit of $\sim$ 200 μm on the pillar height. When DRIE etching micropillars whose heights are much greater than their width, certain restrictions exists on the pitch of the pillars if straight sidewalls are desired. As a general rule, pillars with a pitch more than twice their width run the risk of becoming undercut for deep etches. Also, for an etch window on the order of microns surrounding each pillar, an etch depth of roughly 20 times the etch window can be reasonably achieved; greater pillar aspect ratios tend to self-terminate their etch since reacting ion species can no longer reach the pillar base in sufficient number.

These fabrication limitations posed an issue since the desired optimum flow for very tall pillars is expected to exist for width-to-pitch ratios between 1:4 and 1:3 (see Figure 4-2). Exploring the space both above and below the optimum would require even smaller width-to-pitch ratios, which run significant risk of being entirely chopped off via undercutting. The solution was to initially etch pillars with width-to-pitch

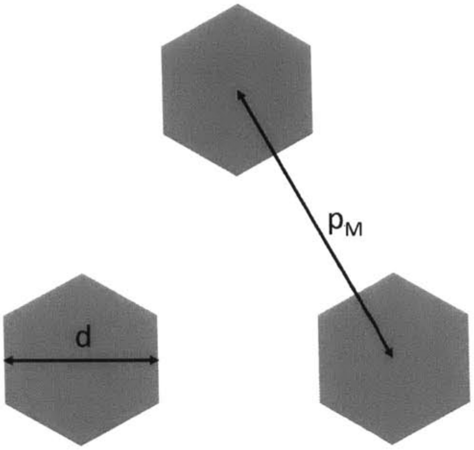

Figure 4-3: Schematic of hexagonally-packed micropillars with hexagonal cross-section: Microfeature size d and microfeature pitch p_M are labeled in the schematic.

Sample #	d [μm]	p_M [μm]
1	10	20
2	15	20
3	15	25
4	15	30
5	20	30
6	25	30
7	35	40

Table 4.1: Design space of first-generation wicking structures: Sample # 1 is best suited for exploring the flow optimum since these pillars can be thinned via oxidation to approach the optimal packing densities shown in Figure 4-2.

ratios near the safe 1 : 2 value and subsequently reduce the pillar width via oxidation followed by etching of oxide. This process can decrease pillar width by roughly 1 μm with each cycle, and it can be repeated; however, practical considerations of time and cost limit reasonable processing to a few cycles. Therefore, initial pillar widths of ten microns represent a practical upper limit, since it would take 3-5 thinning cycles to put the width-to-pitch ratio between 1:4 and 1:3 for a pitch of 20 μm (i.e. twice the width). A range of pillar dimensions, beyond the expected optimum, were fabricated to explore liquid behavior on such surfaces (Table 4.1).

Fabrication Process

The first round of fabrication performed was intended to produce micropillar forests of varying dimensions to examine their effect on liquid wetting properties. A schematic of the process flow is shown in Figure 4-4. It begins with a 500 μm thick, n-type single-crystal silicon wafer that is single-side polished. The wafer is baked in an oven where it is exposed to vapor phase HMDS , which forms a monolayer on the wafer surface that improves the adhesion of photoresist. The wafer is then spin-coated with 1 μm of OCG 825 photoresist and pre-baked at 90 $°C$ for 30 minutes to remove solvent. Micropillar features are exposed in the photoresist via contact photolithography using a 2.5 second exposure on the EV-1 mask aligner. After lithography, the features are developed using OCG 934 developer and then spin-rinsed clean. This is followed by a post-bake at 120 $°C$ which improves the selectivity of the photoresist to silicon in the subsequent DRIE step.

The micropillar features are etched using DRIE with the Bosch process which alternates SF_6 etching with C_4F_8 passivation to achieve straight sidewalls. When the desired etch depth is reached, photoresist and DRIE polymers are removed via ashing in 100 W oxygen plasma. Then, a "piranha clean" utilizing 3:1 per volume sulfuric acid:hydrogen peroxide is performed followed shortly thereafter by a full RCA clean to prepare the wafers for the diffusion tubes. Wet thermal oxide is grown at a temperature of 1025 $°C$ to a thickness of 1 μm. At this point, the pillar thickness can be reduced with a buffered oxide etch (BOE). Further thickness reduction is possible

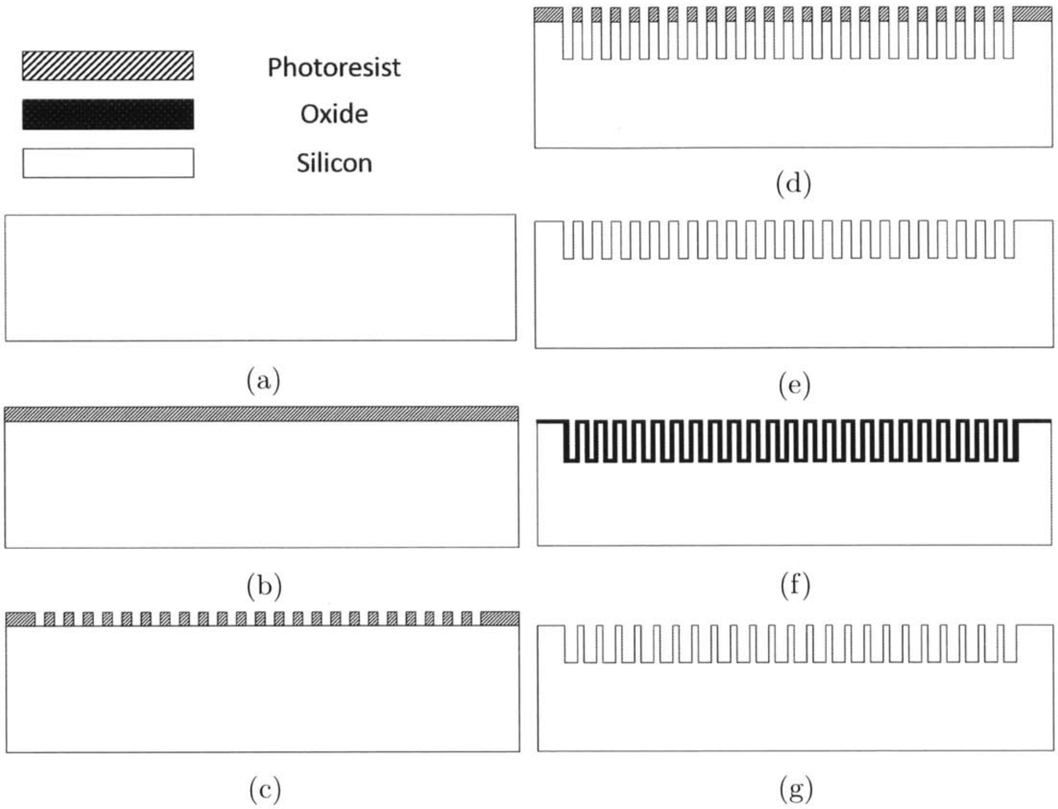

Figure 4-4: Process flow for first-generation wicking structures: (a) Start with 500 μm thick silicon wafer (b) Spin-coat with 1 μm thin photoresist (c) Expose and develop micropillar cross-sections in photoresist (d) DRIE pillars using photoresist as masking layer (e) Remove DRIE polymers and photoresist in oxygen plasma (f) Grow 1 μm thermal oxide at 1025 °C (g) Etch oxide to thin the micropillars.

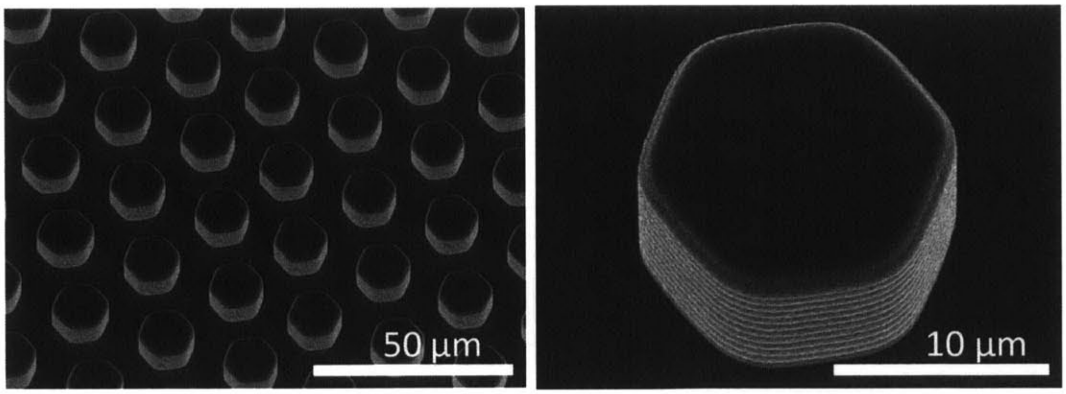

(a) (b)

Figure 4-5: Fabricated first-generation micropillars: (a) Hexagonally-packed micropillars with 15 μm diameter, 10 μm height, and 25 μm pitch. (b) Close-up of a single micropillar reveals sidewall scalloping from DRIE etch.

by repeating wet oxidation and BOE several times. Once the desired pillar geometry is attained, final surface coatings can be applied using LPCVD or sputtering of a metal. An example of the micropillars fabricated with this process is included in Figure 4-5.

4.2.2 Emitter Arrays

Design Considerations

The emitter blades etched out of the silicon wafer are defined by three primary dimensions: the length l_e, tip radius R_{Tip}, and spacing s of the emitters. It was previously mentioned that there exists a trade-off between fluid flow and electrical design considerations. Taller, narrower emitters favor greater electric field enhancement but reduce the total flow rate at the tip as compared with short, wider emitters. For micropillars on the scale previously discussed, we can obtain an order of magnitude estimate of the maximum emitter length capable of supporting flow rates needed for electrospinning. From Darcy's law, we have:

$$Q_{min} = 4R_{Tip}hv_D = \frac{2R_{Tip}hG^2}{l_{e,max}} \tag{4.2}$$

$$l_{e,max} = \frac{(0.13)2R_{Tip}hp_M\gamma}{\mu Q_{min}} \tag{4.3}$$

The value of 0.13 is the maximum dimensionless spreading coefficient $\left(\frac{\mu G^2}{\gamma p_M}\right)$ for infinitely tall pillars described by Xiao et al. and plotted in Figure 4-2. For a low-end electrospinning flow rate of $5.6 \times 10^{-11}\left[\frac{m^3}{s}\right]$ [7], a viscosity of 1 $[Pa \cdot s]$, and a tip radius of 250 μm, $l_{e,max}$ is 0.3 mm. This length is approximately equal to the tip radius and, therefore, would not protrude enough from the liquid bath to strongly localize emission (see Section 4.1). Experiments using electrospray emitters on this scale from other research [25] confirmed a lack of localization; instead, jets wandered in a manner typical of free-surface electrospinning. This calculation suggests that the previously designed micropillar wicking structures are not capable of supplying sufficient flow rates for electrospinning at large enough emitter lengths for localization. The researchers had not realized this at the time of the first design iteration. Due to uncertainty over wicking behavior in the presence of electrical forces (neglected in the calculation), a range of emitter designs were developed with varying length, tip radius, and spacing (Table 4.2).

Sample #	Emitters/Blade	s $[mm]$	$R_{Tip}[\mu m]$	l_e $[mm]$
1	3	3	250	0.5
2	3	3	250	1
3	5	3	250	1
4	3	3	250	2
5	3	3	125	1
6	5	1.5	125	0.5
7	3	3	50	5

Table 4.2: Design space of first-generation emitters: The first-generation emitter arrays were defined by the number of emitters per blade, the spacing "s," the tip radius "R_{Tip}," and the length "l_e".

The other consideration guiding the selection of emitter dimensions is their electric field enhancing characteristics. These were briefly explored with 3D simulations in COMSOL. A number of different geometries were simulated, but the output seemed to indicate roughly the same max enhancement factor. Breaking down the 3D simulation results for one particular design into two perpendicular planes (x-y and x-z) revealed the issue (Figure 4-6). The sharp corners produced at the front and back of the emitter (x-z plane) that result from DRIE etching provide the dominant field enhancement as compared to the relatively large radius of curvature in the perpendicular direction (x-y plane). These sharp corners have infinite curvature in the solid model portrayed in Figure 4-6, which is obviously not the case for a real emitter blade. Since the simulations did not include a specific definition of the sharp corner radius, the output depends on the fineness of the mesh created and is, therefore, unreliable. However, the highest enhancement factor in the x-y plane, where the designed radius of curvature is 50 μm, has a reasonable value of 2.22. It is reasonable because our emitter has no curvature in the x-z plane at the center-apex. Therefore, very close to this center-apex, the field should be similar to that of an infinite half-cylinder on a grounded plane, whose highest enhancement factor is 2. The simulated emitter tip is actually 5 mm above the grounded plane, which has the effect of slightly increasing the enhancement factor (in rough agreement with the simulation result). The important takeaway, however, is that the sharp corners resulting from the DRIE process provide the dominant field enhancement. This has the desired effect of producing the strongest fields at the edges where the liquid is supposed to wick.

Field Enhancement Factor β = local field strength/far field strength

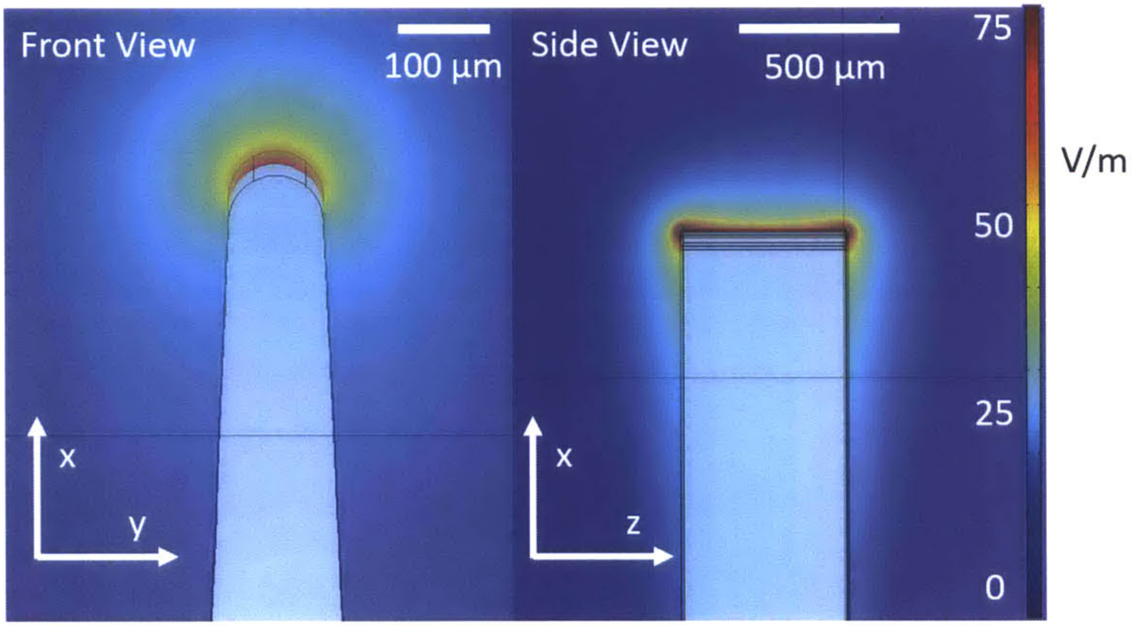

$E_{\text{apex, center}} = 73.91$ [V/m]
$\beta_{\text{apex, center}} = 2.22$

$E_{\text{apex, corners}} = 257.17$ [V/m]
$\beta_{\text{apex, corners}} = \beta_{\text{Max}} = 7.72$

*** Simulation carried out for 1 [V] at 3 [cm] working distance**

Figure 4-6: Electric field simulation around emitter tip: Electric field enhancement is greatest at the sharp front and back edges that result from DRIE (see side view).

A final important design aspect with regards to ease of fabrication is the inclusion of "tethers" on the emitter blades. These are thin beams of silicon at points around the emitter blade perimeter that are intentionally not etched. They keep the blades connected to the rest of the wafer in a few locations after the rest of the outline has been completely through-etched. This allows for continued processing of the wafer as one unit. When processing is complete the emitter blades can be removed by breaking the tethers manually with a pair of tweezers.

Fabrication Process

The fabrication of first-generation emitter blades with integrated roughness begins with a 500 μm thick, n-type single-crystal silicon wafer that is double side polished and coated with 0.5 μm of thermal oxide. Assuming 150:1 selectivity of thermal oxide to silicon, the starting oxide layer provides a sufficient mask to etch features roughly 75 μm deep. In order to allow for deeper features and build in an extra factor of safety, additional oxide was deposited. This first requires a standard RCA clean of the wafer. Following the clean, 1 μm of oxide is deposited on the surface via PECVD, and the wafer is annealed for one hour in nitrogen at 950 $°C$. This densifies the oxide layer and improves its etch selectivity.

Patterning of the oxide layer via photolithography entails similar steps as those described to fabricate the micropillars alone. They are: HMDS deposition, spin-coating of 1 μm OCG 825, 30 minute pre-bake at 90 $°C$, exposure, development in OCG 934, spin rinsing, and 30 minute post-bake at 120 $°C$. A new step at this point is RIE of the oxide layer under the photoresist with the AME 5000. This transfers the micropillar pattern from the thin photoresist into the oxide. Once this is complete, the photoresist is removed via ashing in oxygen plasma, and the wafer is ready for more photolithography (Figure 4-7).

The second round of photolithography transfers the emitter blade outline. It begins, as before, with the deposition of HMDS for improved adhesion of resist. This time around thicker resist is used, since it provides a more durable masking layer for through-wafer etching and is compatible with the larger etch window ($\approx 80\mu m$). The wafer is spin-coated with 10 μm of AZ 4620 thick resist and pre-baked for 60 minutes at 90 $°C$. The emitter blade outline is exposed in the thick resist with two 10 second exposures followed by development, spin-rinsing, and 30 minute post-bake at 120 $°C$.

At this point, the 80 μm etch window around the emitter blade has been cleared of resist but still contains the underlying oxide film (which may or may not be patterned with microfeatures depending on the location). This oxide is removed with another

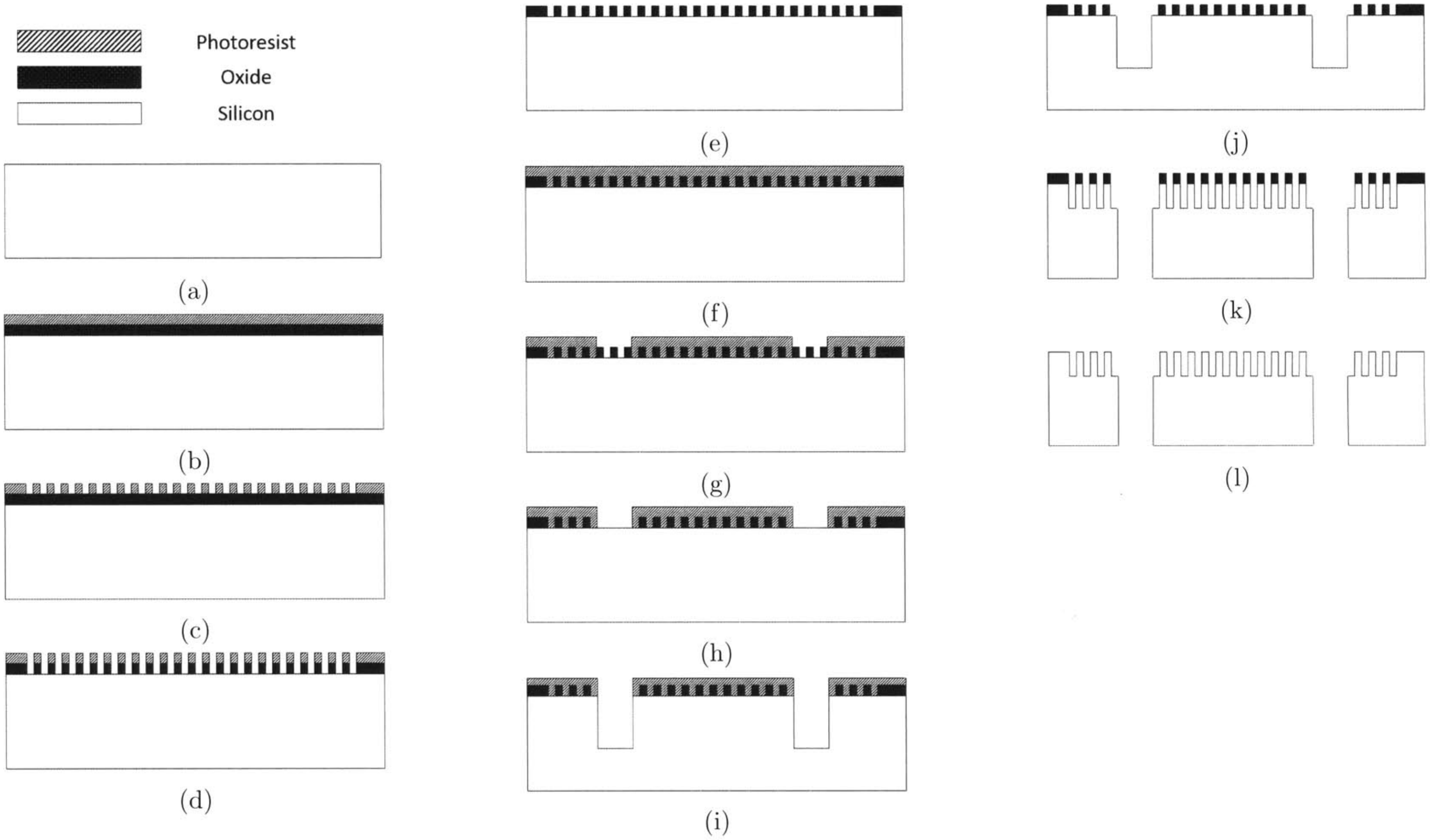

Figure 4-7: First-generation emitter blade process flow: (a) Start with DSP, 500 μm thick silicon wafer (b) Deposit and anneal oxide, then spin-coat with photoresist (c) Expose and develop microfeatures in photoresist (d) RIE microfeatures into nested oxide mask (e) Remove photoresist in oxygen plasma (f) Spin-coat thick resist on top-side (g) Expose and develop emitter blade outline in thick resist (h) RIE to clear oxide from blade outline etch window (i) DRIE of emitter blade profile from top-side to partial depth (j) Oxygen plasma and piranha clean to remove thick resist (k) Simultaneous DRIE of top-side microfeatures and remaining depth of emitter profile using nested oxide mask (l) Etch away oxide mask and break tethers to remove emitter blades.

reactive ion etch, which clears the way for the DRIE through-etch of the silicon. After this, the emitter blade outlines are etched with DRIE from the top-side to a depth between 75% and 90% of the total wafer thickness depending on the desired final micropillar depth. The wafer is ashed in oxygen plasma and then piranha-cleaned to remove DRIE polymers and photoresist.

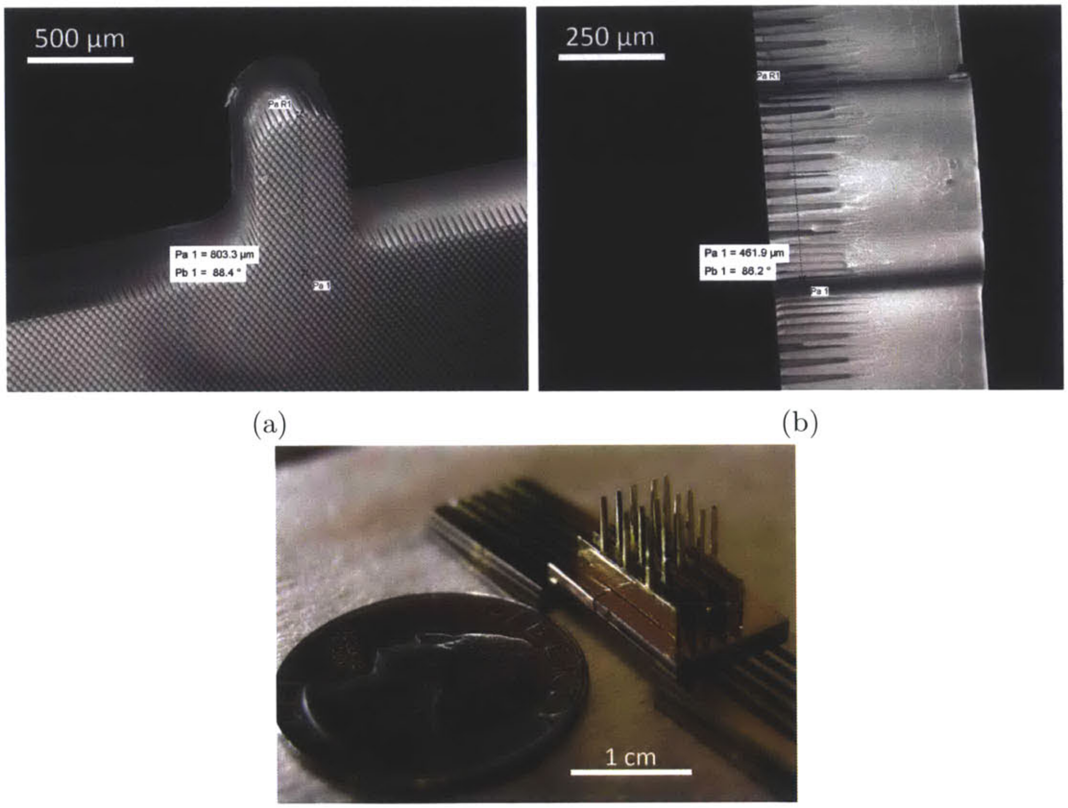

(a) (b)

(c)

Figure 4-8: Fabricated first-generation emitter arrays: (a) Front-view of 1 mm tall emitter tip with micropillar features on one side. (b) Top-view of the same emitter tip. (c) Fully-assembled, gold-coated array next to a quarter for size comparison. The array contains 15, 5 mm-tall emitters in a 3×5 arrangement with an average density of ≈ 22 emitters per square cm.

The silicon wafer must then be mounted on a quartz wafer with photoresist to prepare for the DRIE through-etch. This etch is performed from the top-side of the wafer using the patterned oxide layer as a mask. It simultaneously etches the microfeatures and completes the remaining 10-25% of the through-etch. When it is complete, the silicon wafer must be released from the quartz wafer with acetone soaking. Due to the implementation of the previously mentioned silicon tethers, the wafer remains in one piece upon release. This allows for post-processing (i.e., film deposition, oxidation thinning, etc.) to be performed on the entire wafer simultaneously. When all processing is complete, emitter blades are separated from the rest of the wafer by manually breaking the tethers with a pair of tweezers. An example of an emitter array fabricated this way is shown in Figure 4-8.

4.3 Second-generation Devices

4.3.1 Surface Microstructures

Design Considerations

Characterization of the first-generation devices revealed several important deficiencies. One major issue was that wicking structures on the scale first designed were too small to ensure sufficient flow of the viscous polymer solutions tested. A thorough re-examination of the work by Xiao et al. [40] made it clear that, although the non-dimensional spreading parameter was maximized by maximizing the height-to-pitch ratio ($\frac{h}{p_M}$) at the optimum width-to-pitch ratio ($\frac{d}{p_M}$), this did not necessarily maximize the flow rate within the design constraints. Since the spreading parameter is non-dimensionalized via division by the pitch p_M, increasing p_M at constant $\frac{d}{p_M}$ and constant h will increase the flow rate despite decreasing $\frac{h}{p_M}$. This scaling would not necessarily hold true as p_M approaches the capillary length, at which point gravitational effects must be taken into account. The realization that the maximum achievable flow rates within the design constraints existed at scales where gravity is significant inspired a re-working of the Xiao analysis to include gravity. It became evident that other geometries, such as trench-like microchannels, should enable even higher flow rates due to higher capillary pressure at high porosity or, equivalently, high permeability. The extension of this line of reasoning further leads to an enclosed cylindrical geometry, which offers an even higher ratio of surface tension force to viscous resistance; however, the flow in this case would no longer be an open, external flow and thus would be more susceptible to clogging and pressure non-uniformity that can occur in closed channels.

As was explained in Chapter 3, maximum flow rate occurs not necessarily when p_M reaches the capillary length λ but when $w = p_M - d$ is roughly the same order of magnitude as h. Once w becomes several times h the natural curvature of the liquid meniscus will intersect the bottom surface of the wicking structure, at which point previous assumptions no longer hold and capillary rise, if any occurs, is in the corners. In this second-generation design, both micropillar and microchannel geometries were included. Dimensions were selected to reveal the suspected flow rate maxima as well as allow a direct comparison of pillar and channel wicking rates (Table 4.3). In order to facilitate a direct comparison, square-packed pillars with square cross-section were chosen. Both nominal and measured dimensions of the samples made are included in Table 4.3.

Sample #	p_M [μm]	d [μm]	d_{act} [μm]	Sample #	p_M [μm]	d [μm]	d_{act} [μm]
1P	125	30	Lost	1T	125	30	Lost
2P	125	42.5	Lost	2T	125	42.5	26.3
3P	125	67.5	45.3	3T	125	67.5	55
4P	250	30	Lost	4T	250	30	Lost
5P	250	67.5	37.2	5T	250	67.5	46.8
6P	250	117.5	66.5	6T	250	117.5	73.2
7P	250	167.5	93.1	7T	250	167.5	100.6
8P	500	30	Lost	8T	500	30	Lost
9P	500	67.5	Lost	9T	500	67.5	44
10P	500	167.5	144.4	10T	500	167.5	146.7
11P	500	230	211.1	11T	500	230	211.5
12P	500	305	288.9	12T	500	305	288.5

Table 4.3: Design space of second-generation wicking structures: Ranges for the microstructure width d and pitch p_M are selected to explore flow rates around expected optima for both pillars ($\#P$) and trenches ($\#T$). Fabrication errors resulted in the loss of some samples and a shifting of the design space; the actual fabricated dimensions are included in the table with the designed dimensions.

Fabrication Process

The selection of new microstructure dimensions brought with it new fabrication challenges. The first issue was the scaling up of the etch window (i.e., the microchannel width or the gap between adjacent pillars). With an increase in this dimension comes an increased risk of undercutting the wicking structures and tapering the sidewalls of the cut. Another source of concern were the two commonly known DRIE phenomena referred to as microloading and ARDE (aspect ratio-dependent etching); the first describes the fact that etch rate locally depends on the proportion of etching area to total area, while the second describes the tendency of etch rate to decrease as the aspect ratio (i.e., $\frac{\text{etch depth}}{\text{etch window}} = \frac{h}{w}$) increases. The net effect of these phenomena is that it is very difficult to etch a large variety of feature sizes on the same wafer and achieve uniform results. In an attempt to combat these effects and allow for the entire design space to be explored on a single wafer, a new process was proposed.

The concept was to pattern identical, smaller scale pillars uniformly throughout the desired etch windows. These small pillars would etch uniformly to some desired depth at which point they could be sacrificed with an specially tuned undercutting etch. This would leave behind the intended wicking features that span a wide range of dimensions without the large variations in height and sidewall angle that might be expected in direct etching in the absence of the sacrificial pillars. An additional benefit of this process is the introduction of higher surface roughness at the bottom of the wicking structures where the sacrificial pillars originally connected to the substrate. This should increase the driving capillary pressure, and, as a result, further increase the flow rate (Figure 4-9).

In practice, this process did not work as planned. The sacrificial undercutting etch was difficult to tune for the desired chopping effect. An unoptimized etch was used that eliminated the sacrificial pillars at the cost of also altering the intended dimensions. The characteristics of this etch and its effects on one pillar geometry are shown in Figure 4-10.

When this process was applied to all of the wicking geometries, those with the

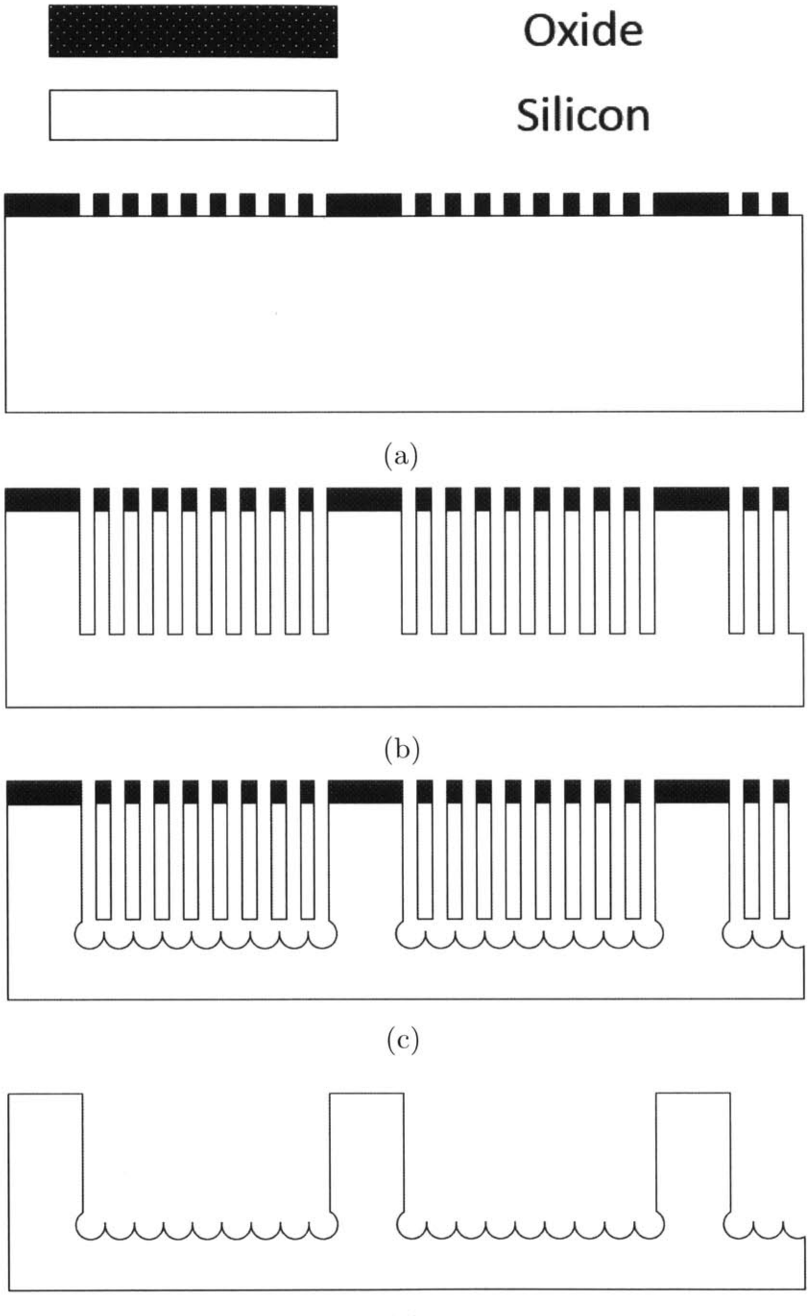

Figure 4-9: Process flow for sacrificial etch: (a) Pattern non-uniform features into oxide mask (b) DRIE all features to desired depth (c) Perform tuned SF_6 etch to sacrifice narrow pillars and leave behind intended features (d) Etch away oxide mask.

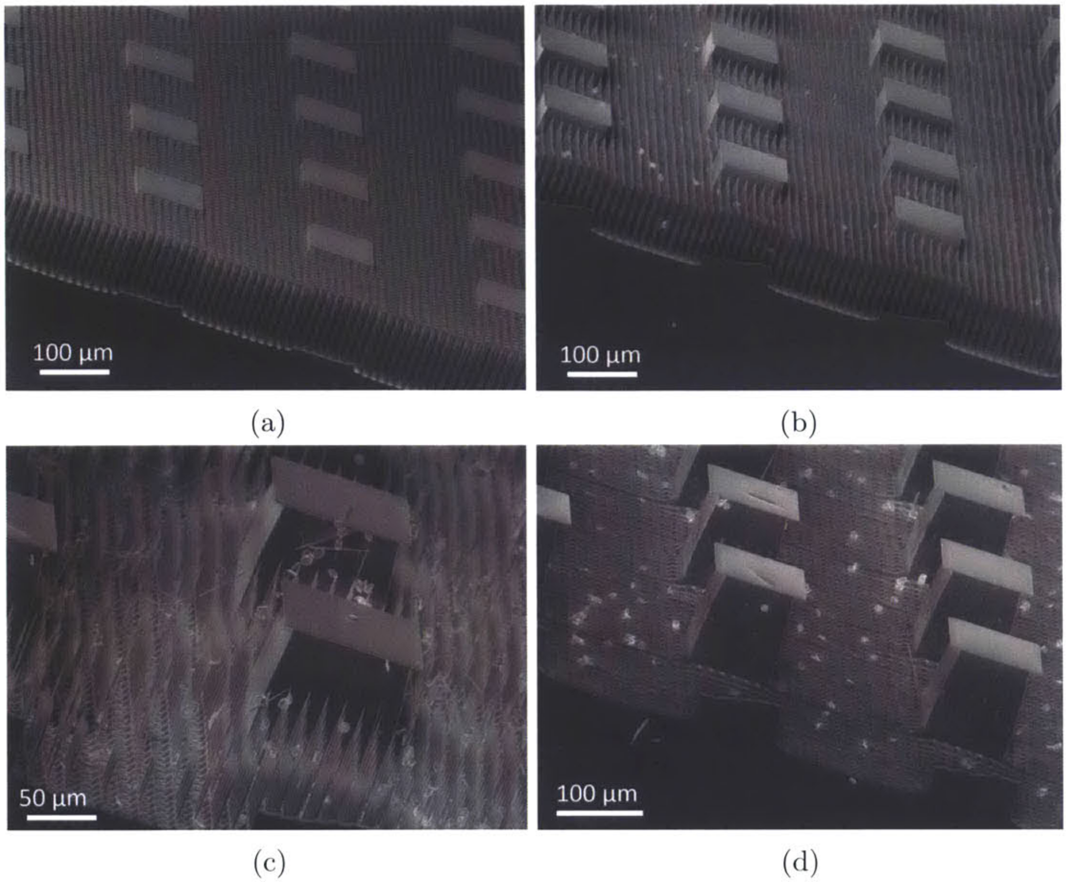

(a) (b) (c) (d)

Figure 4-10: Characterization of sacrificial etch: (a) Non-uniform microfeatures are etched to the desired depth. (b) Sacrificial step is not sufficiently selective and begins etching pillars from the top and sides rather than the bottom. (c) Further etching drastically thins the pillars from all directions. (d) The narrow pillars are finally sacrificed after significant lateral etching has damaged the intended features. The bottom surface is roughened by chopping of the narrow pillars. The "hats" on the wide pillars are oxide masks that disappear after processing.

narrowest feature size d (either pillar width or microchannel wall thickness) were chopped off in addition to the sacrificial pillars. This left behind unintended pyramid or ridge-like structures on the order of 10 μm tall. These unintended structures were capable of wicking liquids; however, the combination of lower capillary pressure and reduced film thickness meant a significant reduction in flow rate. The wicking structures that avoided undercutting were demonstrated to successfully transport several different working liquids at flow rates of interest to electro-hydrodynamic jetting.

4.3.2 Emitter Arrays

Design Considerations

The results of the first round of electrospinning experiments informed the development of the second generation design. Since short emitters previously proved ineffective, all emitters were made 6 mm tall. The new design space included three different emitter spacings (1, 2, and 3 mm), two tip radii (125 and 250 μm), and four wicking structures (2P, 6P, 1T, 4T) - two for each tip radius size. Second-generation emitters were fabricated on three-sectioned 3 cm blades that could be cleaved into smaller 2 cm or 1 cm sections if desired. This helped optimized the use of wafer space in fabrication.

Fabrication Process

The fabrication of the second-generation emitter blades with two-sided roughness begins with a 500 μm thick, n-type single-crystal silicon wafer that is double side polished and coated with 0.5 μm of thermal oxide. Assuming 150:1 selectivity of thermal oxide to silicon, the starting oxide layer provides a sufficient mask to etch features roughly 75 μm deep. In order to allow for deeper features and build in an extra factor of safety, additional oxide was deposited. This first requires a standard RCA clean of the wafer. Following the clean, 1 μm of oxide is deposited on the surface via PECVD, and the wafer is annealed for one hour in nitrogen at 950 $^\circ C$. This densifies the oxide layer and improves its etch selectivity.

Patterning of the oxide layer via photolithography entails similar steps as those previously described, except the steps are now performed on both sides of the wafer. They are: HMDS deposition, top-side spin-coating of 1 μm OCG 825, 15 minute pre-bake at 90 $^\circ C$, back-side spin-coating of 1 μm OCG 825, 30 minute pre-bake at 90 $^\circ C$, top-side exposure, back-side exposure, development in OCG 934, spin rinsing, and 30 minute post-bake at 120 $^\circ C$. A new step at this point is RIE of the oxide layer on both sides of the wafer with the AME 5000. This transfers the micropillar pattern from the thin photoresist into the oxide. Once this is complete, the photoresist is removed via ashing in oxygen plasma, and the wafer is ready for more photolithography (Figure 4-11).

The second round of photolithography transfers the emitter blade outline into the thick resist with the same series of steps performed on the first-generation emitters. The outline is then cleared of oxide with a reactive ion etch, which clears the way for the DRIE through-etch of the silicon. But, first, the wafer is flipped over and the back-side microfeatures are etched with DRIE. An SF_6 etch is then performed to sacrifice the narrow pillars, leaving the intended features behind. After this, the silicon wafer is mounted top-side up onto a quartz wafer using photoresist. Following the mounting step, the emitter blade outlines are etched with DRIE from the top-side to a depth between 75% and 90% of the total wafer thickness depending on the desired final micropillar depth. The silicon wafer is then released from the quartz wafer via soaking in an acetone, which dissolves the photoresist. The released silicon wafer is ashed in oxygen plasma and then piranha-cleaned to remove DRIE polymers and photoresist.

The silicon wafer must be mounted on a quartz wafer, once more, for the final DRIE etch. This etch is performed from the top-side of the wafer using the patterned oxide layer as a mask. It simultaneously etches the top-side microfeatures and completes the remaining 10-25% of the through-etch. Then, another SF_6 etch is used to sacrifice the narrow pillars, leaving the intended features behind. When it is complete, the silicon wafer must again be released from the quartz wafer with acetone soaking. When all processing is complete, emitter blades are separated from the rest of the wafer by manually breaking the tethers with a pair of tweezers.

Fabrication of the second-generation wicking structures on the emitters suffered from similar deficiencies to fabrication off the emitters. It was likely exacerbated by two particular aspects of the integrated emitter fabrication. First, the four wicking structures chosen for incorporation into the emitters were those with the highest expected flow rates per unit width. These were the designs with smaller feature size d, which also happened to be the designs most likely to suffer from undercutting. Second, the relatively large etch window surrounding the emitter profile ($\approx 80\ \mu m$) likely

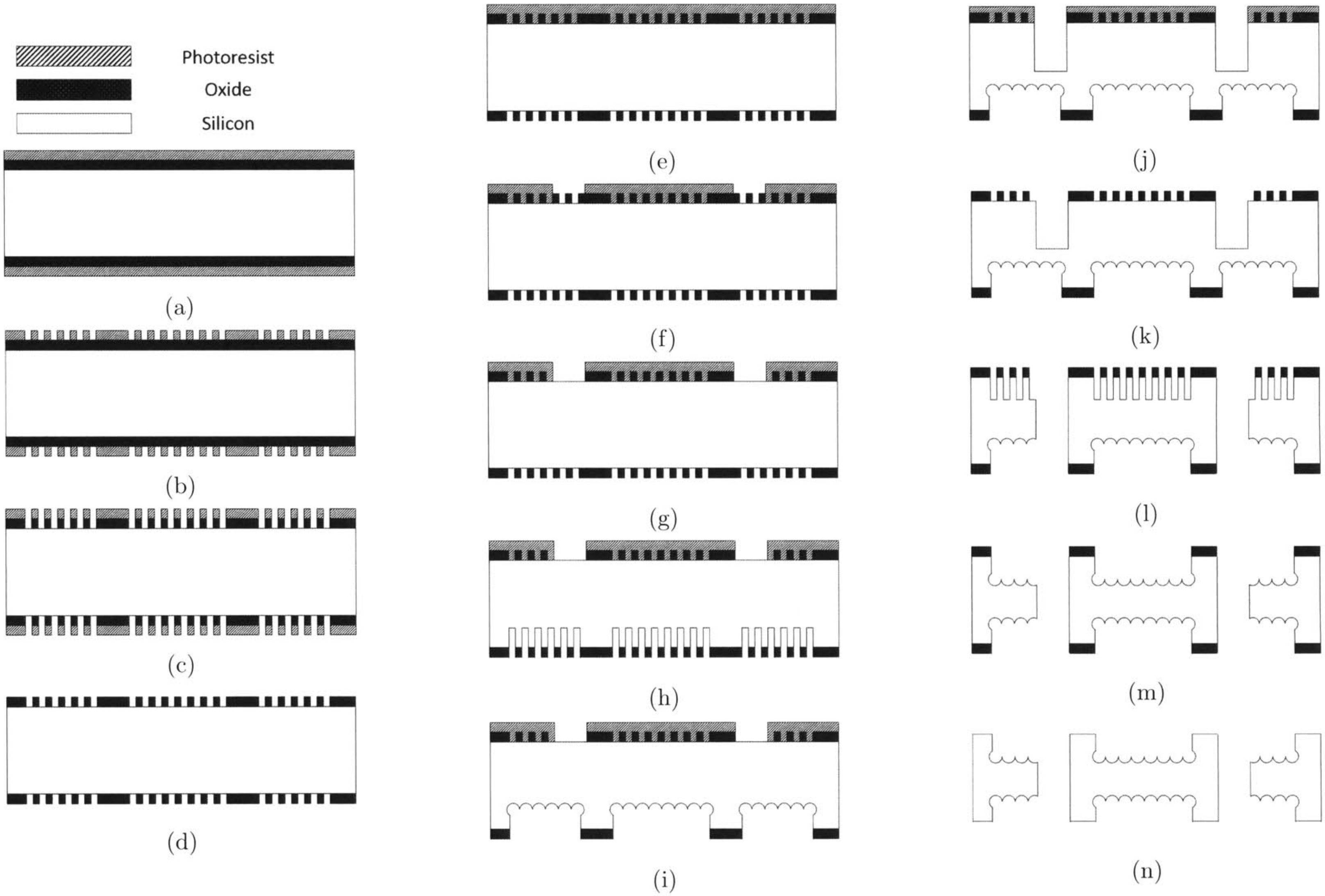

Figure 4-11: First-generation emitter blade process flow: (a) Deposit and anneal oxide, then spin-coat with photoresist (b) Expose and develop microfeatures in photoresist (c) RIE microfeatures into nested oxide mask (d) Remove photoresist in oxygen plasma (e) Spin-coat thick resist on top-side (f) Expose and develop emitter blade outline in thick resist (g) RIE to clear oxide from blade outline etch window (h) DRIE of back-side microfeatures to desired depth (i) Tuned SF_6 etch to chop back-side sacrificial pillars (j) DRIE of emitter blade profile from top-side to partial depth (k) Oxygen plasma and piranha clean to remove thick resist (l) Simultaneous DRIE of top-side microfeatures and remaining depth of emitter profile using nested oxide mask (m) Tuned SF_6 etch to chop top-side sacrificial pillars (n) Etch away oxide mask and break tethers to remove emitter blades.

enhanced the undercutting of structures near the emitter edge during the sacrificial SF_6 etch. As a result, only one of the four wicking geometries survived the emitter fabrication without being chopped off. The surviving geometry was a pillar structure that was expected to be far less effective at wicking than the channel structure of corresponding size; it was included primarily for the purpose of comparison (Figure 4-12). This unfortunate flaw in the fabrication process meant it was unlikely these emitters would be capable of continuous electrospinning, although they could still be tested using the coating procedure employed for the first-generation emitters. This will be discussed further with other experimental results in the subsequent chapters.

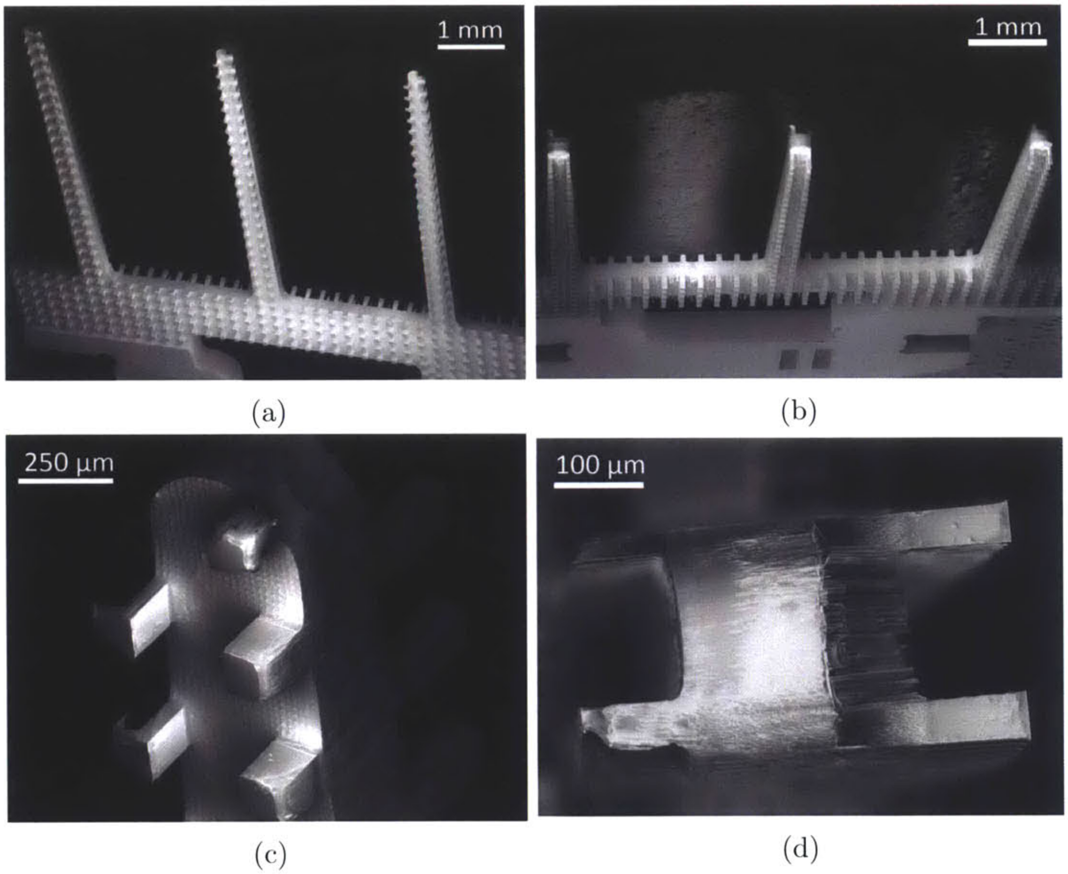

(a) (b) (c) (d)

Figure 4-12: Fabricated second-generation emitter with pillars: The only wicking geometry to survive the integrated fabrication on emitter arrays is shown in the pictures above.

Chapter 5

Wetting Behavior of Microstructured Surfaces

5.1 Characterization of First-Generation Surface Features

Before testing the first-generation emitter arrays, it was of interest to characterize the designed microstructured surfaces independently. A simple yet informative technique for doing this is depositing a droplet of liquid on the surface. Much can be deduced from observations of the shape, static contact angle, or spreading rate of the droplet. These tests can be used to confirm theoretical predictions for liquid propagation rates through micropillars and help guide the selection of optimal material coatings and geometries.

In order to make direct comparisons with modeling predictions, it is necessary to first know the surface tension of the working liquid and its inherent contact angle on a given surface chemistry. This inherent angle is the Young's angle discussed previously; it is a result of competing surface energies and is independent of roughness or geometrical features. In practice, most surfaces have some non-ideality so an exact measurement of Young's angle is difficult. This was confirmed by contact angle measurements of water on the following surfaces: silicon (with native oxide), thermally grown SiO_2, LPCVD SiN, and LPCVD SiC. These surfaces were nominally flat. Average contact angles on the fresh films are shown in Figure 5-1.

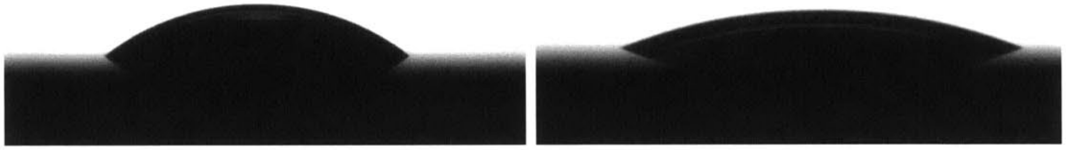

(a) Silicon (w/ native oxide): 45°

(b) Silicon Dioxide: 29°

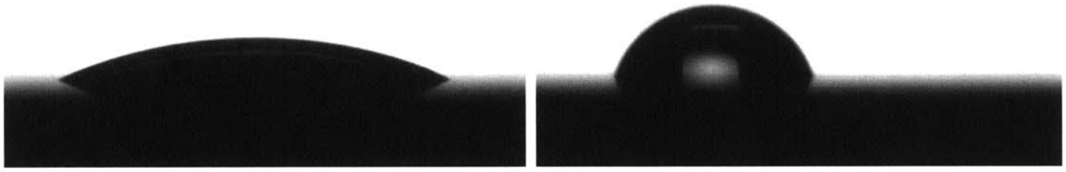

(c) Silicon Nitride: 28°

(d) Silicon Carbide: 78°

Figure 5-1: Contact angles of water on different surfaces: A range of intrinsic wettability is observed.

These measured values could vary by ±5° at different locations on the wafer. Rigorous cleaning procedures can provide more reliable measurements but cleanliness degrades over time. It is best to develop a standardized cleaning treatment and perform it prior to any testing.

For maximizing the spreading rate of a viscous electrospinning solution, it is sensible to use tall micropillars with near-optimal porosity that have been coated with an intrinsically hydrophilic surface, such as SiO_2. Exposure of the surface to oxygen plasma prior to testing will make it even more wetting, reducing the contact angle to near 0°. Using the best possible case, given the fabricated first-generation microstructures, it was not possible to induce noticeable spreading of a droplet of 4%

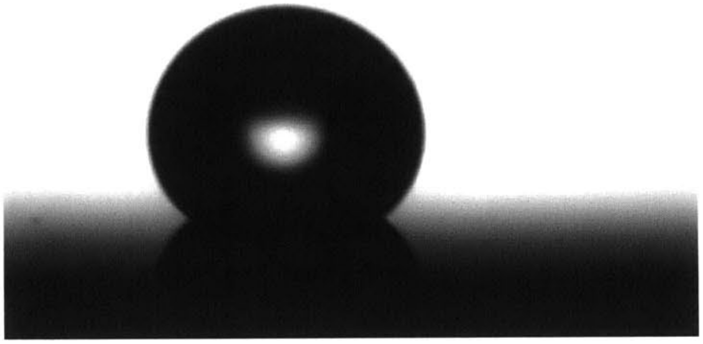

Figure 5-2: Superhydrophobic water droplet on SiC coated micropillars: Interfaces with Young's angles under 90° can be coerced into a metastable Cassie-Baxter state with a large enough energy barrier, which in this case is provided by the 63 μm tall, sharp-edged micropillars coated with SiC. The water droplet shown has a contact angle of 136°.

polyethylene oxide in 40/60 water/ethanol. It became evident that pillars on the scale of those fabricated were not well suited for transport of viscous liquids. Revisiting the relevant theory suggested increasing flow cross-section was the best way to increase flow rate. This inspired the second-generation wicking structures previously discussed whose characterization is discussed in section 5.2.2. Although the original micropillar structures proved incapable of spreading highly viscous liquids, it was still possible to characterize them using water.

5.1.1 Demonstration of Different Wetting States

For the range of micropillar geometries fabricated, several different wetting states could be induced with the use of various surface coatings. Silicon carbide was the most hydrophobic coating explored with an intrinsic contact angle of 78°. Using SiC-coated pillars, it was possible to coerce water droplets into a state of superhydrophobicity. According to equation 3.7, a droplet must already have a Young's angle above 90° to favor the Cassie-Baxter state. However, lower contact angle interfaces can be held in a metastable Cassie-Baxter state if there is a large enough energy barrier blocking

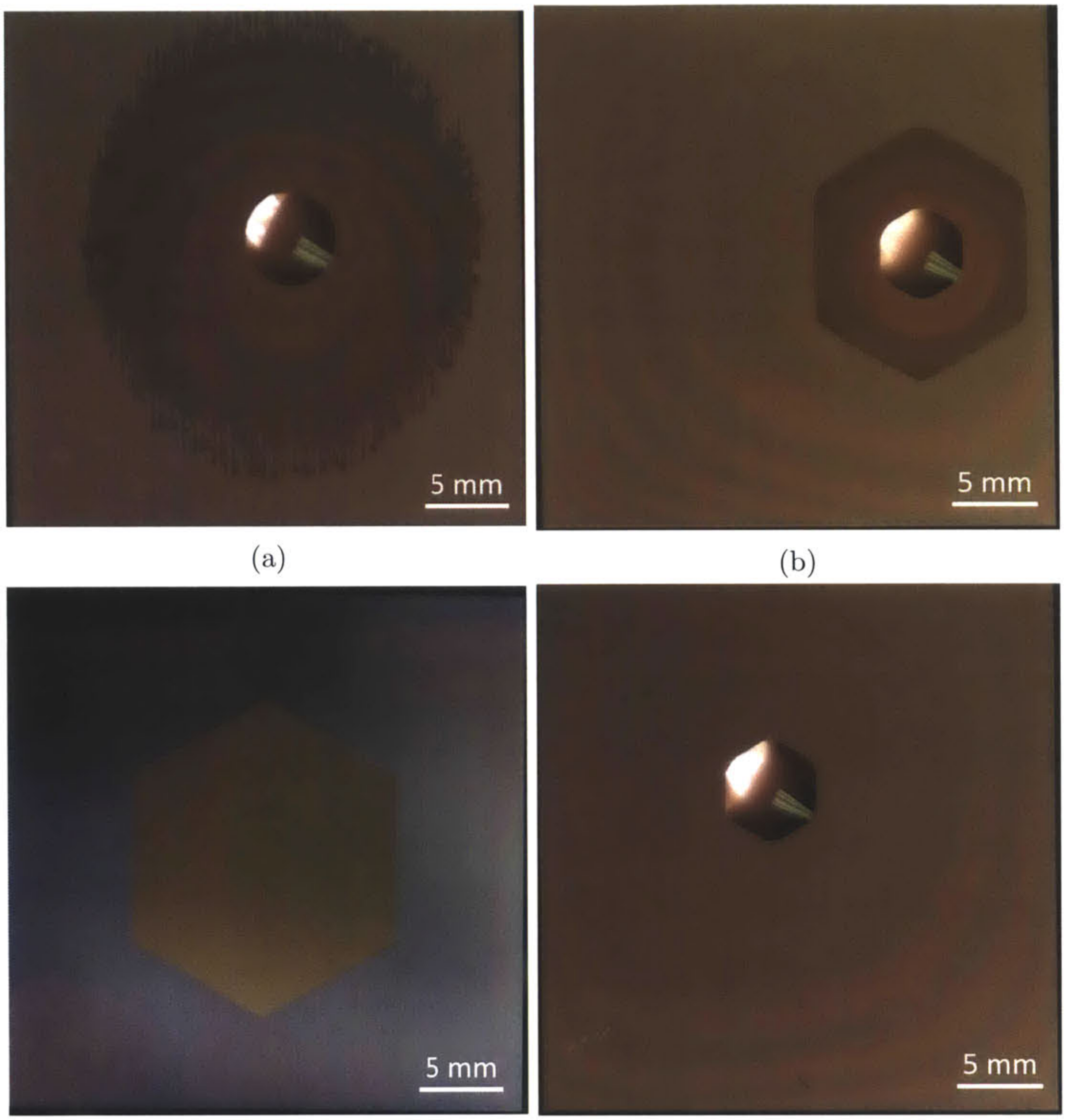

(a) (b)

(c) (d)

Figure 5-3: Hemi-wicking of water droplets through porous micropillar forests: (a) 10 μm tall pillars coated in polysilicon (Porosity = ϵ = 0.31) exhibit fractal-like spreading due to the bifurcating behavior of the flow at each hexagonal junction. (b) 10 μm tall pillars coated in polysilicon ($\epsilon = 0.64$) spread water with a hexagon-shaped front. (c) 63 μm tall pillars coated with oxide ($\epsilon = 0.64$) show hexagonally-shaped spreading. Due to their greater porosity and hydrophilicity, these surfaces fully imbibe the droplet of water in less than 0.5 seconds. (d) 10 μm tall pillars coated in polysilicon ($\epsilon = 0.75$) do not spread the droplet, since the critical contact angle is lower than Young's angle. The Wenzel state is energetically favorable.

the transition to the lower energy Wenzel state [34]. Figure 5-2 shows a water droplet in such a metastable state with a contact angle of 136°.

The most common droplet behavior in our micropillar forests was hemi-wicking. This is due to the fact that even moderate increases in surface roughness greatly increase the critical contact angle ($\theta_{HW,crit} = \cos^{-1}[\frac{1-\phi_s}{r-\phi_s}]$) below which hemi-wicking occurs. In fact, only one sample, aside from those coated with SiC, failed to exhibit hemi-wicking. This sample was coated in polysilicon ($\theta_Y \approx 65°$) but had a critical contact angle of 61.3° ($d = 15\ \mu m$, $p = 30\ \mu m$, $h = 10\ \mu m$). All other samples had greater roughness and, therefore, larger critical contact angles due to either taller or denser micropillar forests. These other samples exhibited different varieties of hemi-wicking. Shallower pillars enable the coexistence of a droplet and spreading film while taller pillars imbibe the entire droplet. Denser pillars spread liquid in a fractal-like pattern as a result of bifurcation at narrow hexagonal juntions; sparser pillars spread liquid in the shape of a hexagon (Figure 5-3).

5.2 Characterization of Second-Generation Surface Features

The previously described characterization of first-generation wicking features was helpful in providing an intuitive understanding of liquid behavior on microstructured surfaces. It inspired the design of larger-scale second-generation wicking features capable of delivering higher flow rate per unit area. Consideration of capillary flow optimization in larger geometries prompted the incorporation of gravitational effects into the analysis, which was an important theoretical development and influenced the procedure for testing the new structures.

5.2.1 Experimental Method

Polyethylene oxide (PEO, molecular weight M = 6×10^5) purchased from Sigma Aldrich was used to prepare solutions in ethanol/water mixtures. Due to its lower solubility in ethanol, PEO was first dissolved in deionized water alone at concentrations as high as 6% w/v. The solutions were heated to 50 $^{\circ}C$ on a hot plate and kept at this temperature for several days. Vigorous shaking was applied intermittently until the solutions appeared uniform in consistency. At this point, solutions were diluted to lower concentrations using various amounts of water and ethanol to achieve desired solvent ratios. After dilution they were, again, shaken vigorously and allowed to sit overnight.

During the wicking tests, an open Pyrex dish on a hotplate was filled with the desired solution, which was maintained at 30 $^{\circ}C$ via a thermometer feedback loop to ensure consistent viscosity. The test sample was exposed to a 200 W oxygen plasma for three minutes no more than 15 minutes before testing. Once cleaned, the sample was loaded with double-sided tape onto a plastic holder at the end of a stainless steel post. The post hung from a larger support structure and had the freedom to rotate so that it would rest vertically under the influence of gravity. The support structure was mounted on an adjustable stage, which allowed for it to be lowered until the hanging sample came into contact with the free-surface of the test liquid (Figure 5-4).

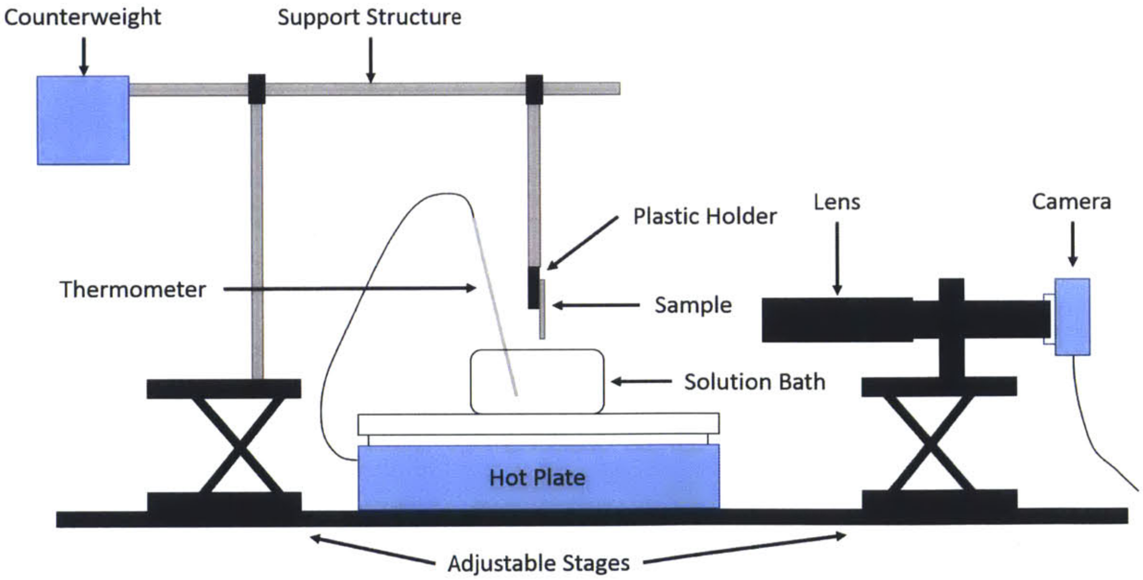

Figure 5-4: Schematic of the experimental setup for vertical capillary rise tests: This setup allowed for precise control over the liquid temperature and the orientation of the sample.

The rise of liquid through microstructures on the sample was recorded at frame rates between 40 and 50 fps using a Moticam 3.0 camera. Automated analysis of the videos to extract liquid rise height as a function of time proved difficult due to a number of factors including the presence of multiple moving liquid fronts, low contrast of the liquid and sample, and reflections of lighting sources on the sample. Instead, videos were analyzed by manually measuring position of the liquid front using a ruler fixed to a screen on which the videos were stepped in known frame intervals at 9x magnification. Uncertainty of approximately 0.5 mm in the ruler measurement corresponds to 56 μm uncertainty of the actual liquid position, which is an acceptable 0.3% of the 2 cm sample length.

5.2.2 Vertical Capillary Rise

Analysis of capillary rise against gravity in our second-generation wicking structures confirmed several important theoretical predictions. First, the model describing flow in open microchannels (model 1) was compared to the data from a range of microchannel geometries (Figure 5-5). The working liquid used was 1% PEO in 40/60 ethanol/water, since the inherent dynamics are slow enough to collect well-resolved data points but fast enough to limit the effects of evaporation. Viscosity and surface tension values were taken directly or extrapolated from literature as 0.03 $[Pa \cdot s]$ and 0.04 $\left[\frac{N}{m}\right]$ respectively [44]. Since all samples were treated with oxygen plasma shortly before testing, the contact angle should approach zero (i.e., the surfaces are rendered completely wetting). However, entering near-zero contact angles in the model generally yields an over prediction of the wicking rate. This has been observed in other work and was accounted for with a higher "effective" viscosity resulting from dynamic contact phenomena [45] or by assuming partial slip at the free-surface of the liquid [46]. Using a contact angle of 30° in our model yields fairly good agreement with data across several different samples and liquids. This agrees with dynamic contact angle predictions in other work [47] and provides a better average of curvature effects in meniscus correction factors. Since pressure varies linearly along the channel, $\cos\theta_{CA}$ should vary approximately linearly from 0 at the base to 1 at the liquid front (in the

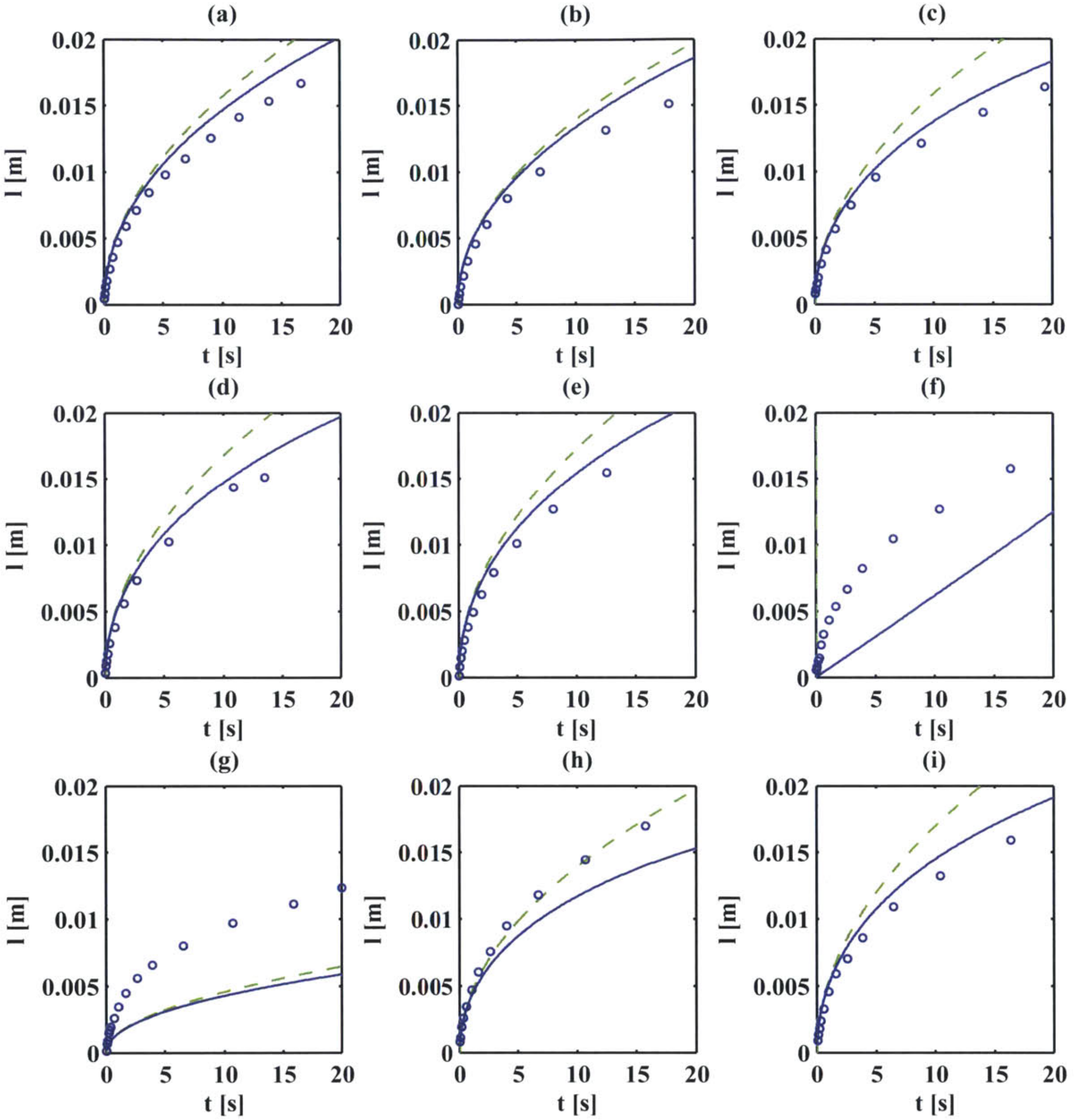

Figure 5-5: Height of rising liquid front vs. time for various open-microchannel geometries: The blue circles are measured data points; the solid, blue line shows the microchannel model including gravitational and meniscus effects (model 1); and the dashed, green line shows model predictions neglecting gravity (Washburn's equation from section 3.2.3). (a) T2 (b) T3 (c) T5 (d) T6 (e) T7 (f) T9 (g) T10 (h) T11 (i) T12. The working liquid is 1% PEO in 40/60 ethanol/water. Samples T9, T10, and T11 show poor agreement with our model, because they fall outside of the valid range $\frac{w}{h} < 2$.

perfectly wetting case). Therefore, on average, $\cos\theta_{CA} = 0.5$ which corresponds to a contact angle of 30°.

Our data and model 1 show good agreement for all samples in which $\frac{w}{h} < 2$. Beyond this limit, model 1 is not expected to accurately describe the data, because the meniscus will contact the channel bottom and capillary rise will occur primarily in the channel corners. Meniscus height vs. time data from samples within the limit $\frac{w}{h} < 2$ were fitted to equation 3.41 using the "*nlinfit*" function in MATLAB. The two extracted parameters were plugged into the derivative of equation 3.41 to estimate rise velocity, and this value was multiplied by average flow cross-section and divided by channel width to give the flow rate per unit length q. The experimentally derived values are plotted against theoretical predictions in Figure 5-6. Since microchannel height varied among the samples ($h \in [116, 139]\ \mu m$), theoretical predictions are

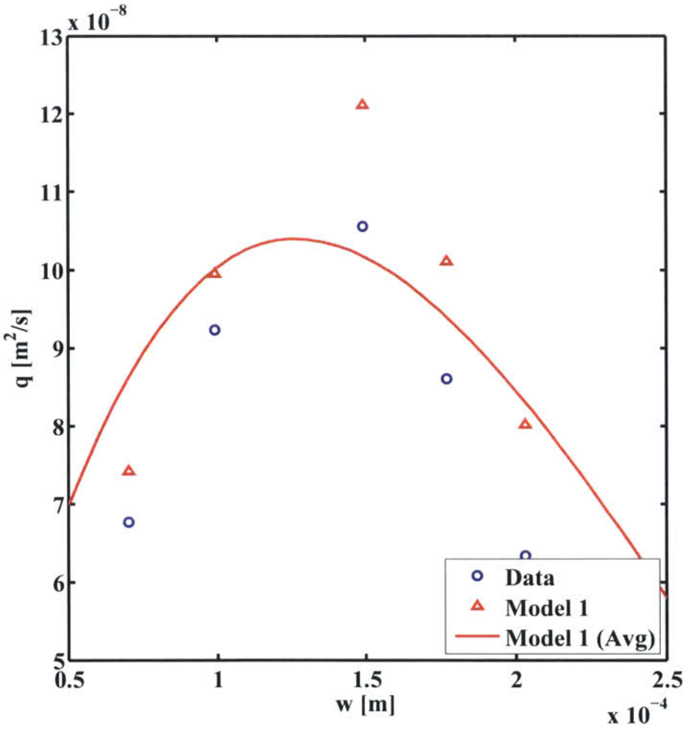

Figure 5-6: Flow rate per unit width q vs. microchannel width w (experiment and theory): The blue circles are measured data points, the red triangles are the corresponding theoretical predictions of model 1, and the red line shows the trend of model 1 using the average channel height of the tested samples. Both theory and experiment suggest a maximum flow rate per unit length exists for some channel width between 100 and 150 μm, which is on the order of the channel heights.

plotted in two ways. Predictions using the exact, measured channel heights are plotted as points (red triangles) against the exact channel widths, much like the experimental data. We also plot a curve (solid red line), calculated using the average channel height of 128 μm, to convey the trend with varying channel width. The predicted rise rates slightly overestimate the actual rise rates, but both theory and data suggest a flow maximum for a channel width somewhere between 100 and 150 μm, which is on the order of the channel heights fabricated.

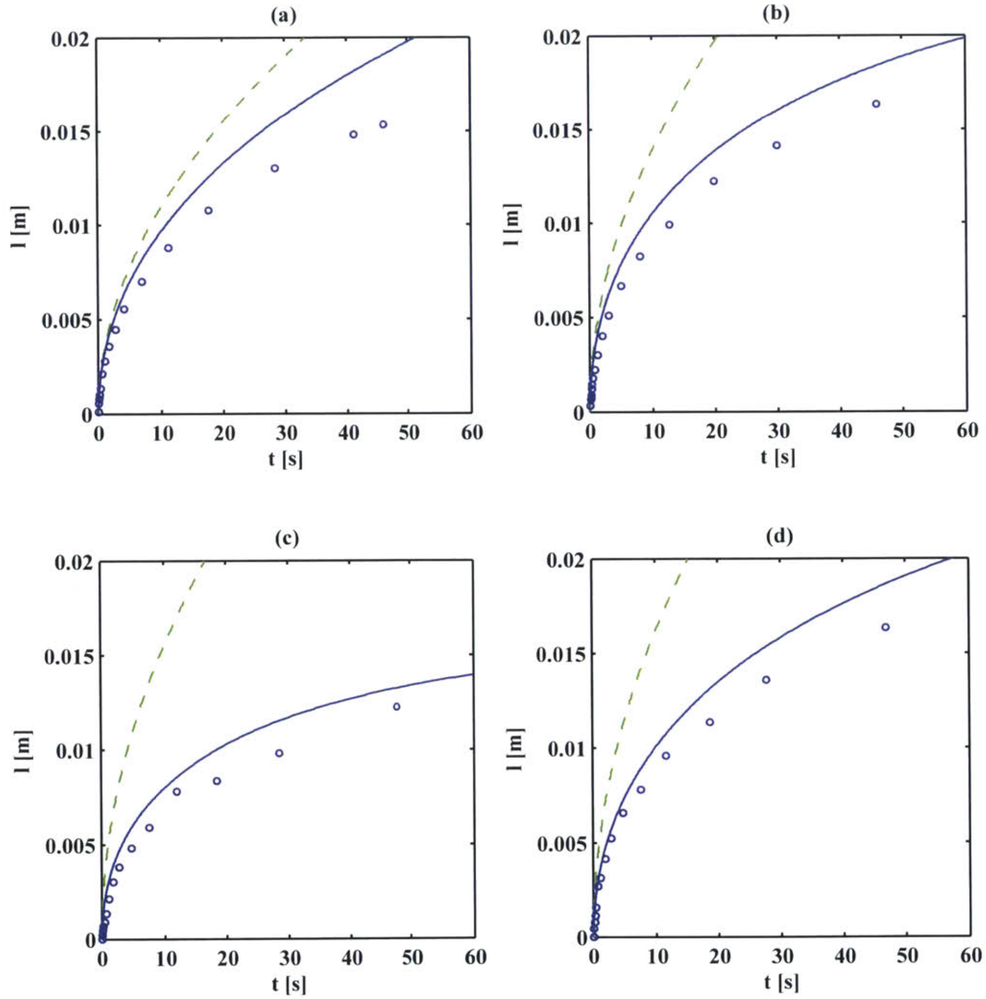

Figure 5-7: Height of rising liquid front vs. time for various micropillar geometries: The blue circles are measured data points; the solid, blue line shows the micropillar model including gravitational and meniscus effects (model 2); and the dashed, green line shows predictions of the model proposed by Xiao et al. in [40]. (a) P3 (b) P7 (c) P11 (d) P12. The working liquid is 1% PEO in 40/60 ethanol/water.

We also compare flow through several different micropillar geometries to our corresponding micropillar model (model 2). The working liquid used was again 1% PEO in 40/60 ethanol/water. As was the case with microchannels, our model (solid, blue line) shows good agreement with the data, although it slightly overestimates liquid rise rates (Figure 5-7). The model proposed by Xiao et al. (dashed, green line) is significantly less accurate, since it does not account for gravity or the decreased permeability associated with the meniscus cutting into the otherwise fastest portions of the velocity profile.

After confirming the validity of models 1 and 2 for a variety of geometries, we sought to directly compare the wicking merits of microchannels to micropillars. The fabrication errors previously discussed resulted in a shift of the intended microfeature dimensions such that there were no microchannels with a sidewall thickness equal

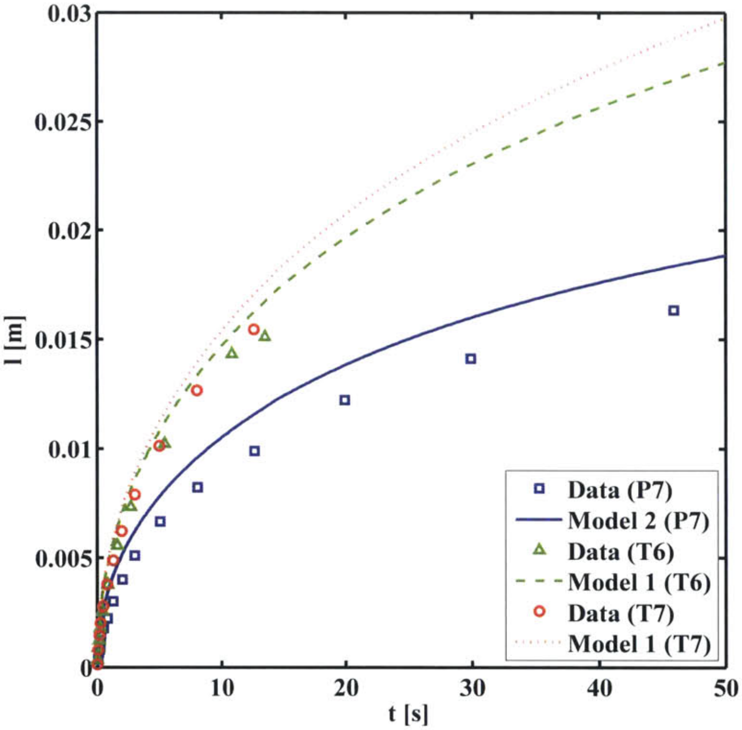

Figure 5-8: Height of rising liquid front vs. time compared in microchannel and micropillar geometries: Both microchannel samples (T6, T7) wick faster than the micropillar sample (P7) of approximately equal size. Calculations verify that Darcy velocity is also greater for the microchannels, which suggests they are the superior option for maximizing flow.

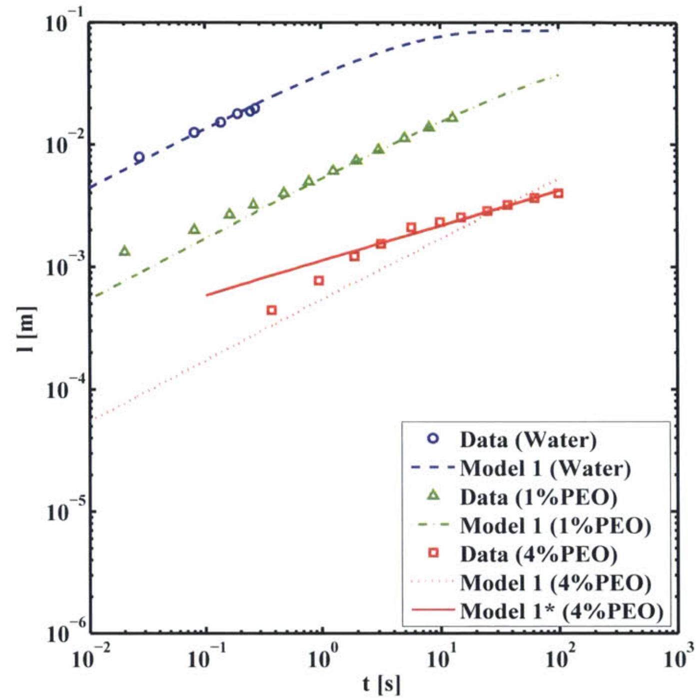

Figure 5-9: Height of rising liquid front vs. time compared for different viscosity liquids: Liquids with viscosities on three different orders of magnitude are tested in the same wicking structure (T7). Data and model 1 agree well for the two lower viscosity liquids, but the 4% PEO solution deviates due to non-Newtonian effects. Model 1* accounts for shear thinning with a power law and exhibits a better fit to the data.

to the side length of one of the micropillars. We decided to compare a particular micropillar sample (P7) to two different microchannel samples: one with d slightly larger than the pillars (T7) and the other with d slightly smaller (T6). If both microchannel samples performed better than the micropillars, it would suggest their superiority for wicking at equivalent sizes. This is, in fact, what was observed (Figure 5-8). The models slightly overestimate the wicking rate, as before. It should be noted that the plotted data indicates height of the moving liquid front as function of time, not flow rate per unit length. A sample with slower height rise than another can actually deliver higher flow rates if it is significantly more porous than its competitor. The data was fitted and flow rate per unit length q was calculated from the fitted rise velocity. At a height of 5 mm, the flow rates per unit length were as follows: $P7 : q = 8.45 \times 10^{-8}\left[\frac{m^2}{s}\right], T6 : q = 1.68 \times 10^{-7}\left[\frac{m^2}{s}\right], T7 : q = 1.66 \times 10^{-7}\left[\frac{m^2}{s}\right].$

Both microchannel samples deliver about twice as much liquid per unit length of surface as the micropillar sample of roughly equivalent dimensions.

Finally, we also examined the wicking abilities of one particular microstructure for several different liquids of varying viscosity. Microchannel sample T7 was tested in water, 1% PEO in 40/60 ethanol/water, and 4% PEO in 40/60 ethanol/water. The results are shown in figure 5-9. Model 1 fits the experimental data for water and 1% PEO quite well. The 4% PEO data does not match model 1 as well; at early times liquid rise is faster than predicted while at later times liquid rise is much slower than predicted. This is a result of non-Newtonian liquid behavior in the 4% PEO that is not accounted for in model 1. Fully describing the behavior of such a liquid requires accounting for polymer relaxation times, non-zero normal stresses, and viscosity that varies with strain rate. A relatively simple way to describe the last of these factors,

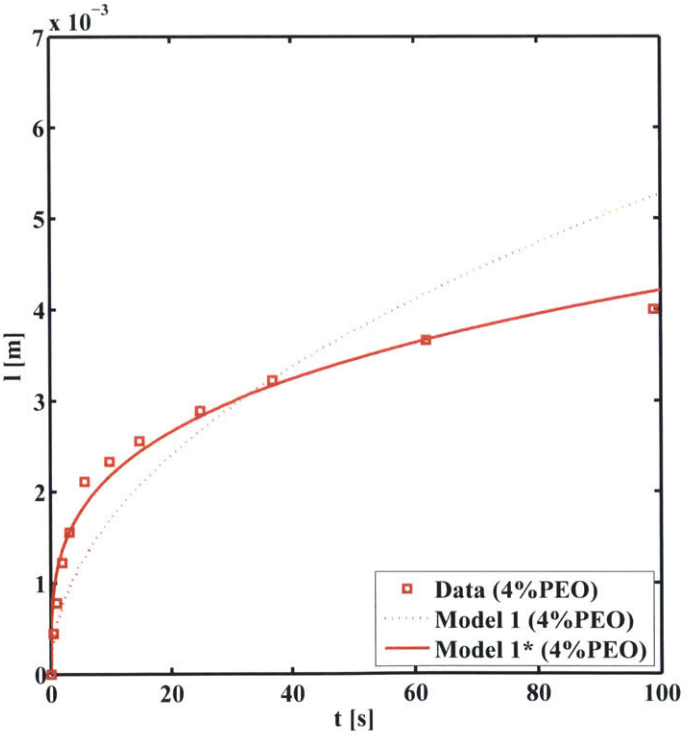

Figure 5-10: Height of rising liquid front vs. time compared for different viscosity liquids: The liquid rise height of the 4% PEO solution is shown at normal scale above. Treating the solution as a power law fluid (model 1^*) results in a much better fit of the shear-thinning behavior.

non-constant viscosity, is to model it with a power law (i.e., $\bar{\bar{\tau}} = \eta(\frac{\partial u}{\partial y})^n_p$ instead of $\bar{\bar{\tau}} = \mu(\frac{\partial u}{\partial y})$). Using parameters $\eta = 1.5 \times 10^7$ and $n_p = 0.4$ in model 1* provides a much better fit of the liquid's shear thinning behavior (Figure 5-9,Figure 5-10).

The rise velocity of the 4% PEO liquid front was approximated using finite differences. At a height of 2 mm, this velocity is 90 $\left[\frac{\mu m}{s}\right]$. Multiplying this by a channel height of 139 μm and a porosity of 0.6 gives the flow rate per unit length of surface as $7.46 \times 10^{-9}\left[\frac{m^2}{s}\right]$. If we take the low end of possible electrospinning flow rates to be $5.56 \times 10^{-11}\left[\frac{m^3}{s}\right]$, a 1 cm wide emitter is required. This suggests it would be wise to increase the channel height and width by an order of magnitude. Choosing these dimensions on the order of the capillary length will help achieve the global maximum flow rate that is possible in surface tension-driven flow.

Chapter 6

Electro-Hydrodynamic Jetting from Emitter Arrays

6.1 Experimental Procedure

6.1.1 First-Generation Devices

In order to test emitter arrays that were not capable of significant wicking, a procedure of pre-coating the emitters with the working liquid using a pipette was adopted. The idea of actively-coating some emitting surface prior to electrospinning has been demonstrated in the literature [48]. The PEO solutions used for electrospinning were of the same origin and produced using the same technique as described in the previous chapter.

The first experimental arrangement consisted of a 3-inch diameter plastic disc separated from an aluminum collector electrode of the same size with plastic spacers. This setup stood aluminum side up (i.e., electrospinning was performed against gravity). Aluminum foil was secured over the collector using conductive copper tape to allow for easy removal and imaging of different fiber spinning runs. High voltage was provided from a 30 kV DC power supply (Gamma High Voltage ES-30, 5W) to the aluminum disc via a cable terminated with an alligator clip. The emitter array being tested rested on spacers on the plastic base and was attached to a grounded wire with conductive tape. The array was coated with polymer solution using a pipette, and high voltage was applied by manually turning the analog dial on the power supply. Electrospinning was achieved for working distances under 3 cm, where the working distance (WD) is defined at the spacing between the emitter tips and the collector electrode. Our working distances were shorter than those typically used for electrospinning [27]. It was suspected that the arrays were exposed to smaller electric fields than a traditional single needle would experience at the same distance and voltage due to electrical shielding among neighboring emitters.

A number of arrays were fired as described, but their thin coat of polymer solution would deplete quickly, on the order of tens of seconds, and spinning would terminate. The micropillar structures that had been etched into one side of some emitter blades were potentially a help in this regard. Although the dynamics of flow through the pillars is too slow to enable continuous spinning, they are capable of storing a greater amount of liquid near the emitter tip as compared with flat surfaces due to their porosity. Their increased roughness also supports a thicker film on top of the entrenched layer than a smooth surface can support [49].

The desire to facilitate further experimentation and possibly increase run times prompted the fabrication of a new testing arrangement incorporating a plastic bath with a seat for the emitter array (Figure 6-1). The design allowed for the array to sit partially submerged in liquid, and it was thought that a combination of precoated emitters and a high bath level might lengthen run times. In such a setup, the electric field would have an easier time assisting the flow as it would not have to penetrate as deeply into the array, and the flow distance would be shorter. A slightly different electrode configuration was developed as well. Aluminum foil was taped onto a plastic block supported by a post mounted away from the bath (Figure 6-2), whereas, in the previous setup, spacers sat close to the array and were suspected of influencing the electric field detrimentally. The detachment of base and collector enabled active adjustment of the working distance mid-experiment by setting the bath on an adjustable stage. Originally, a grounded metal stage was used, but this seemed to inhibit spinning and was replaced with an electrically isolated stage. The

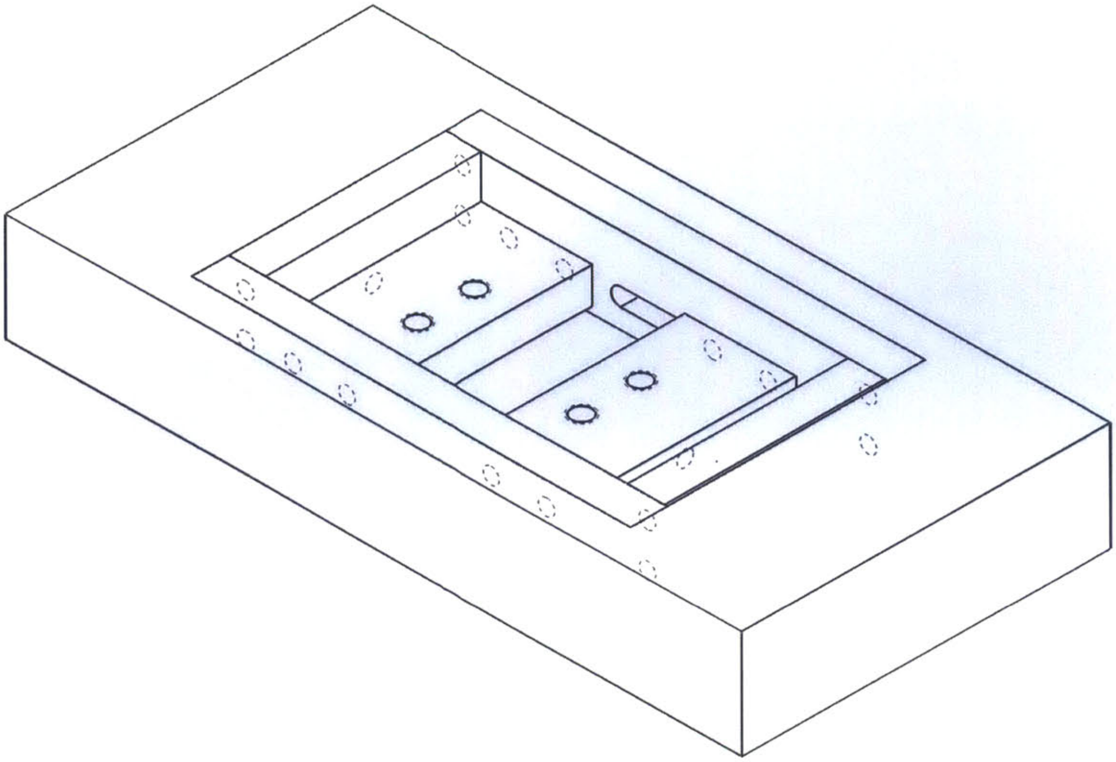

Figure 6-1: Plastic base to hold first-generation emitter arrays: This base allows the arrays to be operated while partially submerged in a bath of polymer solution.

results of experiments using this and the previous setup will be described later in this chapter.

6.1.2 Second-Generation Devices

For the second-generation experiments, a new testing apparatus was fabricated to standardize many operating parameters, improve repeatability, and interface with a new power supply. The Spellman High Voltage Bertan Series 225-50R supply is capable of delivering up to 50 kV DC high voltage and interfaces easily with Labview software, allowing the automation of voltage sweeps and current recording. For the new supply, a safer, more reliable means of making electrical contact with the emitters was desired. A Claymount CA3 connector and receptacle rated to 60 kV DC were chosen, and a part was designed to permanently house the high voltage receptacle. Four gold-coated, spring-loaded pogo pins were secured opposite the receptacle and

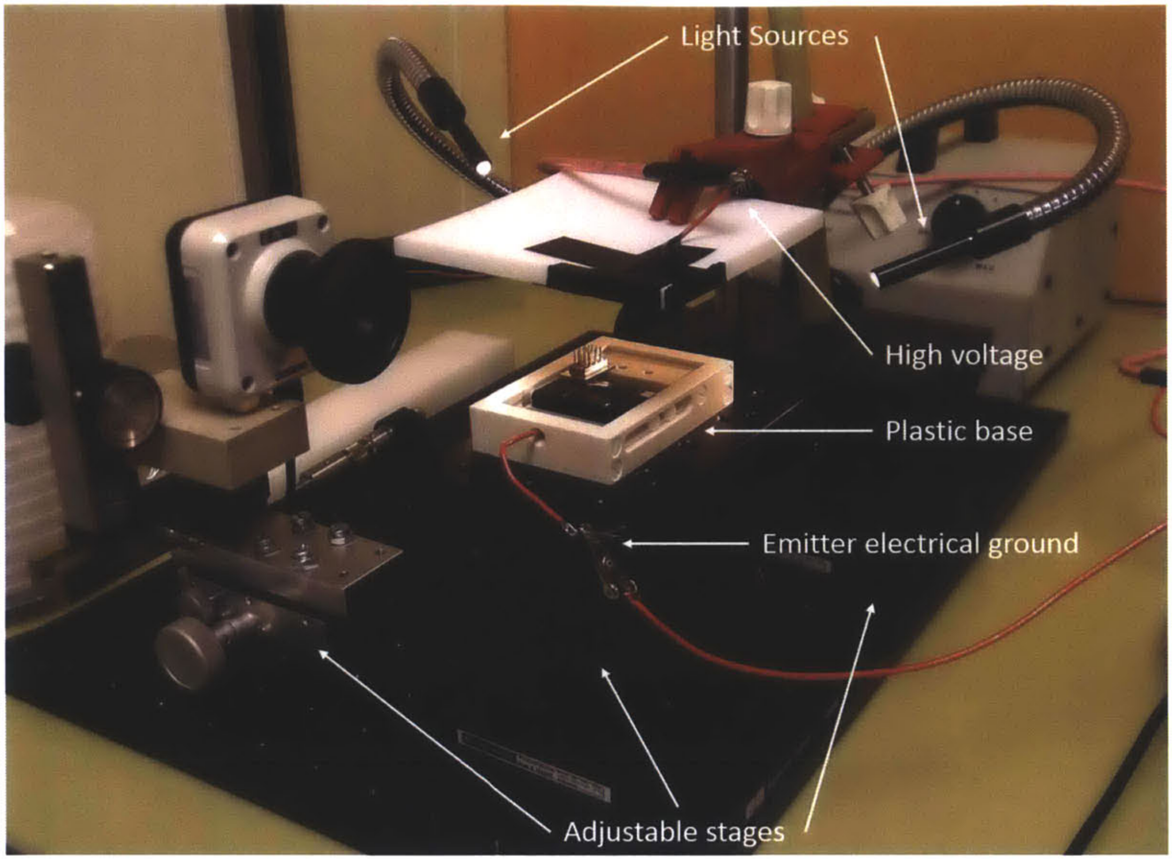

Figure 6-2: Modified, first-generation electrospinning testing rig: This experimental setup eliminates spacers between the emitter array and collector electrode, which can undesirably alter the electric field distribution. It also allows independent positional adjustment of the emitters and electrode.

soldered to its hot end. A carriage with a window supporting an aluminum electrode plate would slide over the housing until the backside of the electrode fully compressed the pogo pins. The carriage could then be held in place by inserting plastic pins into slots machined on either side of the carriage and receptacle housing (Figure 6-3). In the actual experiments, aluminum foil cut-outs were loaded into the carriage prior to the thicker aluminum plate; the plate provided rigidity to resist the spring-loaded electrical contacts but the fibers were collected on the foil. All parts aside from the collector, pogo pins, and high voltage receptacle were machined from high dielectric strength materials: either ultra-high molecular weight polyethylene (UHMWPE) or polyphenylene sulfide (PPS).

A new bath was fabricated, also from UHMWPE, that was capable of holding

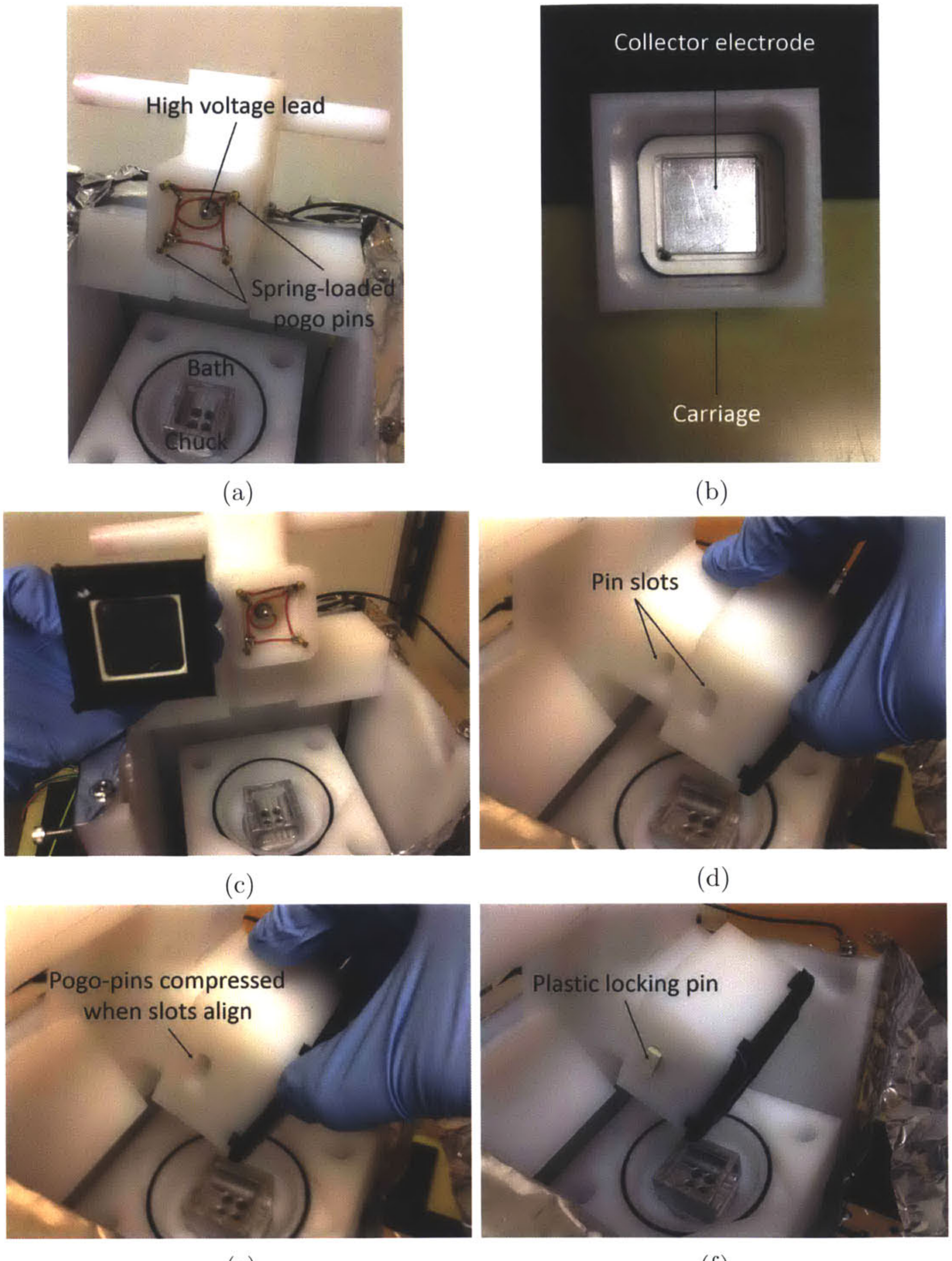

(a) (b) (c) (d) (e) (f)

Figure 6-3: Second-generation high voltage receptacle housing: (a) High-voltage receptable housing with spring-loaded pogo pins (b) Plastic carriage holding aluminum collector electrode (c)-(f) Steps to make electrical connection to the collector electrode.

the larger second-generation arrays. An aluminum chuck to support the emitter base was secured in the center of the bath on top of an aluminum plug. This plug was inserted into a hole at the bottom of the bath and properly sealed with an o-ring. Electrical connection to the array was made unobtrusively via the underside of the bath through the plug-chuck conductive pathway. Through holes were drilled in the four corners surrounding the bath to allow slide-mounting on four plastic columns screwed in an optical breadboard. This would fix x-y position, and annular plastic spacers fitting around each column allowed adjustment of z-position (Figure 6-4). A plastic lid was designed to cover and seal the top of the bath except for a cutout in its center where the emitter array was located.

Around the bath, a three-walled enclosure made of UHMWPE was constructed. Aluminum shim stock was secured on the outer side of the three exterior walls, and a detachable aluminum sheet would cover the open side during testing. A window was cut in the detachable sheet through which a camera could record the experiments. The receptacle housing was mounted above the bath in the following fashion: plastic rods were inserted through the housing on either side of the collector and then placed in notches on top of the enclosure in such a way that they bridged the two opposite walls and acted as support beams. The notches were positioned to maintain the relative planarity of the collector and emitter array. The back notch fixed its rod's translational position but allowed a rotational degree of freedom. The front rod was free to swing upwards with such a rotation, thereby moving the the receptacle housing away from the bath and allowing better access to the space, especially for swapping the foil collector (Figure 6-5).

A Labview script was written to semi-automate the testing process. Due to the nature of the experiments, continuous voltage sweeps did not make sense. The combination of short run times, transient effects, and a narrow operating range between turn-on and arcing suggested it was best to test at constant voltages. The influence of voltage could be ascertained by running multiple experiments, each at a different constant voltage. In any given experiment, the voltage was ramped from zero to the chosen value at a constant rate and then held at that value for a set amount of time

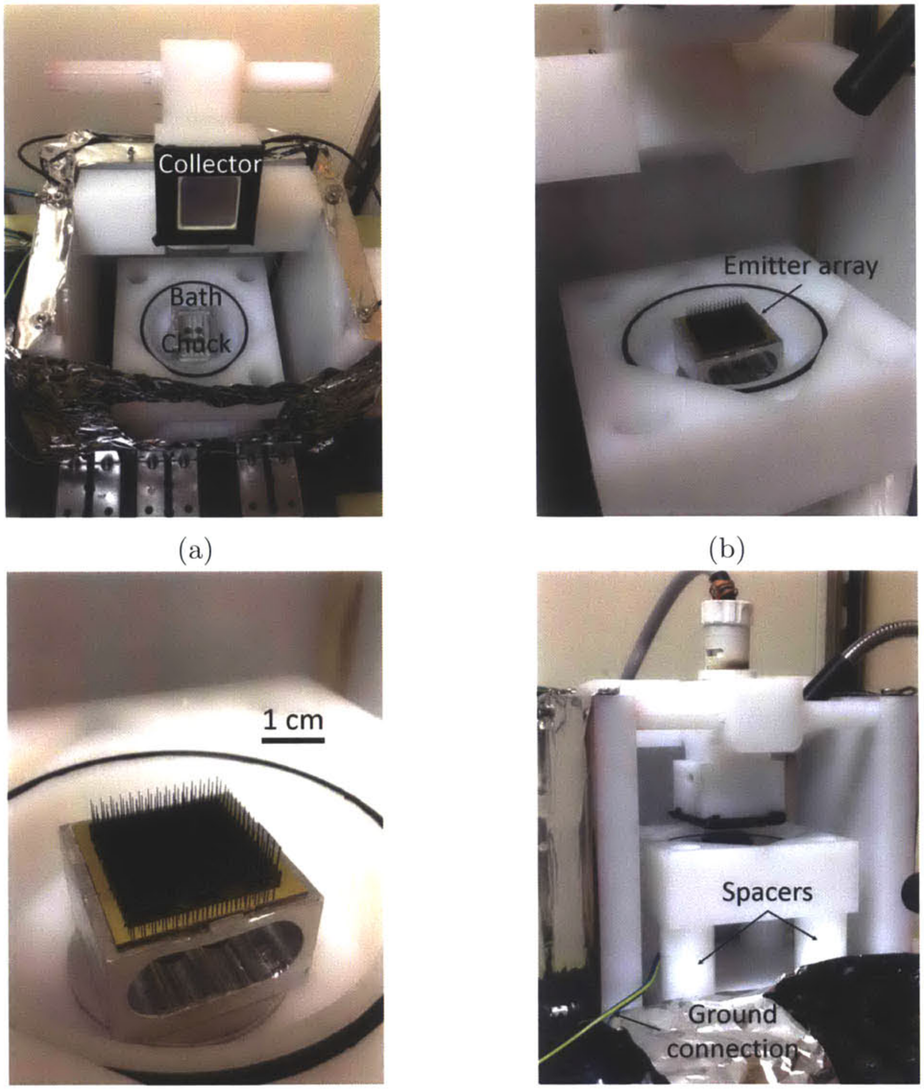

(a) (b) (c) (d)

Figure 6-4: Second-generation bath for emitter arrays: (a) Top-view of bath containing aluminum chuck for making electrical connection to the emitter arrays (b)/(c) 15×15 emitter array mounted on aluminum chuck (d) The height of the bath is adjusted with spacers; connection to ground is made underneath the bath to avoid interference with the emitter array.

before ramping back down to zero. The script recorded both the voltage and current traces at a sampling rate of roughly once every 700 ms. Testing revealed that faster sampling resulted in redundant readout values.

After running an experiment, the foil would be removed and placed overnight in a covered container in a nitrogen box so that any remaining solvent would evaporate.

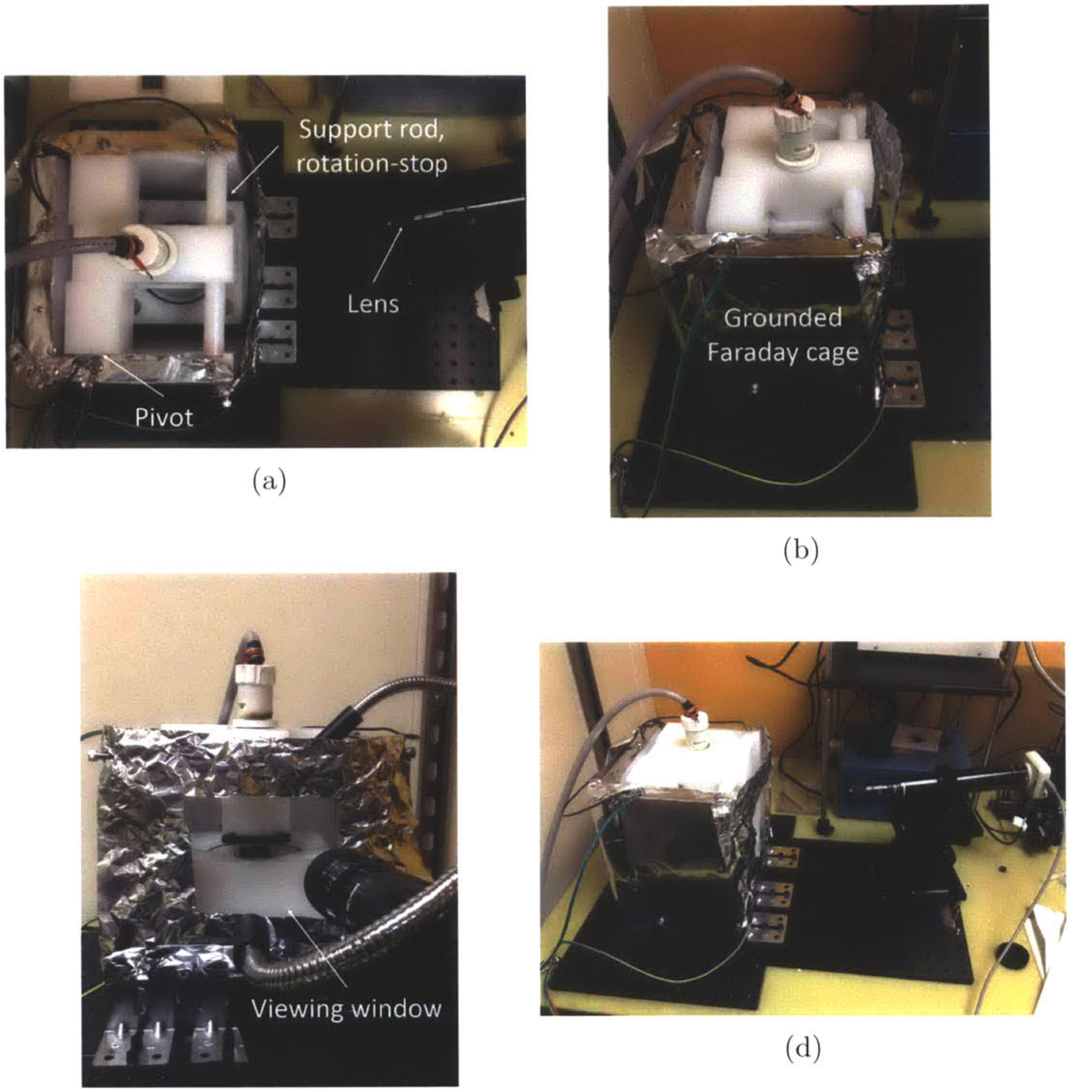

(a)

(b)

(c)

(d)

Figure 6-5: Second-generation testing apparatus: (a)-(d) Electrospinning experiments were performed in the enclosed plastic structure seen above. The exterior is electrically shielded by grounded shim stock. A high-zoom lens records testing at a large enough distance to avoid electrical interference.

The foil could then be weighed to ascertain the mass production rate of the process. This approach had severe limitations as the balance being used (Mettler Toledo AG204 Delta Range) was accurate to within ±0.1 mg. In most cases, a single run would deposit fibers whose mass could not be resolved. One way around this limitation is to perform several runs of spinning on the same foil. This approach generated detectable amounts of fiber but still suffered from low precision since the deposited mass was usually only slightly greater than the resolution of the scale. Nonetheless, this enabled order of magnitude estimates of the mass throughput. Following weighing, foils would be imaged in a scanning electron microscope to characterize the polymer deposits.

6.2 Characterization and Discussion

6.2.1 First-Generation Devices

During testing of the first-generation emitter arrays, we realized that the performance of the devices depended on a variety of experimental parameters. Electrospinning proved more difficult, and arcing between the collector and array more likely, if sufficient time passed between the coating of the array and the ramping of high voltage. One factor inhibiting the electrospinning could be increased surface tension and viscosity with the evaporation of solvent from the free liquid surface. Another likely cause is thinning of the coated layer due to gravity, which can expose sharp edges of the emitter geometry. When this occurred, corona discharge was sometimes observed near the emitter tip, and this always seemed to inhibit electrospinning (Figure 6-6).

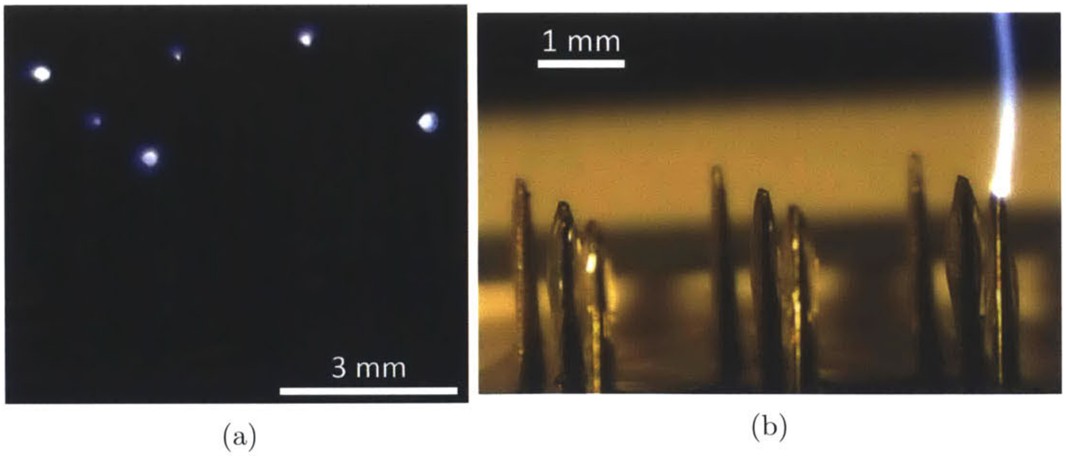

(a) (b)

Figure 6-6: Corona discharge and arcing from first-generation array: (a) Corona discharge was sometimes observed from the edge emitters of an array and always seemed to inhibit electrospinning. (b) Arcing between the collector and emitter array would sometimes occur preferentially over electrospinning, even when liquid was present at the tips.

It was also discovered that slower ramping of the voltage was less successful initiating a fiber jet than faster ramping (on the order of seconds). This may be partially due to the already discussed time-lag issues but may also have to do with the relative magnitudes of the fluid relaxation time and the charge relaxation time near the emitter tip [26]. The combination of these factors motivated the practice of quickly ramping the high voltage within seconds after coating of the array. Doing so would result in a fast swelling of the liquid around the emitter tips followed by a burst of jets that is characteristic of what the author has coined "chaotic" electrospinning.

Mobile, Chaotic Jets

The mobile, chaotic regime is defined by an unsteady onset of electrospinning and the subsequent mobility and transience of any fiber jets that form. This regime is

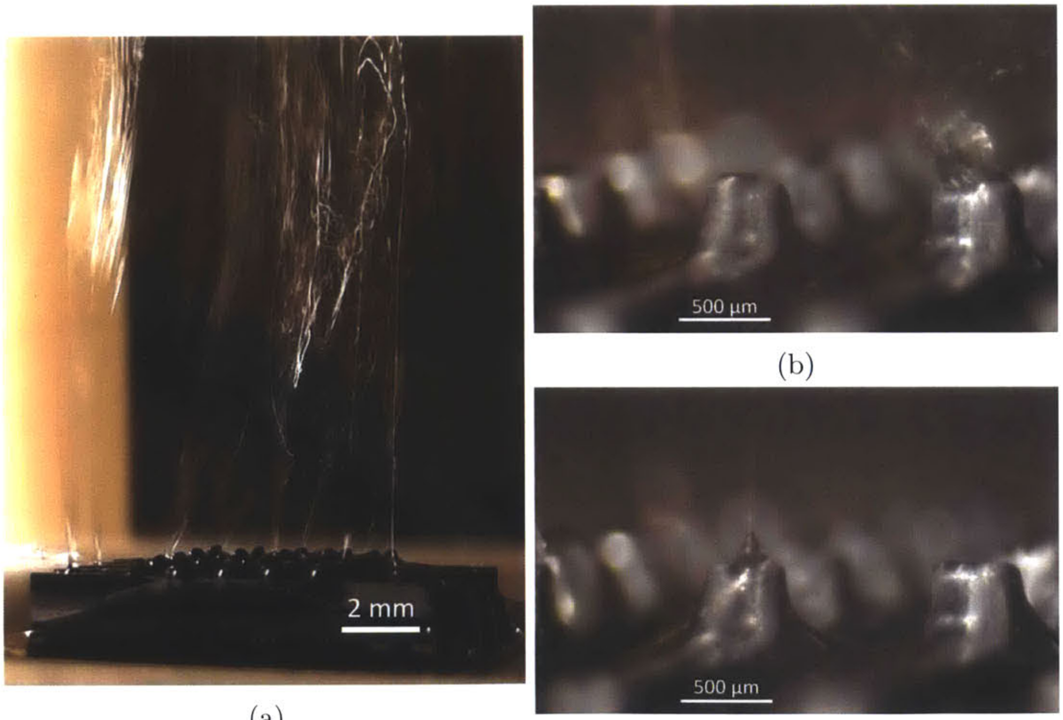

(a) (b) (c)

Figure 6-7: Mobile, chaotic regime of electrospinning: (a) Extensive whipping instability and non-localized jets are characteristic of this regime. (b) Unsteady burst-like start-up of electrospinning is observed. (c) Occasional Taylor-cone structures are observed, but they are transient.

most commonly observed for shorter, more densely packed emitter arrays. The lack of strong, localized electric field enhancement at the emitter tips means fiber jets can wander across the array in a rastering fashion. Taylor cone-like structures can be observed periodically, but they are not steady spatially or temporally. When these arrays are operated from a bath, jets will also initiate directly from the liquid surface of the bath and move freely between that surface and the array. This is essentially a modified form of free-surface electrospinning, where the presence of short emitters provides some structure to catalyze jet formation. Fiber jets exhibit very evident whipping instability in this regime (Figure 6-7).

Anchored, Chaotic Jets

The anchored, chaotic regime is, fundamentally, very similar to the mobile, chaotic regime. It is typically observed when electrospinning from taller, sharper emitters, which provide sufficient electric field enhancement to pin jets at their tips. Emission directly from the bath or array base can occur if high enough voltages are applied.

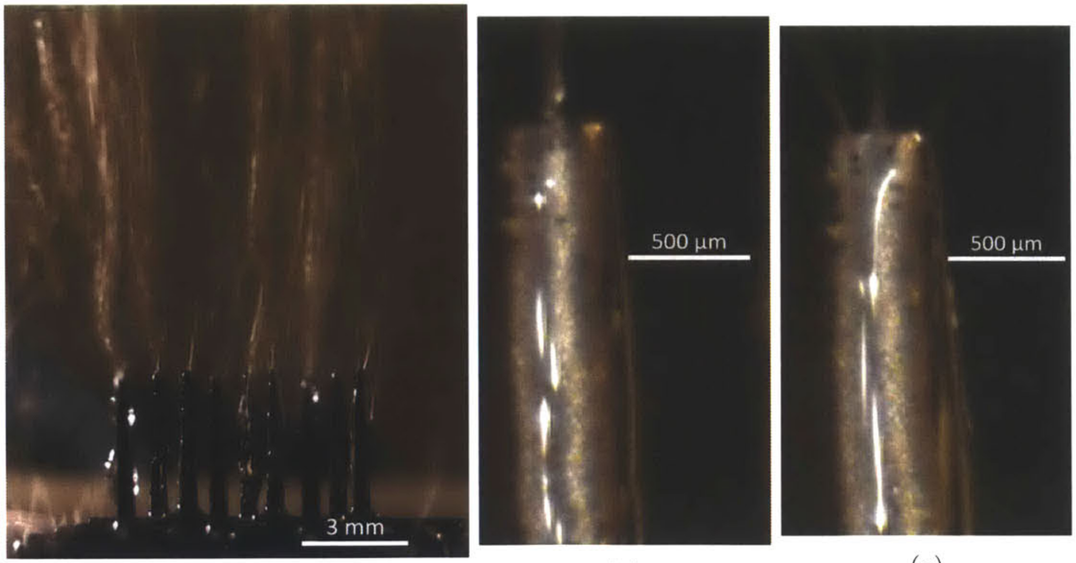

(a) (b) (c)

Figure 6-8: Anchored, chaotic regime of electrospinning:(a) Extensive whipping instability occurs but with greater localization of emission than in mobile, chaotic electrospinning. (b) Single fiber jet is observed pinned to an emitter tip. (c) Multiple fiber jets can emanate from a single emitter tip.

Sometimes, Taylor cone-like structures will be seen "climbing" the sides of the emitters, and it is possible for more than one jet to emanate from a single tip (Figure 6-8). Electrospinning in this regime offers two primary advantages. First, there is a general level of control over where the fibers will be deposited. It is far from precise due to extensive jet whipping, but it can be expected that the unwoven fiber mat will end up in the general region over the array. This is not necessarily true in free-surface electrospinning where the jets are not localized. The second, and major, advantage is that the field enhancement lowers the voltage required to spin.

Anchored, Stable Jets

The third and final regime identified is characterized by anchored, stable jets. It was discovered while attempting to lower voltage requirements by lowering the surface tension of the liquid. One way to do this is use a higher fraction of ethanol in the ethanol/water solvent, but this reduces the solubility of PEO and limits the maximum concentration solution that can be prepared. Instead, polymer solution was pipetted over the emitters as usual, but this was followed immediately by a second coating of pure ethanol before ramping the voltage. This technique not only reduces the

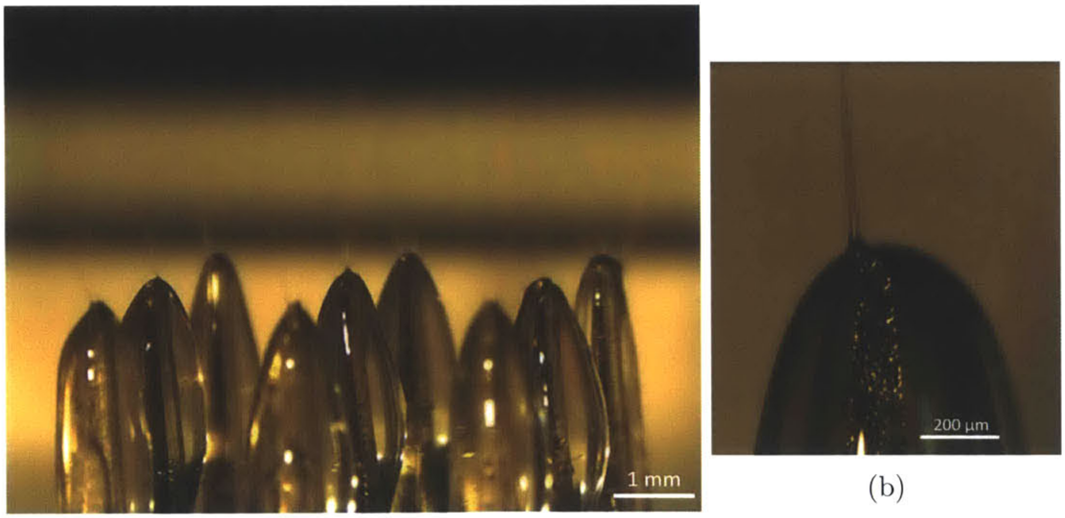

(a)

(b)

Figure 6-9: Stable regime of electrospinning: (a) 3×3 array of emitters being fully utilized in the stable regime. (b) A close-up of a single emitter tip shows a quasi-steady fiber jet.

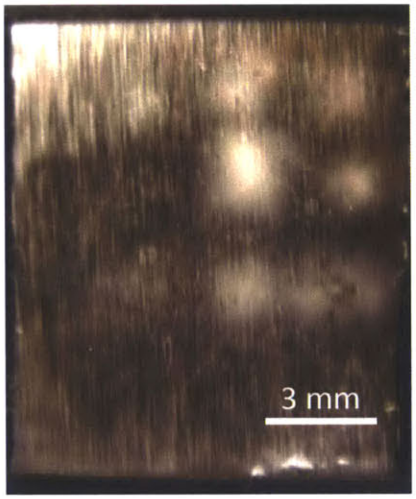

Figure 6-10: Collector imprint for stably operated 3×3 first-generation emitter array: Fibers spun stably at 1 cm working distance are deposited in a pattern mimicking the array layout and contained within the unit cell of their emitter.

starting voltages required, but it allows for a finer, often single jet to form. It is not quite the stable Taylor cone one might observe in jetting from a needle, which firmly pins the ends of the cone. The jet is "stable" in the sense that it appears to draw liquid at a slow, constant rate, even though it can, and does, wander around the tip (Figure 6-9). The mechanism behind the ethanol priming technique is not entirely understood. Although, it is expected to reduce surface tension, the effect should be minimal since the presence of ethanol mixed in the solution already significantly lowers surface tension [27].

The discovery of this regime was considered an important step towards the task of making denser emitter arrays. In the chaotic regimes, emitters fire on and off and interfere with one another due to severe whipping, suggesting they may not scale down well. Operating in the stable regime at a 1 cm working distance, emitters deposit their fibers within the extent of their unit cell creating imprints like the one seen in (Figure 6-10). This is not necessarily evidence that the whipping instability does not occur but that, at short enough working distances and low enough voltages, it might be reduced. This could be a cause for concern, since it is the whipping instability which is considered the primary force behind the tremendous thinning ratios for which electrospinning is known. However, stably spun fibers seem comparable to chaotically

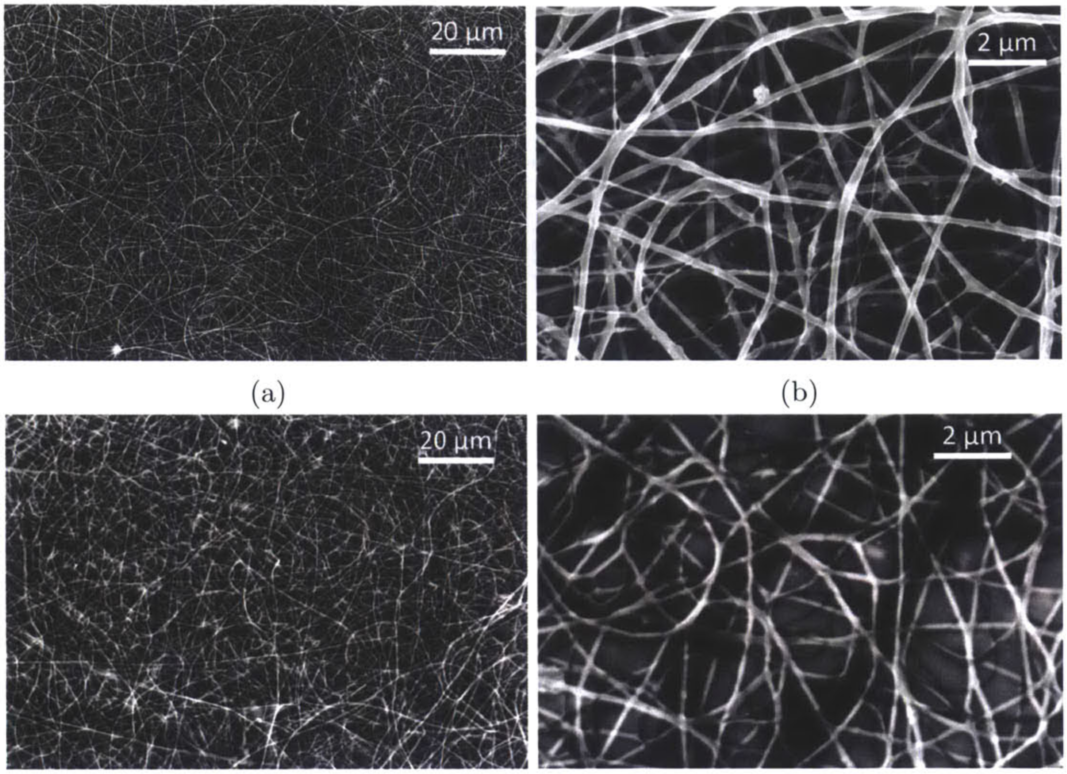

(a) (b)

(c) (d)

Figure 6-11: Comparable nanofibers spun in both chaotic and stable regimes: (a)(b) Fibers spun in the chaotic-anchored regime (c)(d) Fibers spun in the stable regime. In both cases, regions of uniform fibers with average diameters on the order of 200 nm were produced.

spun fibers when viewed under an SEM (Figure 6-11).

Either regime of spinning can produce unwoven mats of nanofibers with diameters on the order of a few hundred nanometers. However, in both cases, the output of the process was not entirely uniform. Although clean fibers were produced, regions on the collector exhibited messier-looking fibers or non-fibrous polymer deposits (Figure 6-12). It was initially suspected that some of the structures observed were formed via melting of polymer during gold coating of the fibers or SEM imaging. Another possible explanation was that the short working distances used did not permit sufficient whipping and evaporation of solvent; however, in some regions of the collector there were clearly dried fibers. As it turns out, the alternative polymer structures may result from simultaneous electrospray of solvent over the nanofibers, causing their dissolution on the collector. This theory was developed based on the second round of experiments and will be discussed in the following section.

Figure 6-12: Alternative polymer structures on collector electrode: Polymer structures containing radial striations and interesting grain boundaries were observed in some regions of the collector. Later experiments suggest this may result from electrospray of solvent over deposited fibers.

6.2.2 Second-Generation Devices

Using the second-generation experimental apparatus, electrospinning was performed from both larger and denser arrays than those previously tested. Operating at a 1 cm working distance, we achieved full array utilization in the stable regime producing deposits on the collector that match the shape and size of the array used (Figure 6-13). Arrays as large as 15×15 emitters with an emitter density of 25 emitters per cm^2 were tested. The largest array tested produced a total mass flow rate of $74 \pm 9.25\left[\frac{mg}{hr}\right]$ or a mass flux of $82 \pm 10.25\left[\frac{g}{hr \cdot m^2}\right]$. This is on the same order of magnitude as the $100\left[\frac{g}{hr \cdot m^2}\right]$ produced by the leading free-surface electrospinning technology [50]; however, our array was operated at 8.2 kV as opposed to the 30-100 kV typically used in commercialized free-surface electrospinning sources.

Electrospinning was also performed at larger working distances. For tip-to-collector distances of 2 and 3 cm, collector imprints were no longer comprised of a one-to-one,

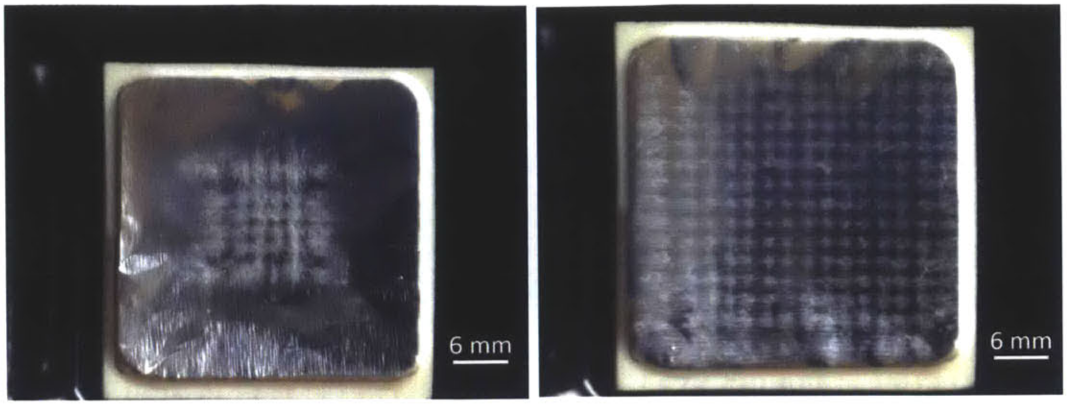

(a) (b)

Figure 6-13: Collector imprints from second-generation emitter arrays operated at $WD = 2cm$: (a) Imprint from a 6×6 array of emitters with 125 μm tip radius spaced 2 mm apart (b) Imprint from a larger 15×15 emitter array with the same tip radius and spacing. In both cases, all of the emitters in the array are utilized leaving more or less similar imprints in which the deposits match up with the emitter positions in a one-to-one fashion.

matching array of dots. Instead, deposition occurred more uniformly over the area of the array creating one large patch of white deposits (Figure 6-14). This is likely due to greater growth of the whipping instability as the fiber jet travels a longer distance to the collector. It should be noted that, although the whipping instability is evident, the nature of the emission at the tips was fairly "stable," even at these larger distances, for virtually all tests. This is likely a consequence of improved alignment in addition to the use of ethanol priming for most of the second-generation device characterization.

For some of the arrays tested at these larger working distances, mass flux was greater than it was at 1 cm working distance (Table 6.1). This may seem counter-intuitive but makes sense if one considers the field enhancement of different parts of the array at different working distances. Edge emitters will always have higher enhancement factors than interior emitters in our setup but this advantage increases the closer the array is to the collector. If mass flow rate is dependent on local electric field strength, then it would be expected that, at shorter working distances, a greater fraction of the deposited mass comes from edge emitters. Since there is a threshold voltage at which arcing to an edge emitter occurs, field strength at interior emitters

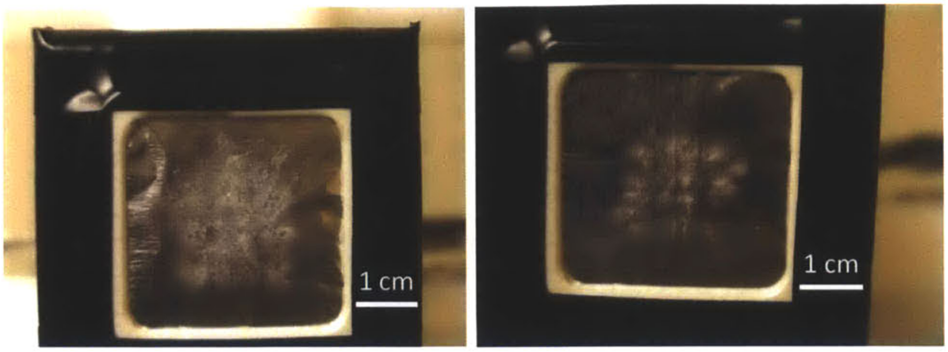

(a) 4×4, WD = 2 cm, s = 3 mm, $R_{Tip} = 250\mu m$, V = 18kV, 4% PEO in 40/60 (eth/water), 3×15s cycles

(b) 4×4, WD = 2 cm, s = 3 mm, $R_{Tip} = 250\mu m$, V = 18kV, 6% PEO in 25/75 (eth/water), 3×15s cycles

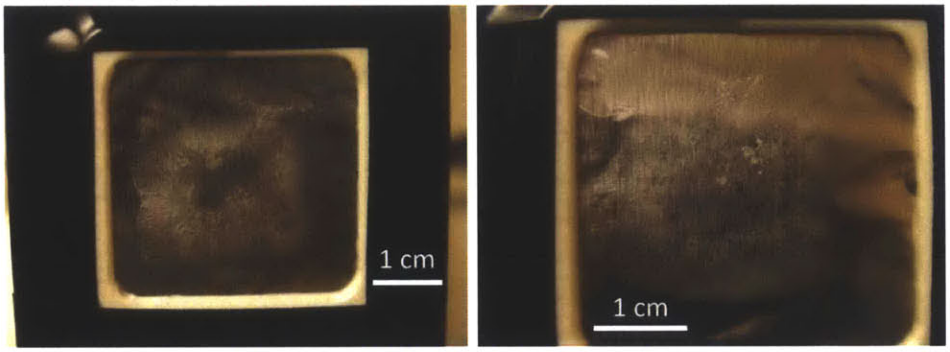

(c) 4×4, WD = 3 cm, s = 3 mm, $R_{Tip} = 250\mu m$, V = 25kV, 4% PEO in 40/60 (eth/water), 3×10s cycles

(d) 6×6, WD = 3 cm, s = 3 mm, $R_{Tip} = 250\mu m$, V = 25kV, 4% PEO in 40/60 (eth/water), 3×10s cycles

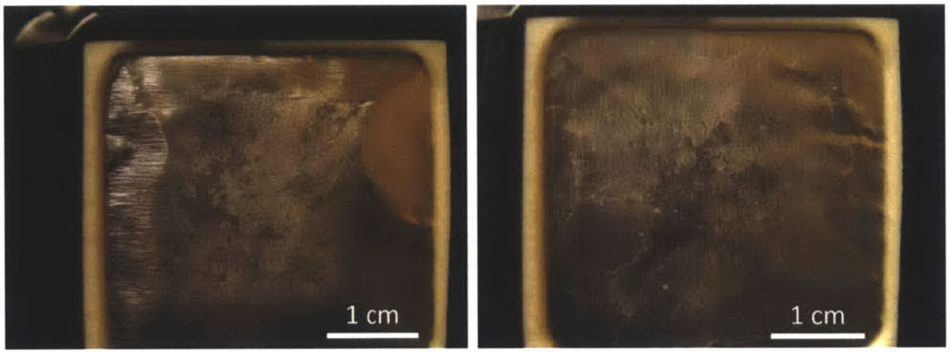

(e) 6×6, WD = 3 cm, s = 3 mm, $R_{Tip} = 250\mu m$, V = 25kV, 4% PEO in 40/60 (eth/water), 10×10s cycles

(f) 6×6, WD = 3 cm, s = 3 mm, $R_{Tip} = 125\mu m$, V = 25kV, 4% PEO in 40/60 (eth/water), 3×10s cycles

Figure 6-14: Collector imprints for second-generation emitter arrays operated at $WD \geq 2\ cm$: Deposits are less localized at working distances greater than 1 cm due to growth of the whipping instability. The instability is reduced with higher viscosity (b). At $WD = 3\ cm$, the deposition area becomes noticeably larger than the array itself, again due to growth of the whipping envelope (c-f). "Empty" patches appear within the deposits in some cases (c,e,f); however, SEM imaging confirms the presence of alternative polymer structures.

can only be increased so much. At larger working distances, the difference in field enhancement between edge and interior emitters is smaller. Near the threshold arcing voltage (which is now larger due to the larger working distance), it would be expected that the relative field strength at the interior emitters compared to edge emitters would be greater than it was for shorter working distances. Therefore, the average field felt across the array would increase, which could explain the increased mass flow rate.

Size	V [kV]	WD [cm]	s [mm]	$R_{Tip}[\mu m]$	$\dot{m}_{avg}\ [\frac{mg}{hr \cdot emitter}]$	Flux $[\frac{g}{hr \cdot m^2}]$
6 × 6	8.2	1	2	125	0.15±0.05	37.5±12.5
15×15	7.2	1	2	125	0.16±0.04	40±10
6×6	7.2	1	2	125	0.25±0.05	62.5±12.5
15×15	8.2	1	2	125	0.33±0.04	82.1±10.3
6×6	25	3	2	125	1.0±0.33	250±83
6×6	25	3	2	250	1.3±0.10	325±25
4×4	18	2	3	250	3.5±0.50	389±56
4×4	25	3	3	250	3.75±0.75	417±83

Table 6.1: Mass production rates of various second-generation emitter arrays: Increasing array size at constant density increased the mass flux. Increasing density, on the other hand, reduced mass flux for the arrays tested.

The data show greater mass flux for arrays with more emitters when all other parameters are equal. This may seem trivial, but it is an important result suggesting that the design can be scaled up without a loss of productivity. However, increasing the number of emitters at a fixed array size or, rather, increasing the emitter density did not improve productivity for the arrays tested. At increased emitter density, electrical shielding of interior emitters is greater so they see a lower effective field strength. This was made especially clear by the fact that our arrays with 1-mm emitter spacing did not even fire. The results suggest that for the particular emitter designs used, the optimal spacing within the array is greater than 2 mm. It is important to note that this does not necessarily hold true generally. For narrower, sharper emitters one would expect the optimum spacing to be lower.

One related issue that was observed while testing is that, at lower voltages, the full

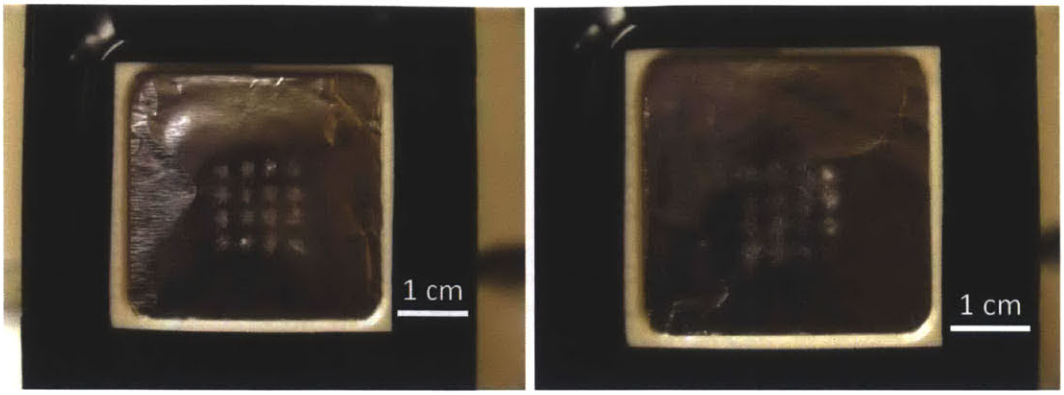

(a) (b)

Figure 6-15: Collector imprints of second-generation arrays using edge electrode for uniformity: (a) Deposition is highly localized using an edge electrode at 1 cm working distance (b) Using an edge electrode at 2 cm working distance, deposition is less localized than at 1 cm but much more so than the case of 2 cm working distance without the edge electrode (Figure 6-14(a))

array was not utilized. Some subset of the emitters would fire, and it was typically those closer to the edge of the array as one would expect due to electrical shielding of the interior emitters. Although full utilization could usually be achieved by increasing the voltage sufficiently, this does not mean each emitter experiences the same field strength, as was previously discussed. Therefore, per-emitter emission might not be uniform across the array; in particular, the outer emitters are expected to experience larger fields than the inner emitters. For this reason, an edge electrode was briefly investigated on a 4x4 array of emitters with 3 mm spacing. Similar work with ring electrodes has demonstrated improved uniformity due to reduced field enhancement at the array edge [51]. Our edge electrode was nothing more than several layers of aluminum foil constructed to form a flat, conducting surface encircling the array edge at a distance of roughly 3 mm (i.e., the emitter spacing for the arrays used in these tests). The edge electrode sat approximately 2 mm below the plane of the emitter tips and was grounded with the emitter array. This effective shortening of the emitters resulted in such reduced field enhancement that the array did not fire without ethanol priming. With ethanol priming, the array was fired at working distances of 1 cm and 2 cm; imprints are shown in Figure 6-15. The electrode seems to yield more uniform looking imprints. This is especially conspicuous when comparing

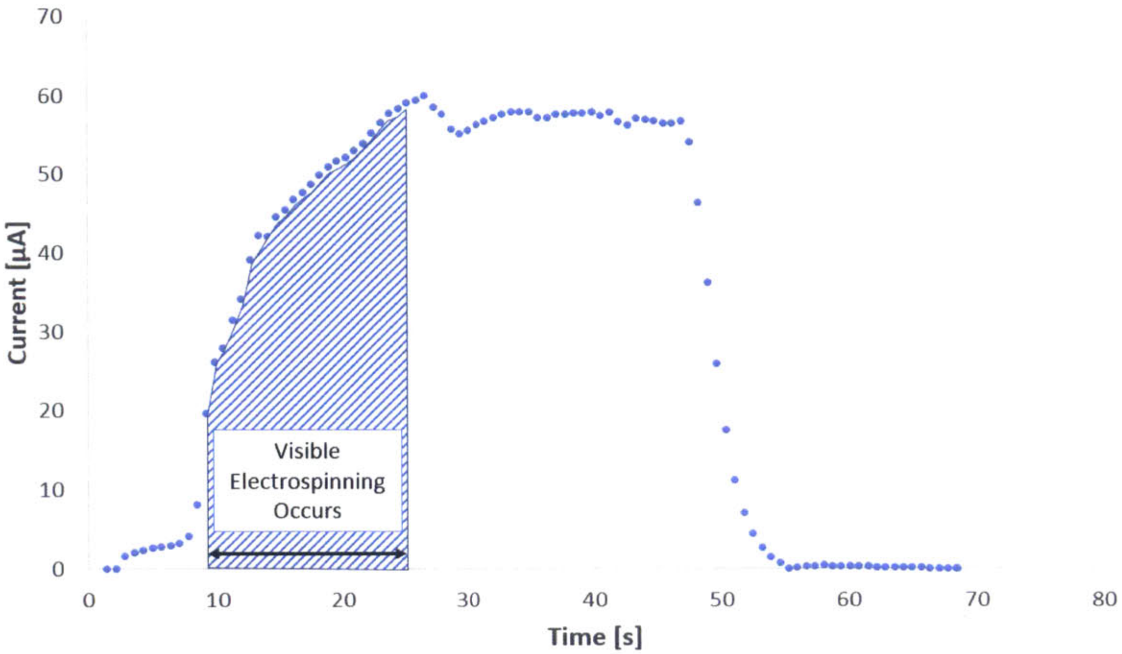

Figure 6-16: Current vs. time for typical run of electro-hydrodynamic jetting: Visible electrospinning occurs in the transient period indicated above, but current continues to flow even after visible jetting ceases. Analysis suggests this is due to electrospray.

electrospinning with and without the electrode from the same array at 2 cm working distance. The electrode helps retain the one-to-one mapping of emitters to deposit-spots that is otherwise lost when moving from 1 cm to 2 cm working distance.

Testing of the second generation devices with the Bertan power supply provided an opportunity to record current measurements as a function of applied voltage. We observed that the current readings during any individual electrospinning run were not steady; that is, electrospinning from the coated arrays seems to be a transient phenomenon. Spinning would usually commence during the voltage ramp just before the plateau was reached. Once voltage leveled off, current would continue a generally increasing trend until visible electrospinning ceased. If the high voltage was maintained beyond this time, current would continue to flow, either increasing until tripping the power supply or leveling off at a constant value (Figure 6-16).

The first issue this posed was that of how to analyze the current data. Quantitative models for emitted current have been developed in some of the electrospinning and electrospray literature [22, 23]; however, almost all of them describe traditional needle

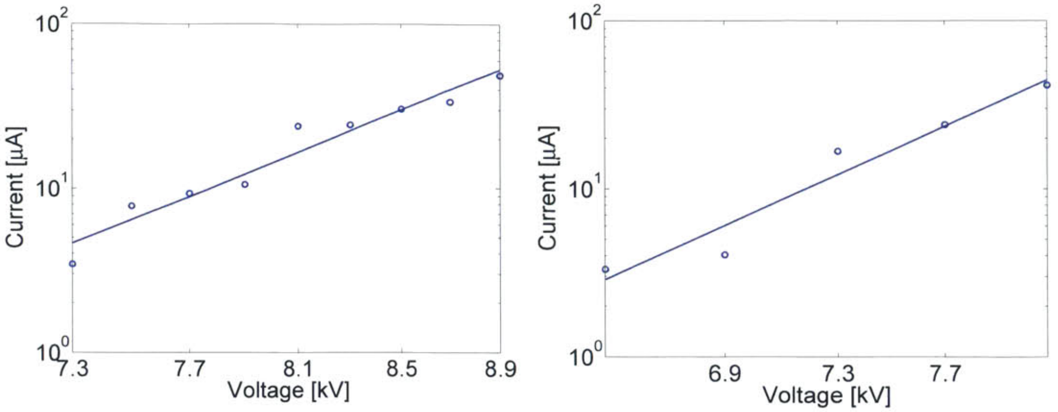

(a) 6×6, $R_{Tip} = 250\mu m$, WD = 1 cm, No ethanol priming

(b) 6×6, $R_{Tip} = 250\mu m$, WD = 1 cm, Ethanol priming

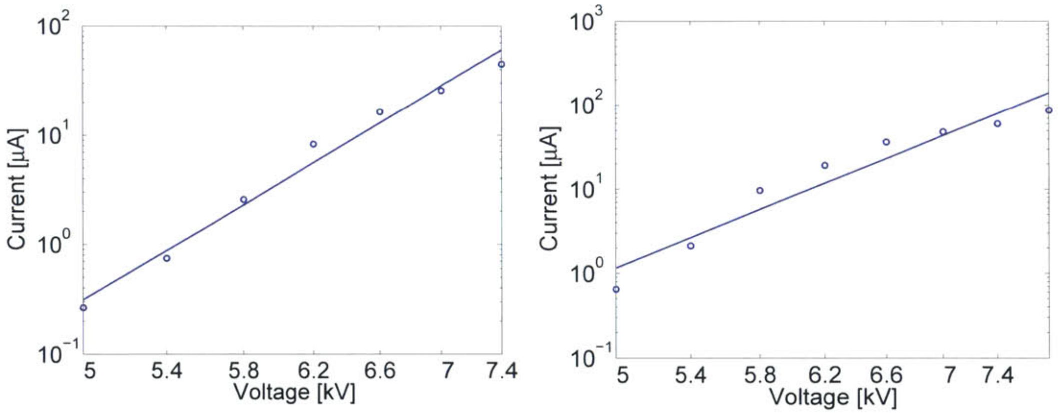

(c) 6×6, $R_{Tip} = 125\mu m$, WD = 1 cm, No ethanol priming

(d) 6×6, $R_{Tip} = 125\mu m$, WD = 1 cm, Ethanol priming

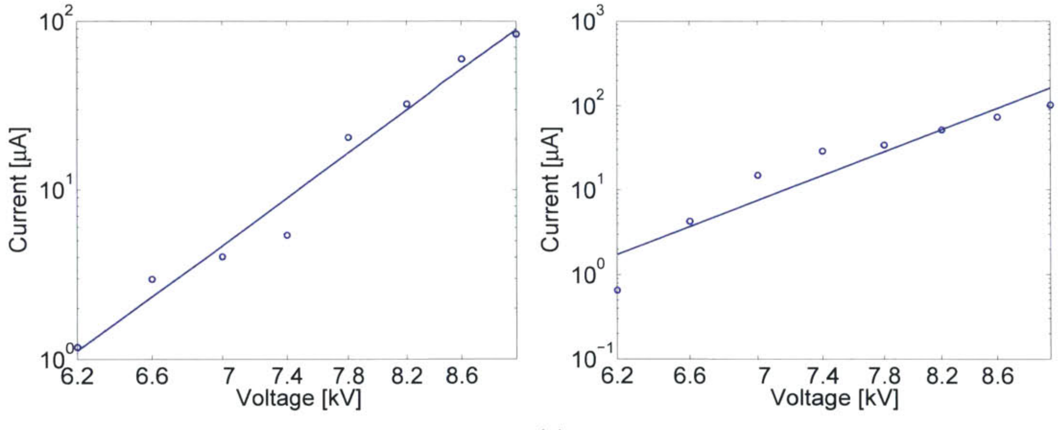

(e) 10×10, $R_{Tip} = 125\mu m$, WD = 1 cm, No ethanol priming

(f) 10×10, $R_{Tip} = 125\mu m$, WD = 1 cm, Ethanol priming

Figure 6-17: Average current vs. voltage for electro-hydrodynamic jetting: Average current is plotted vs. operating voltage and fitted with a power law ($I = k_V V^{p_V}$) for various arrays. The coefficient of determination (R^2) for the fits is also given. (a) $p_V = 12.29$; $R^2 = 0.9719$ (b) $p_V = 12.44$; $R^2 = 0.9705$ (c) $p_V = 13.40$; $R^2 = 0.9915$ (d) $p_V = 10.79$; $R^2 = 0.9661$ (e) $p_V = 11.74$; $R^2 = 0.9878$ (f) $p_V = 12.18$; $R^2 = 0.9435$.

jetting in which flow rate is an independent variable rather than a response of the system to some applied voltage. Electrospinning current has been empirically modeled with a power law in the applied voltage at fixed flow rates ($I = k_V V^{p_V}$) [44]. We decided to follow this approach, averaging the current over any individual run and fitting these averages versus applied voltage. The plots and fitted exponents are shown in Figure 6-17. For the arrays tested, the fitted exponent falls between 10 and 14 with an average around 12. This is much larger than the powers reported previously for traditional needle electrospinning of the same polymer solution, which are around 3 [44]. There are several plausible explanations for this discrepancy. The first is that flow rate is not constant in our experiments. If flow rate is itself a function of the applied voltage and current depends on both voltage and flow rate, then increasing the voltage raises the current by simultaneously increasing conduction and convection of the fiber jet. Another factor that would explain the larger exponent is unequal utilization of the array at different voltages. In this case, increasing voltage not only increases the conducted and convected current from a single emitter but the number of emitters that fire. In the same vein, larger voltages are capable of drawing multiple jets from a single emitter. The combined effect of all of these factors is that current should scale much more quickly with voltage for an externally-fed array than for a single emitter with controlled flow rate.

The other main issue with the data is the persistent current after the cessation of visible electrospinning. One hypothesis was that fiber jets continued to transport current, but they became so thin as to no longer be visible on a magnified video recording. This seems reasonable; however, thorough examination of the collector foil after runs where current was measured in the absence of visible jetting yielded no trace of fibers under an SEM. Such was the case for all tests using a 10×10 array of emitters spaced at 1 mm (the densest array fabricated). Instead of fibers, we observed small specks of polymer distributed fairly uniformly within circular regions on the foil that lined up with the edge emitters (Figure 6-18).

It seemed that the deposits and unexplained current were both the result of electrospray, which is typically observed for less viscous conductive liquids. High viscosity

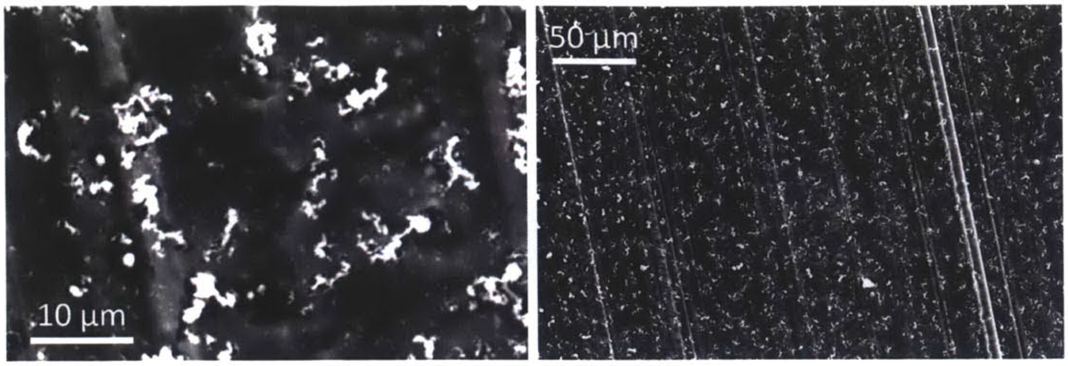

(a) (b)

Figure 6-18: Polymer particles deposited by electrospray: (a)/(b) Polymer specks deposited by electrospray vary between 1 and 5 μm in size. Within the deposition area, the particles are very uniformly dispersed.

liquids usually produce fibers in a strong electric field, but it is possible that a lack of sufficient liquid flow at the emitter tips resulted in droplet formation. Electrospray has been extensively studied and minimum droplet size has been shown to scale as $R_{drop,min} = (\frac{\gamma \tau_e^2}{8\rho})^{1/3}$ where $\tau_e = \frac{\epsilon_r \epsilon_0}{K}$ is the electrical relaxation time, ϵ_r is the relative permittivity of the liquid, and K is the conductivity of the liquid. This predicts a minimum droplet diameter of about 0.5 μm for 4% PEO in 40/60 ethanol/water ($\gamma = 40[\frac{mN}{m}]$, $\rho = 916[\frac{kg}{m^3}]$, $K = 1.15[\frac{mS}{m}]$, and $\epsilon_r = 66.57$ [44]). The specks of polymer observed on the foil have diameters ranging primarily between 1 μm and 5 μm, with none larger than 10 μm. If we assume that the specks were left behind by the evaporation of a droplet of the working liquid, this means the initially emitted droplet would have had a diameter approximately three times larger than the speck. Such droplets are safely above the 0.5 μm lower limit suggesting this could be the mechanism at play.

However, the appearance of the specks is not necessarily what one would expect had they formed via evaporation of solvent, which would likely leave a spread out film. They appear as a more concentrated mass almost as though they has precipitated out of solution. Another possible explanation of the results is that they are caused by ethanol priming. Depositing ethanol over the emitters that have already been coated with polymer solution may leave a thin film of ethanol on the surface. This ethanol has much lower viscosity than the polymer solution and is, therefore, more likely to electrospray. Also, PEO is significantly less soluble in ethanol than it is in water. If the ethanol concentration right near the emitter tips becomes very high during priming, it is feasible that PEO might precipitate out of solution and be carried to the collector inside droplets. Studies of PEO precipitation have verified particle sizes on the order of a few microns in agreement with our observations [52, 53].

Whether it was the polymer solution, pure ethanol, or some mixture of the two, it is highly likely some kind of electrospray occurs from our arrays. This discovery helped shed light on another confusing result from our device characterization; i.e., regions of fiber deposits appeared degraded. Alternative polymer structures had been observed previously but were less common and could not be explained. We now believe that many of them are formed by the electrospray of solvent, which is occurring simultaneously with or immediately after electrospinning of fibers. This dissolves the fibers on the collector resulting in several of the structures shown in Figure 6-19. In some cases the dissolution is partial and fibers are still visible within the slime. In other cases, the cracks fully coalesce into a blanket of polymer, which is relatively smooth except for interesting grain boundaries in its surface. Specks of polymer, like those deposited during isolated electospray, were found mixed in with many of the fiber deposits. They are often located at the center of the grain boundaries, which might very well be formed by deposited droplets.

Before hypothesizing the electrospray explanation, it was thought that the alternative polymer structures might simply result from insufficient evaporation of solvent due to a short working distance. This can occur and will often result in "cross-linked" fibers. However, previous experiments had successfully spun very clean, uniform fibers at the same working distances, and, unlike the electrospray hypothesis, this would not explain the anomalous current after fiber spinning has ceased nor the speck-like deposits observed. It is very likely that electrospray is occurring and also occurred during earlier testing (see figure 6-12), perhaps just less noticeably. It can be that using larger, denser arrays and enclosing the testing area causes the air to quickly saturate and, therefore, reduces evaporation rates of both fibers and sprayed droplets,

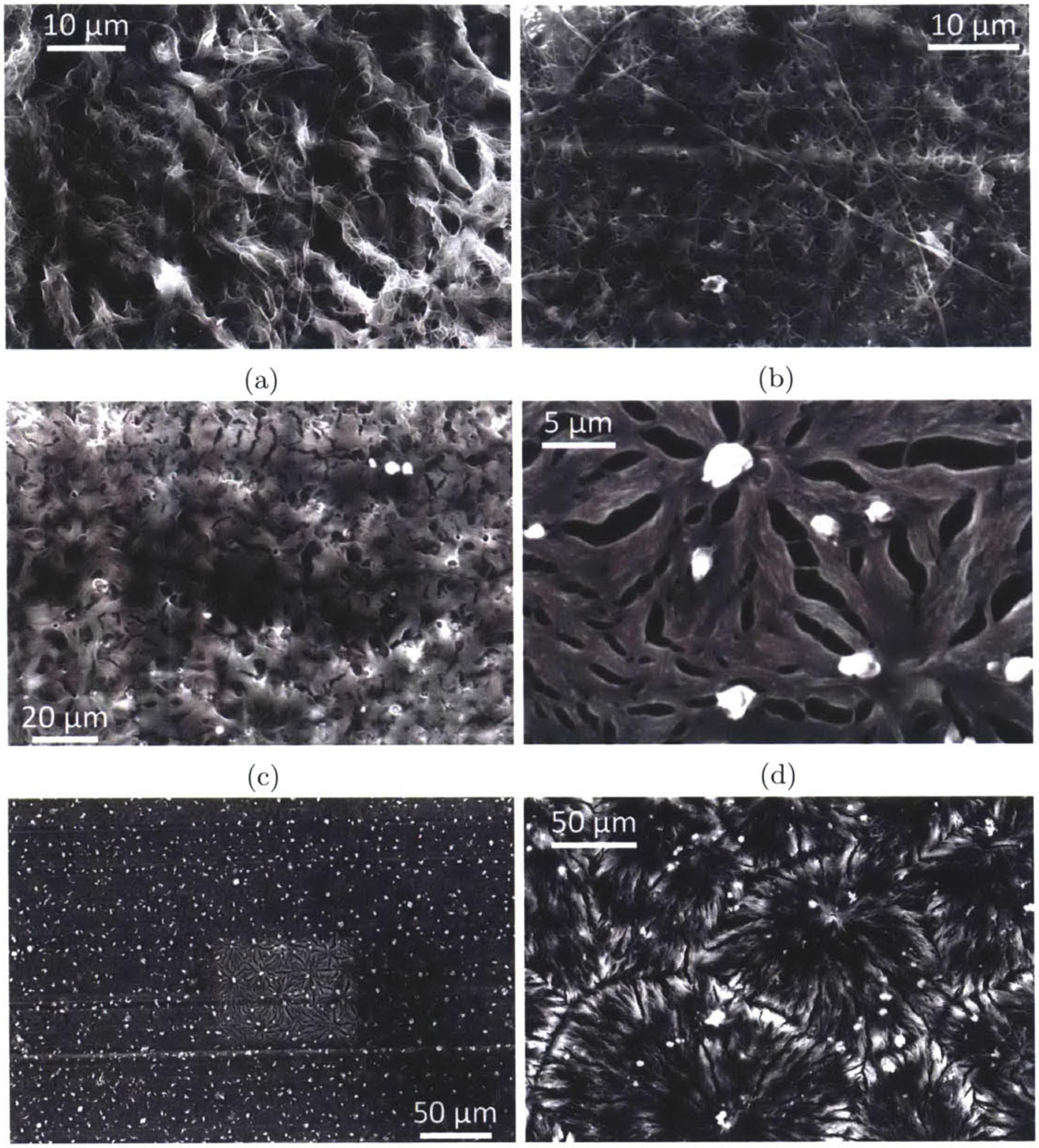

(a) (b) (c) (d) (e) (f)

Figure 6-19: Alternative polymer structures formed during electro-hydrodynamic jetting: (a) Nanofibers are clearly visible among the dissolved polymer slime (b) Nanofibers are present but partially dissolved (c) Fibers have completely coalesced into ribbon like structures (d) Polymer particles sitting on top of striated polymer layer. It is likely electrospray of solvent deposited the particles and dissolved underlying nanofibers to form some of these structures. (e) Zoomed out view of particles shows modified structure in previously imaged area. Solid layer may be sitting over a porous bed of fibers. (f) Grain boundaries in the polymer layer could indicate the locations of droplet deposition.

resulting in more moisture reaching the collector and greater fiber degradation. This would also explain the observation of better fibers near the array edges as compared to the center.

That said, the alternative polymer structures are interesting and potentially useful in their own right. The electrospray observed could be used to evenly disperse fine droplets of some viscous catalyst that would otherwise be difficult to atomize. Better control over the balance of spinning and spraying might enable reliable fabrication of partially dissolved ridge-like structures that can be optimized for biological applications such as tissue engineering. Electrospraying solvent over already formed nanofiber mats can dissolve the top region to form an impermeable boundary for controlled integration with other layers.

6.2.3 Electrospray from Microchannel Chip

Although the optimal microchannel structures were not directly integrated on the emitter arrays, it was still of interest to characterize their liquid transport properties in the context of electro-hydrodynamic jetting. This was accomplished by using the samples from the wicking characterization directly as emission sources. A chip with open microchannels was supported vertically in a bath of liquid and its position was adjusted so that the liquid would rise all the way to the top edge of the sample. High voltage was applied in step increments, and the current response was recorded.

With water as the working liquid, electrospray initiates at some threshold voltage and the measured current increases quickly just beyond this voltage. Further increases in voltage result in a more slowly increasing current that varies linearly with the voltage (Figure 6-20). In the early stages, the process is barrier-limited. The electric field distribution and Taylor cone determine the flow rate, which grows at an increasing rate with growing electric field strength. In the later stages, the electrospray becomes supply-limited. The growing flow rate results in growing viscous losses, which limits the delivery of more liquid. This concept is analogous to the steady-state of a skydiver who has reached terminal velocity.

Previous work has shown that electrospray current for viscous liquids varies as

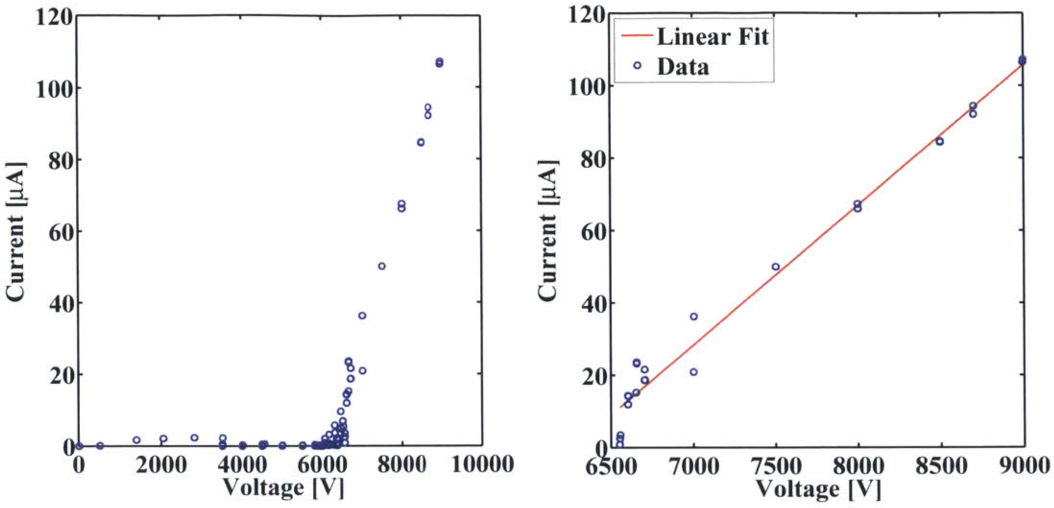

(a) (b)

Figure 6-20: Average current vs. voltage for electrospray of water from wicking sample: A linear relationship between average current and voltage is observed ($I = a_1 V + a_0$, where $a_1 = 3.870 \times 10^{-2}$and $a_0 = -2.425 \times 10^2$). The coefficient of determination for the fit is $R^2 = 0.9812$.

the square root of the flow rate [23]. Calvo et al. confirm this relationship by independently adjusting flow rate with a pump; however, in our electrospray process, flow rate is a dependent variable decided by the parameters of the experiment. Although we could not directly measure flow rate, we suspect that our results are consistent with the previously studied scaling based on the following argument. Flow through the designed wicking structures can be described with Darcy's law, which states that the flow rate is proportional to the pressure gradient. In our experiments, surface tension will wick the liquid to the sample edge, but it is the electric field that provides the driving pressure behind the spray. Electrostatic pressure at a conducting surface scales as the square of the normal electric field, and, for a fixed testing setup, the electric field at a particular location is proportional to the voltage. Therefore, the flow rate should scale as the square of the applied voltage ($Q \propto \nabla p \propto E^2 \propto V^2$). Combined with the experimental observation that current varies linearly with voltage, this implies that $I \propto Q^{\frac{1}{2}}$ in agreement with previous reported work.

Electrospinning was attempted by repeating the previous experiment using 3% PEO in 50/50 ethanol/water. Following the same procedure we used for spraying water, we observed electrospray, not electrospinning, of the PEO solution. The current versus voltage characteristics are plotted in Figure 6-21. The behavior is not as overtly linear as it was for electrospraying water. We attribute this to the shear-thinning properties of the PEO solution, which can be modeled as a power-law fluid ($\bar{\bar{\tau}} = \eta(\frac{\partial u}{\partial y})^{n_p}$). Under this model, the effective viscosity varies as some constant times the strain rate to the $(n_p - 1)$ power ($\mu_{eff} = \eta(\frac{\partial u}{\partial y})^{n_p - 1}$). For a fixed flow geometry, the strain rate is proportional to the flow rate. The value of n_p will be less than one for a shear-thinning fluid. In chapter 5, a similar PEO solution was well-described with a value of $n_p \approx \frac{1}{2}$. This would suggest $\mu_{eff} \propto (\frac{\partial u}{\partial y})^{-\frac{1}{2}} \propto Q^{-\frac{1}{2}}$. Darcy's law states that flow rate is proportional to pressure gradient and inversely proportional to viscosity. If pressure still scales as V^2, then we have $Q \propto \frac{\nabla p}{\mu_{eff}} \propto \frac{V^2}{Q^{-\frac{1}{2}}}$ which implies $Q^{\frac{1}{2}} \propto V^2$. If we assume that current still scales with the square root of flow rate, as it should for viscous droplets, then current should vary as the square of applied voltage. Our observations validate this scaling.

Observing the collector electrode following electrospray of the polymer solution

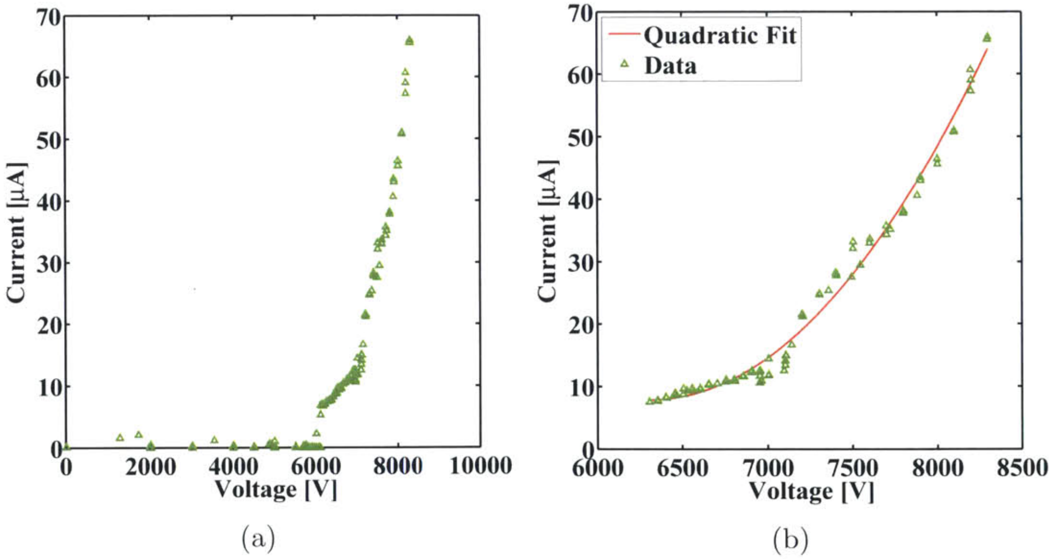

(a) (b)

Figure 6-21: Average current vs. voltage for electrospray of 3%PEO in 50/50 ethanol/water from wicking sample: A quadratic relationship between average current and voltage is observed ($I = a_2V^2 + a_1V + a_0$, where $a_2 = 1.417 \times 10^{-5}, a_1 = -1.788 \times 10^{-1}$and $a_0 = 5.718 \times 10^2$). The coefficient of determination for the fit is $R^2 = 0.9864$.

revealed two primary deposition areas above either corner of the wicking sample. This suggests liquid is wicking through the open microchannels to the top edge of the sample where it then travels along the edge to the corner. Electrospray occurs from these sharp corners, not from the open end of each microchannel as we initially suspected. Also, it is worth noting that, although electrospinning did not occur from the sample when liquid was transported passively, it did occur briefly when the samples were coated in a manner similar to the emitter arrays. This may merely be confirmation that the wicking structures cannot supply a sufficient flow rate on their own; it takes coating the emission area with an excess of polymer solution to initiate electrospinning. However, the fact the electrospray did not occur directly from the microchannel openings permits another hypothesis. It is possible that the fine details of the emission site matter tremendously for electro-hydrodynamic jetting processes, as is suggested by Hohman et al. [26]. The exact geometry, the wetting properties, the local meniscus curvature, the fluid relaxation time, the electrical relaxation time, and the electric field distribution are interrelated and may need to be very precisely balanced to initiate highly localized jetting.

Chapter 7

Summary and Conclusions

This thesis entailed the design, micro-fabrication, and characterization of externally-fed emitter arrays for parallel nano-manufacturing via externally-fed electro-hydrodynamic jetting. We described criteria for maximizing the flow rate per unit area in capillary rise against gravity through porous surfaces comprised of micropillars and microchannels. Microfabricated samples of such surfaces were tested and shown to agree with our theoretical flow predictions. The tests also confirmed that microchannel structures are capable of passively transporting greater flow than comparable micropillar structures. Beyond their obvious significance for controlling externally-fed emitter arrays, these findings have important implications for other research such as maximizing heat transfer via wicking of some coolant or phase-change medium in heat pipes.

We achieved electrospinning from two-dimensional arrays with as many as 225 emitters spaced as close as 2 mm apart. To our knowledge, this is the largest and densest array comprised of fixed, precisely located emitters that has been used to electrospin nanofibers. Keeping all other parameters constant, it has been shown that increasing the size of the array (i.e., more emitters at fixed density) increases the total throughput. This serves as a proof-of-concept that the production method studied can be scaled up without losses in productivity. On the other hand, increasing density was shown to decrease mass production rate per unit area (i.e., mass flux); we achieved the highest mass flux from our sparsest emitters (3 mm spacing). This suggests that, for the emitters fabricated, there is an optimal density at some spacing greater than 2 mm. It is likely that this optimal spacing can be reduced by modifying the emitter geometry, for example by further sharpening the tips.

The largest mass flux measured was on the order of 400 $[\frac{g}{hr \cdot m^2}]$ for applied voltages of 25 kV. This is several times the production rate of the leading, commercialized free-surface electrospinning technology (100 $[\frac{g}{hr \cdot m^2}]$ at 30-100 kV) [50]. We achieved production rates as high as 80 $[\frac{g}{hr \cdot m^2}]$ with voltages as low as 8.2kV. This highlights the benefit of using electric field enhancing structures for lowering power requirements and, therefore, reducing costs associated with high voltage design.

Operating at working distances on the order of 1 cm, we were able to spin in a "stable" regime where the deposits from each emitter in the array are collected in a one-to-one fashion mirroring the shape of the array. Improving positional accuracy of the deposition is essential for developing direct-write fabrication methods. We have also demonstrated the capability to emit different charged species, sometimes simultaneously, from the same hardware. Although, this can be viewed as detrimental if a single output is desired, improved understanding and control of the different modes of operation can pave the way toward the development of complex, ultra-precise 3D-printing sources.

7.1 Future Work

A natural direction for continuation of this research would be to explore better wicking structures that can enable continuous electrospinning with passive liquid delivery. Increasing channel size from on the order of 100 μm to on the order of 1 mm would help increase flow. However, such a large channel would place a limit on the emitter packing density. One approach that could work is using wider wicking channels to access greater flow rates but abruptly narrowing them right at the end of the emitter to create an ultra-sharp tip. Other possibilities include the incorporation of high-slip surfaces, which can lower viscous resistance and allow for gravity-driven liquid delivery at reasonable flow rates.

One way to more directly control the electric field distribution, improve uniformity, and lower operating voltage requirements is to incorporate an individually-gated extractor electrode. This has been successfully demonstrated in previous electrospray research [25]. Spaced very closely to the array, such an extractor can make the most of the field enhancing properties of sharp tips and resolves the problem of emitter shadowing. Beyond the extractor, a collector electrode can be placed farther away than usual, since it is no longer responsible for initiating the jetting process. This would allow more time for whipping of the jet and evaporation of solvent, which could potentially produce even thinner, more uniform fibers. Also, if the whipping instability could be delayed until farther downstream, it could reduce possible space charge effects that may lower emitter output. One issue that must be addressed when using a proximal extractor electrode is the possibility of the emitted species being intercepted. In electrospray, partial interception of the droplet or ion plume is possible and may be acceptable depending on the application. If interception of the jet occurs in electrospinning, then no fiber is transmitted past the extractor, and the process is rendered inoperative.

The electrical characteristics of different emitter tip geometries should be very carefully studied. It may be that very slight variations in structure, or even material properties, are responsible for different preferential modes of electro-hydrodynamic jetting: electrospinning, cone-jet electrospray, micro-dripping, etc. In the same vein, the electrical interference between neighboring emitters in an array as well as with the surrounding materials of the testing apparatus needs to be better understood. Knowing these effects and carefully controlling them can be the first step towards developing versatile nano-manufacturing techniques that take advantage of the "room at the bottom" with high enough productivity to be of practical benefit to mankind.

Appendix A

Derivation of Capillary Flow Model

For low Reynolds number flow in which inertial forces are negligible, we can write the equation of motion as:

$$\mu\nabla^2 v = -\nabla p \tag{A.1}$$

If we assume fully-developed, one-dimensional flow along the axis of an open rectangular microchannel of width w and height h, the problem reduces to:

$$(\partial_x^2 + \partial_y^2)v_z(x,y) = \frac{\Delta p}{\mu l} \tag{A.2}$$

With no slip boundary conditions on the three channel walls and a no stress boundary condition on the open face (ignoring the meniscus), we can solve for the velocity profile using Fourier series. The solution is given as:

$$v_z(x,y) = \frac{4w^2}{\pi^3}\frac{\Delta p}{\mu l}\sum_{n,odd}^{\infty}\frac{1}{n^3}\left[1 - \frac{\cosh(\frac{n\pi[y-h]}{w})}{\cosh(\frac{n\pi h}{w})}\right]\sin\left(\frac{n\pi x}{w}\right) \tag{A.3}$$

Integrating over the channel cross-section gives the idealized flow rate in the absence of meniscus effects:

$$Q_{ideal} = \frac{4w^3 h}{\pi^3}\frac{\Delta p}{\mu l}\Big[1 - \sum_{n,odd}^{\infty}\frac{1}{n^5}\frac{96}{\pi^4}\frac{w}{\pi h}\tanh\left(\frac{n\pi h}{w}\right)\Big] \tag{A.4}$$

This can be reasonably approximated for $\frac{h}{w} > \frac{1}{2}$ as:

$$Q_{ideal} = \frac{4w^3h}{\pi^3}\frac{\Delta p}{\mu l}\Big[1 - \frac{31\zeta(5)}{30\zeta(4)}\frac{w}{\pi h}\tanh\Big(\frac{\pi h}{w}\Big)\Big] \tag{A.5}$$

where $\zeta(n)$ is the Riemann zeta function evaluated at n.

In order to account for meniscus effects, we subtract away the flow that would have occurred in the void region of the meniscus:

$$Q = Q_{ideal}\Big(1 - \frac{v_{ratio}A_{void}}{A}\Big) \tag{A.6}$$

v_{ratio} is the ratio of the average velocity in the void region to the average velocity of the entire channel. It must fall between 1 and 2 and accounts for that fact that the fraction of flow lost to the meniscus can be greater than the fraction of cross-section lost.

To completely solve for the case of capillary flow in an open microchannel, we must describe the pressure in terms of the microchannel geometry. An approach was described in section 3.1.3 that neglects gravitational and meniscus effects; we modify it now to include both. Average force per unit length of the liquid front is given as:

$$f = -\frac{dE}{dz} = (\gamma_{SV} - \gamma_{SL})(r - \phi_s) - \gamma(1 - \phi_s)F_A - \rho gzh(1 - \phi_s)F_V \tag{A.7}$$

Average flow cross-section per unit length of the liquid front is

$$A_{avg} = h(1 - \phi_s)\Big(1 - \frac{A_{void}}{A}\Big) = h(1 - \phi_s)F_V \tag{A.8}$$

Average capillary pressure is approximated by dividing the force by the cross-section:

$$\Delta p = \frac{\rho gz}{F_V}\Big[\Big(\frac{\lambda^2}{hz}\Big)\Big(\frac{r - \phi_s}{1 - \phi_s}\cos\theta_{CA} - F_A\Big) - F_V\Big] \tag{A.9}$$

F_A multiplies the projection of open liquid surface area to give the actual meniscus surface area. F_V multiples the ideal pore volume to given the actual pore volume, which does not include the void area of the meniscus. These factors can be approximated by assuming that the meniscus takes the shape of a section of cylinder surface area and that it contacts the upper channel edges at the contact angle θ_{CA}. This yields the following expressions:

$$F_A = \frac{\frac{\pi}{2} - \theta_{CA}}{\sin(\frac{\pi}{2} - \theta_{CA})} \tag{A.10}$$

$$F_V = (1 - \frac{w}{4h}[F_A - \sin\theta_{CA}]) \tag{A.11}$$

$$F_{V2} = (1 - v_{ratio}\frac{w}{4h}[F_A - \sin\theta_{CA}]) \tag{A.12}$$

Bibliography

[1] M. C. Roco, "The long view of nanotechnology development: the national nanotechnology initiative at 10 years," in *Nanotechnology Research Directions for Societal Needs in 2020*, pp. 1–28, Springer, 2011.

[2] A. A. Tseng, K. Chen, C. D. Chen, and K. J. Ma, "Electron beam lithography in nanoscale fabrication: recent development," *Electronics Packaging Manufacturing, IEEE Transactions on*, vol. 26, no. 2, pp. 141–149, 2003.

[3] G. Taylor, "Disintegration of water drops in an electric field," *Proceedings of the Royal Society of London. Series A. Mathematical and Physical Sciences*, vol. 280, no. 1382, pp. 383–397, 1964.

[4] D. Garoz, C. Bueno, C. Larriba, S. Castro, I. Romero-Sanz, J. F. de la Mora, Y. Yoshida, and G. Saito, "Taylor cones of ionic liquids from capillary tubes as sources of pure ions: The role of surface tension and electrical conductivity," *Journal of Applied Physics*, vol. 102, no. 6, p. 064913, 2007.

[5] M. Cloupeau and B. Prunet-Foch, "Electrohydrodynamic spraying functioning modes: a critical review," *Journal of Aerosol Science*, vol. 25, no. 6, pp. 1021–1036, 1994.

[6] N. Bhardwaj and S. C. Kundu, "Electrospinning: a fascinating fiber fabrication technique," *Biotechnology advances*, vol. 28, no. 3, pp. 325–347, 2010.

[7] N. M. Thoppey, J. R. Bochinski, L. I. Clarke, and R. E. Gorga, "Unconfined fluid electrospun into high quality nanofibers from a plate edge," *Polymer*, vol. 51, no. 21, pp. 4928–4936, 2010.

[8] T. Nakajima, *Advanced fiber spinning technology*. Elsevier, 1994.

[9] V. Thavasi, G. Singh, and S. Ramakrishna, "Electrospun nanofibers in energy and environmental applications," *Energy & Environmental Science*, vol. 1, no. 2, pp. 205–221, 2008.

[10] T. J. Sill and H. A. von Recum, "Electrospinning: applications in drug delivery and tissue engineering," *Biomaterials*, vol. 29, no. 13, pp. 1989–2006, 2008.

[11] S. Theron, A. Yarin, E. Zussman, and E. Kroll, "Multiple jets in electrospinning: experiment and modeling," *Polymer*, vol. 46, no. 9, pp. 2889–2899, 2005.

[12] A. Yarin and E. Zussman, "Upward needleless electrospinning of multiple nanofibers," *Polymer*, vol. 45, no. 9, pp. 2977–2980, 2004.

[13] D. Lukas, A. Sarkar, and P. Pokorny, "Self-organization of jets in electrospinning from free liquid surface: A generalized approach," *Journal of Applied Physics*, vol. 103, no. 8, p. 084309, 2008.

[14] N. Thoppey, J. Bochinski, L. Clarke, and R. Gorga, "Edge electrospinning for high throughput production of quality nanofibers," *Nanotechnology*, vol. 22, no. 34, p. 345301, 2011.

[15] X. Wang, H. Niu, T. Lin, and X. Wang, "Needleless electrospinning of nanofibers with a conical wire coil," *Polymer Engineering & Science*, vol. 49, no. 8, pp. 1582–1586, 2009.

[16] S. Petrik and M. Maly, "Production nozzle-less electrospinning nanofiber technology," in *MRS Proceedings*, vol. 1240, pp. 1240–WW03, Cambridge Univ Press, 2009.

[17] Y. Srivastava, M. Marquez, and T. Thorsen, "Multijet electrospinning of conducting nanofibers from microfluidic manifolds," *Journal of applied polymer science*, vol. 106, no. 5, pp. 3171–3178, 2007.

[18] C. Chang, K. Limkrailassiri, and L. Lin, "Continuous near-field electrospinning for large area deposition of orderly nanofiber patterns," *Applied Physics Letters*, vol. 93, no. 12, p. 123111, 2008.

[19] L. Rayleigh, "Xx. on the equilibrium of liquid conducting masses charged with electricity," *The London, Edinburgh, and Dublin Philosophical Magazine and Journal of Science*, vol. 14, no. 87, pp. 184–186, 1882.

[20] J. Zeleny, "The electrical discharge from liquid points, and a hydrostatic method of measuring the electric intensity at their surfaces," *Physical Review*, vol. 3, no. 2, p. 69, 1914.

[21] A. L. Yarin, S. Koombhongse, and D. H. Reneker, "Taylor cone and jetting from liquid droplets in electrospinning of nanofibers," *Journal of Applied Physics*, vol. 90, no. 9, pp. 4836–4846, 2001.

[22] J. F. De La Mora and I. G. Loscertales, "The current emitted by highly conducting taylor cones," *Journal of fluid mechanics*, vol. 260, pp. 155–184, 1994.

[23] A. M. Ganan-Calvo, J. Davila, and A. Barrero, "Current and droplet size in the electrospraying of liquids. scaling laws," *Journal of Aerosol Science*, vol. 28, no. 2, pp. 249–275, 1997.

[24] K. Smith, M. Alexander, and J. Stark, "Voltage effects on the volumetric flow rate in cone-jet mode electrospraying," *Journal of applied physics*, vol. 99, no. 6, p. 064909, 2006.

[25] F. A. Hill, E. V. Heubel, P. Ponce de Leon, and L. F. Velasquez-Garcia, "High-throughput ionic liquid ion sources using arrays of microfabricated electrospray emitters with integrated extractor grid and carbon nanotube flow control structures," *Journal of Microelectromechanical Systems*, vol. 23, no. 5, pp. 1237–1248, 2014.

[26] M. M. Hohman, M. Shin, G. Rutledge, and M. P. Brenner, "Electrospinning and electrically forced jets. i. stability theory," *Physics of Fluids (1994-present)*, vol. 13, no. 8, pp. 2201–2220, 2001.

[27] D. H. Reneker, A. L. Yarin, H. Fong, and S. Koombhongse, "Bending instability of electrically charged liquid jets of polymer solutions in electrospinning," *Journal of Applied physics*, vol. 87, no. 9, pp. 4531–4547, 2000.

[28] S. Podenok, M. Sveningsson, K. Hansen, and E. E. Campbell, "Electric field enhancement factors around a metallic, end-capped cylinder," *Nano*, vol. 1, no. 01, pp. 87–93, 2006.

[29] H. Kosmahl, "Analytic evaluation of field emission enhancement factors for ellipsoidal cones and elliptic cross-section wedges," *Electron Devices, IEEE Transactions on*, vol. 38, no. 6, pp. 1534–1537, 1991.

[30] A. Kusne and D. N. Lambeth, "Generalized analytical solution and study of conductive ellipsoidal field emitters," *Electron Devices, IEEE Transactions on*, vol. 57, no. 3, pp. 712–719, 2010.

[31] D. Quéré, "Wetting and roughness," *Annu. Rev. Mater. Res.*, vol. 38, pp. 71–99, 2008.

[32] R. N. Wenzel, "Resistance of solid surfaces to wetting by water," *Industrial & Engineering Chemistry*, vol. 28, no. 8, pp. 988–994, 1936.

[33] A. Cassie and S. Baxter, "Wettability of porous surfaces," *Transactions of the Faraday Society*, vol. 40, pp. 546–551, 1944.

[34] A. Ahuja, J. Taylor, V. Lifton, A. Sidorenko, T. Salamon, E. Lobaton, P. Kolodner, and T. Krupenkin, "Nanonails: A simple geometrical approach to electrically tunable superlyophobic surfaces," *Langmuir*, vol. 24, no. 1, pp. 9–14, 2008.

[35] Z. Zeng and R. Grigg, "A criterion for non-darcy flow in porous media," *Transport in Porous Media*, vol. 63, no. 1, pp. 57–69, 2006.

[36] N. Fries and D. Quéré, *Capillary transport processes in porous materials-experiment and model.* Cuvillier, 2010.

[37] E. W. Washburn, "The dynamics of capillary flow," *Physical review*, vol. 17, no. 3, p. 273, 1921.

[38] D. Quéré, "Inertial capillarity," *EPL (Europhysics Letters)*, vol. 39, no. 5, p. 533, 1997.

[39] C. Bosanquet, "Lv. on the flow of liquids into capillary tubes," *The London, Edinburgh, and Dublin Philosophical Magazine and Journal of Science*, vol. 45, no. 267, pp. 525–531, 1923.

[40] R. Xiao, R. Enright, and E. N. Wang, "Prediction and optimization of liquid propagation in micropillar arrays," *Langmuir*, vol. 26, no. 19, pp. 15070–15075, 2010.

[41] A. Sangani and A. Acrivos, "Slow flow past periodic arrays of cylinders with application to heat transfer," *International journal of Multiphase flow*, vol. 8, no. 3, pp. 193–206, 1982.

[42] P.-G. De Gennes, F. Brochard-Wyart, and D. Quéré, *Capillarity and wetting phenomena: drops, bubbles, pearls, waves.* Springer, 2004.

[43] L. Courbin, J. C. Bird, M. Reyssat, and H. A. Stone, "Dynamics of wetting: from inertial spreading to viscous imbibition," *Journal of Physics: Condensed Matter*, vol. 21, no. 46, p. 464127, 2009.

[44] S. Theron, E. Zussman, and A. Yarin, "Experimental investigation of the governing parameters in the electrospinning of polymer solutions," *Polymer*, vol. 45, no. 6, pp. 2017–2030, 2004.

[45] F. F. Ouali, G. McHale, H. Javed, C. Trabi, N. J. Shirtcliffe, and M. I. Newton, "Wetting considerations in capillary rise and imbibition in closed square tubes and open rectangular cross-section channels," *Microfluidics and nanofluidics*, vol. 15, no. 3, pp. 309–326, 2013.

[46] W. Zheng, L.-P. Wang, D. Or, V. Lazouskaya, and Y. Jin, "Role of mixed boundaries on flow in open capillary channels with curved air–water interfaces," *Langmuir*, vol. 28, no. 35, pp. 12753–12761, 2012.

[47] T.-S. Jiang, O. Soo-Gun, and J. C. Slattery, "Correlation for dynamic contact angle," *Journal of Colloid and Interface Science*, vol. 69, no. 1, pp. 74–77, 1979.

[48] G. Zheng, Y. Dai, L. Wang, and D. Sun, "Direct-write micro/nano-structure for flexible electronic manufacturing," in *Nanotechnology, 2007. IEEE-NANO 2007. 7th IEEE Conference on*, pp. 791–794, IEEE, 2007.

[49] J. Seiwert, C. Clanet, and D. Quéré, "Coating of a textured solid," *Journal of Fluid Mechanics*, vol. 669, pp. 55–63, 2011.

[50] M. Kurečič and M. S. Smole, "Electrospinning: Nanofibre production method.," *Tekstilec*, vol. 56, no. 1, 2013.

[51] Y. Yang, Z. Jia, Q. Li, L. Hou, J. Liu, L. Wang, Z. Guan, and M. Zahn, "A shield ring enhanced equilateral hexagon distributed multi-needle electrospinning spinneret," *Dielectrics and Electrical Insulation, IEEE Transactions on*, vol. 17, no. 5, pp. 1592–1601, 2010.

[52] M. M. Flake, P. K. Nguyen, R. A. Scott, L. R. Vandiver, R. K. Willits, and D. L. Elbert, "Poly (ethylene glycol) microparticles produced by precipitation polymerization in aqueous solution," *Biomacromolecules*, vol. 12, no. 3, pp. 844–850, 2011.

[53] S. Thompson, J. Stukel, A. AlNiemi, and R. K. Willits, "Characteristics of precipitation-formed polyethylene glycol microgels are controlled by molecular weight of reactants," *JoVE (Journal of Visualized Experiments)*, no. 82, pp. e51002–e51002, 2013.